Master thesis

Gravity gradients of prompt elasto-gravity signals

Aspects of their simulation and the possibility to measure them: A case study for the Tohoku-Oki earthquake

Clara Bützler

First Reviewer:	Priv.-Doz. Dr. habil. Thomas Jahr FSU Jena, Institut für Geowissenschaften
Second Reviewer:	Prof. Dr.-Ing. Nico Sneeuw Universität Stuttgart, Geodätisches Institut
First Advisor:	Dr. Karim Douch Universität Stuttgart, Geodätisches Institut
Second Advisor:	Ph.D. Rudolf Widmer-Schnidrig Black Forest Observatory

Processing Time: 15th June 2020 – 3th December 2020

Eigenständigkeitserklärung

Ich erkläre, dass ich die vorliegende Arbeit selbstständig und nur unter Verwendung der angegebenen Hilfsmittel und Quellen angefertigt habe. Die eingereichte Arbeit ist nicht anderweitig als Prüfungsleistung verwendet worden oder als Veröffentlichung erschienen. Seitens der Verfasserin bestehen keine Einwände, die vorliegende Masterarbeit für die öffentliche Benutzung zur Verfügung zu stellen.

Stuttgart, den 03.12.2020, _____

Clara Bützler

Zusammenfassung

Sobald der Bruch eines Erdbebens beginnt, fangen seismische Wellen an, sich auszubreiten. Diese verändern die Dichteverteilung in der Erde, was zu einer Änderung der Gravitation führt. Diese Änderung breitet sich mit Lichtgeschwindigkeit aus und ist somit viel schneller als die seismischen Wellen. Das führt dazu, dass bereits vor dem Einsatz der P-Welle so genannte *prompt elasto-gravity* Signale (PEGS) mit Gravimetern und Seismometern gemessen werden können.
Die Detektion dieser Signale wird allerdings dadurch erschwert, dass Gravimeter und Seismometer nicht nur die genannte Änderung der Schwere messen, sondern auch eine Bodenbeschleunigung, die durch eben diese Schwereänderung verursacht wird. Diese Signale heben sich teilweise gegenseitig auf. Daher wäre es von Vorteil, Messinstrumente zu verwenden, die sensitiv für Schwereänderungen, aber nicht für Bodenbeschleunigungen sind. Diese Eigenschaft erfüllen Gravitationsdehnungsmesser (gravity strainmeter) und Schweregradiometer (gravity gradiometer).
In dieser Arbeit geht es um das Potential von Schweregradiometern für die Detektion von PEGS. Es werden zunächst zwei Methoden zur Modellierung von Schweregradienten von PEGS untersucht und getestet: Die Methode von Harms (2016), welche ein stark vereinfachtes Erdmodell verwendet, kann erfolgreich angewendet werden. Die Umsetzung einer abgewandelten Form der Normalmodensummation, mit der Schweregradienten von PEGS für ein deutlich genaueres Erdmodell berechnet werden können, scheitert hingegen an der Berechnung von Normalmoden für hohe Frequenzen.
Daher wird die Methode von Harms (2016) verwendet, um Schweregradienten von PEGS für das Tohoku-Oki Beben zu simulieren. Die Ergebnisse werden mit den Rauschspektren aktueller Schweregradiometer verglichen. Es zeigt sich, dass die Detektion von PEGS des Tohoku-Oki Bebens auf Grund der unzureichenden Genauigkeit der Instrumente mit aktuellen Schweregradiometern nicht möglich gewesen wäre. Auch mit solchen Schweregradiometern, welche gerade in der Entwicklung sind, stellt sich die Detektion von PEGS als sehr schwierig heraus. Für eine eindeutige Detektion von PEGS müsste die Genauigkeit von Schweregradiometern ungefähr zehnmal höher sein als die derer, welche aktuell entwickelt werden.
Zur Zeit sollten daher für die Untersuchung von PEGS die Messdaten von Seismometern und Gravimetern verwendet werden. In Zukunft können eventuell außerdem Gravitationsdehnungsmesser verwendet werden. Diese werden vor allem für die Detektion von Gravitationswellen entwickelt. Ihr Potential für die Detektion von PEGS wurde bereits in anderen Arbeiten untersucht.

Contents

Chapter 1

Introduction

From the first moment, when the rupture of an earthquake begins, seismic waves start to propagate. The propagation of these waves changes the density distribution of the medium, which leads to a change in gravity, the so-called prompt gravity signal which propagates at the speed of light through the whole Earth.

This gravity perturbation can be observed for example with gravimeters or broadband seismometers before the arrival of the P-wave, but its amplitude is many times smaller than the P-wave signal. Furthermore, the gravity perturbation described above is not the only signal a gravimeter or seismometer measures before the arrival of the P-wave: Additionally, they both measure a ground acceleration induced by the gravity change itself. The resulting signal of both effects is called prompt elasto-gravity signal (PEGS). The gravity change and the ground acceleration partly cancel each other in the measurements of gravimeters or seismometers (Heaton 2017, Vallée et al. 2017, Kame and Kimura 2019), which complicates the detection. However, after having understood this partial cancellation, PEGS have been observed in the measurements for the 2011 Tohoku-Oki earthquake (moment magnitude $M_W = 9.1$) (Vallée et al. 2017) and later for the 1994 deep Bolivia earthquake ($M_W = 8.2$), the 2018 deep Fiji earthquake ($M_W = 8.2$), the 2018 Wharton Basin strike-slip earthquake ($M_W = 8.6$), the 2010 Maule megathrust earthquake ($M_W = 8.8$) and the 2018 Gulf of Alaska strike-slip earthquake ($M_W = 7.9$) (Vallée and Juhel 2019). Meanwhile, methods to model PEGS were developed: Whereas the first one considered the Earth to be a homogeneous full-space (Harms et al. 2015), nowadays PEGS for a self-gravitating, spherical, radial inhomogeneous Earth can be simulated (Juhel et al. 2018b or Zhang et al. 2020).

The detection of PEGS could contribute to earthquake and tsunami early warning systems, especially because they show a strong dependency on the earthquake's magnitude (Vallée et al. 2017). This could lead to earlier realistic estimates of the magnitude, which help to rate the danger of a tsunami. As the measurements of seismometers or gradiometers suffer from the cancellation of ground acceleration and gravity change, Harms et al. (2015), Montagner et al. (2016) and Vallée et al. (2017) proposed to use gravity gradiometers or gravity strainmeters for the detection, which are both not sensitive to

ground motion. The capabilities of gravity strainmeters in this context have been intensively studied by Juhel et al. (2018a) and Shimoda et al. (2020). They found that with gravity strainmeters which are currently under development PEGS of earthquakes down to magnitude $M_W = 7.0$ could be detected.

Supplementing these studies for gravity strainmeters, the aim of this master thesis is to investigate if high sensitivity gravity gradiometers that are already developed or that are under development (Power spectral density between $3\,\mathrm{E}/\sqrt{\mathrm{Hz}}$ and $10^{-4}\,\mathrm{E}/\sqrt{\mathrm{Hz}}$) can represent an alternative solution. An overview of gravity gradiometers that exist or are under development is given in Chapter 5 together with a comparison of the main principles of gravity gradiometers and gravity strainmeters. As a case study I model the gravity gradients of PEGS for the Tohoku-Oki earthquake. To do this simulation, I first have to study how to model gravity gradients of PEGS. Here, I focus on the method of Harms (2016) as a method for a rather simplified Earth model (flat and homogeneous) and the normal mode summation method developed by Juhel et al. (2018b), which is using a more realistic Earth model (radial inhomogeneous sphere) (see Chapter 6). Afterwards, in Chapter 7 I analyse the simulated signals and compare them to the noise spectrum of existing gravity gradiometers and of gravity gradiometers that are under development. Additionally, I compare the signals of gravity gradiometers to the signals of gravity strainmeters.

The main questions, which should be answered in this thesis are:

1. How can existing methods to model gravimeter, seismometer or gravity strainmeter measurements of PEGS be adapted to model gravity gradiometer measurements of PEGS?

2. What do the signals of gravity gradients of PEGS look like?

3. Should it be possible to detect those signals with gravity gradiometers that exist or are under development?

4. Are there advantages or disadvantages of gravity gradiometer signals compared to gravity strainmeter signals with regards to the detection of PEGS?

To give some more background to these investigations I will first present an overview of the Tohoku-Oki earthquake (Chapter 2) and thereafter give a more detailed introduction to the discovery of PEGS and their main physical principles (Chapter 3). This introductory part is concluded by a short recapitulation of the gravity field in spherical harmonics and the basics of continuum mechanics (Chapter 4). In Chapter 8 the results of this master thesis are summarised and further investigations are proposed.

Chapter 2

The Tohoku-Oki earthquake

The investigations of prompt elasto-gravity signals (PEGS) in this thesis are done for the example of the Tohoku-Oki earthquake. The earthquake happened on the 11^{th} of March 2011 off the coast of north eastern Japan (37.52° N, 143.05° E) (Nettles et al. 2011), about 130 km east of the city of Sendai and 370 km north east of Tokio (U.S. Geological Servey 2011). It had a moment magnitude of $M_{\text{W}} = 9.1$, making it the fourth largest earthquake in the last 100 years worldwide and the largest well documented earthquake in Japan (Nettles et al. 2011). The geometry of the moment tensor, strike 203°, dip 10° and slip 88°, indicates that it was triggered by the subduction of the pacific plate beneath the island of Honshu (Nettles et al. 2011). All characteristics of the Tohoku-Oki earthquake reported in the global Centroid Moment Tensor (CMT) catalogue (Nettles et al. 2011) are noted in Table 2.1. A map of Japan showing the fault plane solution of the earthquake can be seen in Figure 2.1. (Nettles et al. 2011). The depth of 0 to 100 km is a typical depth for megathrust earthquakes. They are thrust fault earthquakes happening at subduction zones due to compression and fraction of the two plates (Frisch and Meschede 2005).

Megathrust earthquakes are responsible for most of the tsunamis world-wide and also the Tohoku-Oki earthquake triggered a huge tsunami wave. The tsunami reached the Japanese mainland 20 minutes after the earthquake rupture and affected 2000 km of the Japanese coast. The maximum run-up height was 39.7 m at Miyako, and run-up heights greater than 10 m occurred along 425 km of the coast. The tsunami propagated more than 5 km inland and inundated more than 400 km^2 of land (Mori et al. 2011).

Despite existing early warning systems and tsunami disaster countermeasures, for example tsunami barriers, 15 899 people died through the Tohoku-Oki earthquake and the tsunami. 2 528 people are still missing (National Police Agency of Japan - Emergency Disaster Countermeasures Headquarters 2020). The major cause of death was the tsunami. Furthermore, the tsunami caused the nuclear catastrophe at the nuclear power plant of Fukushima, which was rated with the highest level 7 of the international nuclear and radiological event scale INES (Japanese ministry of economy, trade and industry 2011).

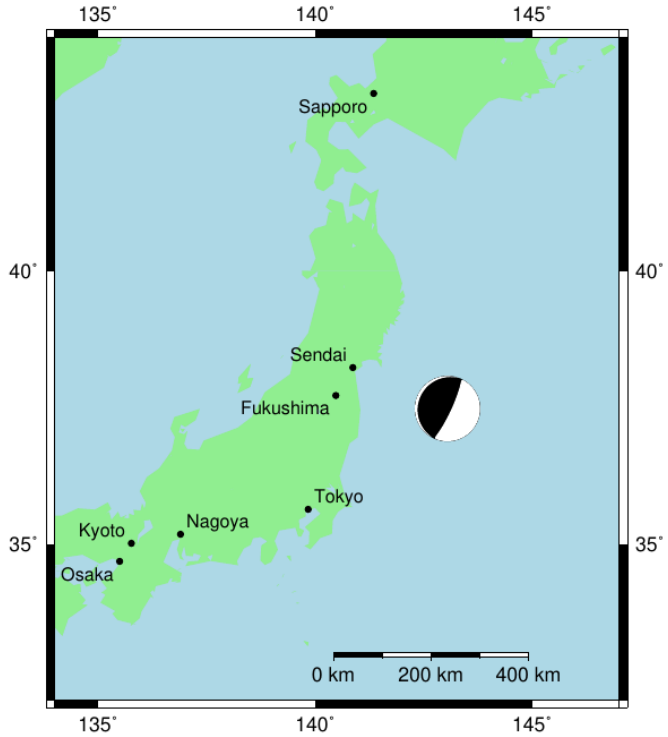

Figure 2.1: **Tohoku-Oki earthquake.** Map of Japan showing the fault plane solution of the Tohoku-Oki earthquake (Nettles et al. 2011)

There is still a clear need for better early warning systems to which measurements of PEGS could possibly contribute, especially because of their high sensitivity to the earthquake's magnitude.

Table 2.1: **Characteristics of the Tohoku-Oki earthquake reported in the global CMT catalogue** (Nettles et al. 2011)

Date:	2011/03/11	Centroid time:	5:47:32.8 GMT	Half width:	70 s
Latitude:	37.52°	Longitude:	143.05°	Depth:	20 km
Moment tensor in 1×10^{29} dyne cm:					
M_{rr}	1.730	$M_{\vartheta\vartheta}$	−0.281	$M_{\varphi\varphi}$	−1.450
$M_{r\vartheta}$	2.120	$M_{r\varphi}$	4.55	$M_{\vartheta\varphi}$	−0.657s
Fault plane:					
Strike:	203°	Dip:	10°	Slip:	88°

Chapter 3

Prompt elasto-gravity signals

In this chapter I first summarise the results of former studies about prompt elasto-gravity signals (PEGS). In the second part I will explain their main physical principles.

3.1 Discovery and recent research results

P-waves were for a long time thought to be the earliest measurable signal of an earthquake. P-wave stands for primary wave and it is the fastest elastic wave.

Mansinha and Hayes (2001) were the first to consider that a gravity signal could be observed in the measurements of superconducting gravimeters before the arrival of the P-wave. However, their search was not successful.

Since Harms et al. (2015) modelled the prompt gravity signal for a homogeneous infinite space, more interest has been devoted to this topic. He later extended his theory to an infinite half space (Harms 2016). Montagner et al. (2016) searched for prompt gravity signals of the 2011 Tohoku-Oki earthquake ($M_W = 9.1$). Using a statistical method, they found a prompt gravity signal with a significance of 98.4 % in the data of the superconducting gravimeter in Kamioka, Japan and a prompt gravity signal with a significance of 99 % in a stacked data set from five broadband seismometers. However, the amplitude of the measured signal was only two third of the one predicted by the model of Harms et al. (2015).

In reply to the observations of Montagner et al. (2016), Heaton (2017) argued that the response of a gravimeter to an instantaneous change in gravity does not only consist of the gravity signal but also of the ground acceleration induced by the elastic response of the Earth to this gravity change. He also showed that these signals should at least partly cancel each other. Vallée et al. (2017) and later Kame and Kimura (2019) showed that for an infinite homogeneous space the ground acceleration would cancel the gravity change completely before the P-wave arrival time. For a more realistic Earth model the cancellation was found to be not as strong but still non-negligible (Vallée et al. 2017).

For this reason, the signal before the arrival of the P-wave, consisting of both the gravity perturbation and the elastic response of the ground, is called prompt elasto-gravity signal (PEGS).

Based on this, Vallée et al. (2017), modelled the PEGS for the Tohoku-Oki earthquake in a layered non-self-gravitating Earth at eleven stations chosen by a signal-to-noise criterion. For the modelling they used a three step procedure. The modelled signals matched very well with the measurements at the eleven stations. The biggest amplitudes were obtained in a distance of 1000 km to 1500 km away from the earthquake, where PEGS measured with seismometers reached an amplitude of 1.6 $\mathrm{nm/s^2}$ before the P-wave arrival time. This favourable distance results from the effect, that for small distances the pre P-wave arrival window is too short and for stations too far away from the earthquake the signal becomes too small due to the distance dependency of the gravity change. Next advances in signal modelling were made by Juhel et al. (2018b) who used a normal mode approach to speed up the computation of the gravity change. However, the ground acceleration can not be directly used from the synthetic seismogram of the normal mode summation due to numerical errors. These errors are induced by the small amplitude of ground acceleration of the PEGS compared to the P-wave. Ground acceleration still had to be calculated in a second step. Additionally to the reduction of computation time, the normal mode approach has the advantage to incorporate the self-gravitation of the Earth, while the approach of Vallée et al. (2017) does not. Nevertheless, the PEGS modelled by Juhel et al. (2018b) differed by about less than 0.3 $\mathrm{nm/s^2}$, that is 14 % from the results of Vallée et al. (2017). This indicates that the effect of self-gravitation of the Earth is negligible. The most recent method to date for modelling PEGS is the one Zhang et al. (2020) describe in their paper. They solve the elastic equation of motion fully coupled to the Poisson equation with the code QSSP (Wang et al. 2017) and overcome the numerical problems resulting from the much smaller displacement contained in the PEGS compared to P-wave by an elegant differential method. Hence, they can model PEGS with only one step of computation. That makes the computations faster. The results have a good agreement to the ones of Vallée et al. (2017) and Juhel et al. (2018b) and the small differences can be essentially explained by different structure and source models.

By modelling PEGS of different focal mechanisms and depths, Vallée and Juhel (2019) found that shallow strike slip earthquakes and large deep earthquakes causes PEGS of bigger amplitudes than megathrust earthquakes of the same magnitude. Based on these findings, they searched for PEGS of other earthquakes than the Tohoku-Oki earthquake. They found PEGS for five more earthquakes (see Chapter 1).

Already in the first articles of Harms et al. (2015) and Montagner et al. (2016) the pos-

sibility to use PEGS for early warning systems was mentioned. In the simple test of modelling the signal not only for the $M_W = 9.1$ Tohoku-Oki earthquake but also for the Tohoku-Oki earthquake scaled down to magnitude $M_W = 8.5$ Vallée et al. (2017) found a strong dependency of PEGS on the earthquake's magnitude. The signal of the $M_W = 8.5$ earthquake had a maximum amplitude of $0.5\,\mathrm{nm/s^2}$ before the arrival of the P-wave, compared to $1.6\,\mathrm{nm/s^2}$ for the $M_W = 9.1$ earthquake. This opens the possibility to obtain accurate magnitude estimates for big earthquakes faster than with current techniques. From their analysis of PEGS of other earthquakes, Vallée and Juhel (2019) conclude that if today's instruments can detect a PEGS, it can be directly assumed that an earthquake of $M_W \geq 8$ happened. Furthermore, if the detected PEGS has a positive sign, the possibility of a subduction megathrust event can be excluded as they produce negative signals everywhere.

Juhel et al. (2018a) investigated the capabilities of gravity strainmeters, which are under development for gravitational wave detection, for earthquake early warning systems. As the sensitivity needed for earthquake early warning systems is lower than for gravitational wave detection, already early stage prototypes of the gravity strainmeters could be used for this purpose. The advantages of both, gravity strainmeters as well as gravity gradiometers, compared to gravimeters were already discussed by other authors before (Harms et al. 2015, Montagner et al. 2016, Vallée et al. 2017): The background seismic noise and the gravity induced ground acceleration would be the same for the two inertial sensors of a gradiometer and therefore, would mostly cancel out in the differential mode. As a result the gravity signal alone is measured. This would not be possible with a gravimeter or seismometer. Juhel et al. (2018a) found that if gravity strainmeter sensitivities of $10^{-15}/\sqrt{\mathrm{Hz}}$ can be achieved, PEGS of earthquakes larger than $M_W = 7.0$ could be detected before the P-wave arrival up to 1000 km away from the earthquake and in the first 10 s up to 120 km away from the earthquake. For the Tohoku-Oki event, they tested a real-time algorithm for estimating the earthquake parameters, based on a matched-filter technique. They found that 5 s before the arrival of the P-wave the PEGS would have been detected with good estimates of the location, the onset time and so far released moment. Furthermore, realistic estimates for the magnitudes could be achieved much earlier than with today's early warning systems, which is important for tsunami early warning. Thus, the gravity strainmeters currently under development show a great potential for the detection of PEGS and their usage for early warning systems.

In this thesis the capabilities of gravity strainmeters are compared to those of gravity gradiometers, which are the second type of instruments sensitive to gravity but not to ground motion.

3.2 Main physical principles

In the following I will present the two main principles of PEGS. Firstly, why there is a prompt-gravity signal measurable before the arrival of P-waves. Secondly, why this prompt gravity signal is not the only signal and why there also exist ground accelerations before the arrival of the P-wave which partly cancels the gravity signal in measurements of seismometers or gravimeters. The sum of these two signals is called prompt-elasto gravity signal (PEGS).

3.2.1 Prompt gravity signals

A sketch of the process responsible for prompt-gravity signals is shown in Figure 3.1. There is a station measuring gravity away from the earthquakes epicentre. Before the earthquake with hypocentre $\boldsymbol{r}_0$ starts, undisturbed gravity is measured. After the rupture onset seismic waves start to propagate. The fastest is the P-wave, which propagates with velocity v_P. The propagation of seismic waves causes dilatation and compression inside the Earth which leads to a change in density. Furthermore, the seismic waves lead to displacement of materials carrying different density. This additionally changes the density distribution. An example is the deformation of layer boundaries. The layer boundary with the biggest density contrast, the the Earth's surface, is the most important in this context. So by all these effects after a certain time t_1 in a sphere with $|\boldsymbol{r} - \boldsymbol{r}_0| < v_\mathrm{P} t_1$ the density distribution has changed. This density change leads to a change in gravity, which occurs throughout the whole Earth, but with increasing distance from the earthquake the size of the gravity change gets smaller. As a seismic wave contains both, areas of dilatation and areas of compression, a lot of their contributions to the gravity change cancel each other. However, the change in density at the wave front the closest to the measurement station contributes the most to the gravity change, so the sign of the gravity change is governed by the contribution of the wave front. As time passes the wave front gets closer to the station. That results in an increase of the gravity change. This time dependent change in gravity can be measured at the station until the first P-wave arrives. Since the signal of the P-wave is about 10^6 times larger than the gravity change the latter cannot be observed anymore after the arrival of the P-wave.

One could think that also the redisplacement of masses at the fault plane produces a measurable gravity change at the measurement station. This would lead to a nearly instantaneous step in measured gravity with the time span of the moment rate function of the earthquake, which should be simultaneously observed at all measurement stations.

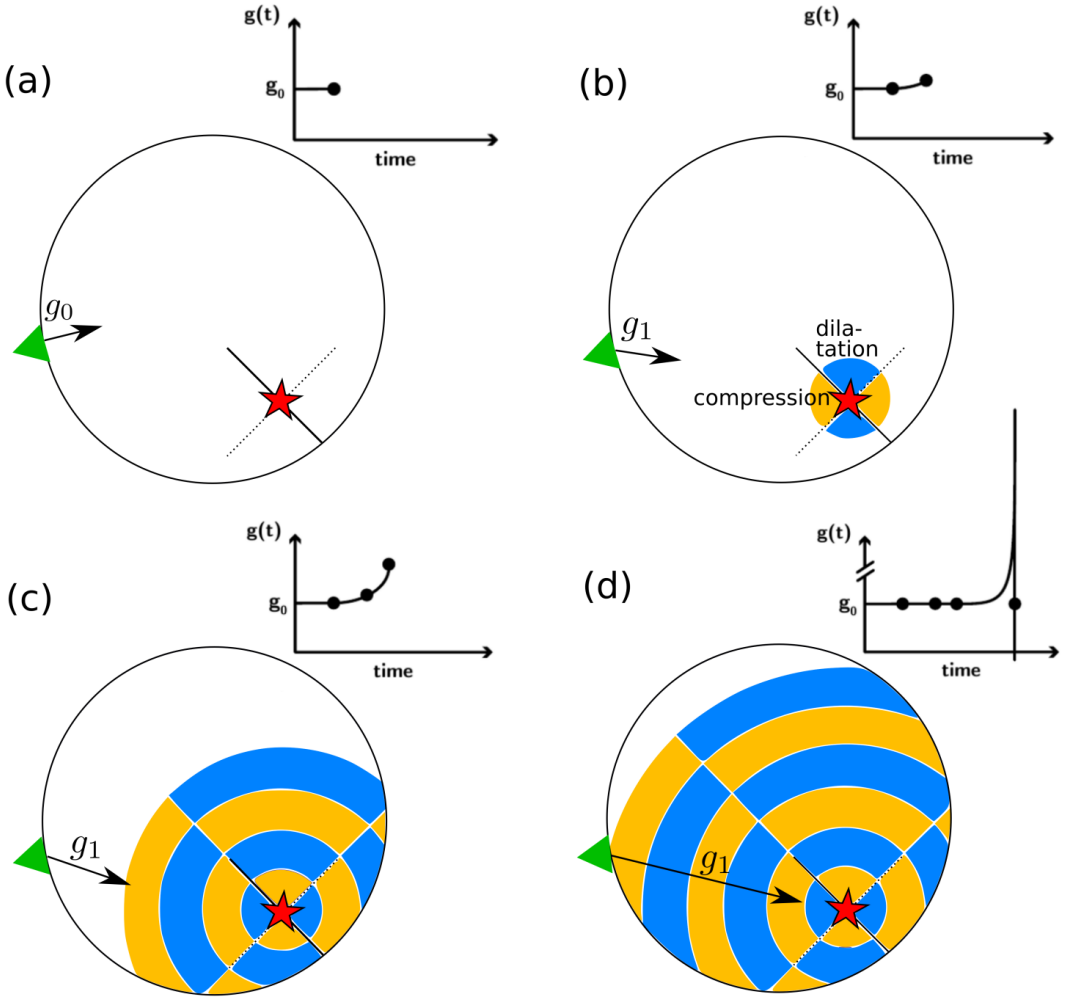

Figure 3.1: **Principle sketch of the origin of prompt gravity signals.** (a) Before the onset of the earthquake the undisturbed gravity g_0 is measured at the station (green triangle). (b) Seismic waves start to propagate. This leads to density increase in the compressed part of the Earth (orange) and density decrease in the dilated part of the Earth (blue). As the compressed part is the closest to the station it has the biggest influence on the gravity change at the station. Gravity at the station increases. (c) The wave front with compressed material gets closer to the station. As a result the gravity change increases. (d) The first P-wave arrives at the station and masks the change in gravity measured at the station. This figure is adapted from Juhel (2017).

However such a signal was not observed (see the observations of Vallée et al. (2017)). Thus, I expect its contribution to be much smaller than the one of the density change related to seismic waves. The reason could be, that the fault plane is further away from the station than the density change related to seismic waves.

3.2.2 Prompt elasto-gravity signals

Heaton (2017) mentioned that the change in gravity is not the only signal a gravimeter or seismometer measures before the arrival of the first P-wave: The change in gravity $\delta \boldsymbol{g}$ of the prompt gravity signal acts as a force on the lithosphere. This force causes an elastic response of the lithosphere, which leads to a ground acceleration $\ddot{\boldsymbol{u}}$ at the gravimeter or seismometer. Both gravimeters and seismometers measure $\delta \boldsymbol{g} - \ddot{\boldsymbol{u}}$ and the two signals partly cancel out each other as they are more or less of the same magnitude. Vallée et al. (2017) and later Kame and Kimura (2019) showed that for an infinite homogeneous space the ground acceleration would cancel the gravity change completely before the P-wave arrival time. For a half space or a layered sphere, this cancellation is not complete and there remains a measurable signal. The mechanism of the additional ground acceleration is sketched in Figure 3.2 to further illustrate the effect . When an earthquake is happening, the propagating waves change the density in a sphere around the hypocentre. This change in density affects gravity at the measurement station, but also everywhere else. At each location inside the Earth this change in gravity acts as a force and excites new elastic waves. If the location is not too far away from the seismometer or gravimeter this wave can reach the station before the P-wave and will be measured as ground acceleration in addition to the gravity change. These two signals partly cancel each other.

Therefore, gravity gradiometers or gravity strainmeters which are not sensitive to ground acceleration but only to a change in gravity could potentially help to measure signals of PEGS. For gravity gradiometers this is studied in this thesis.

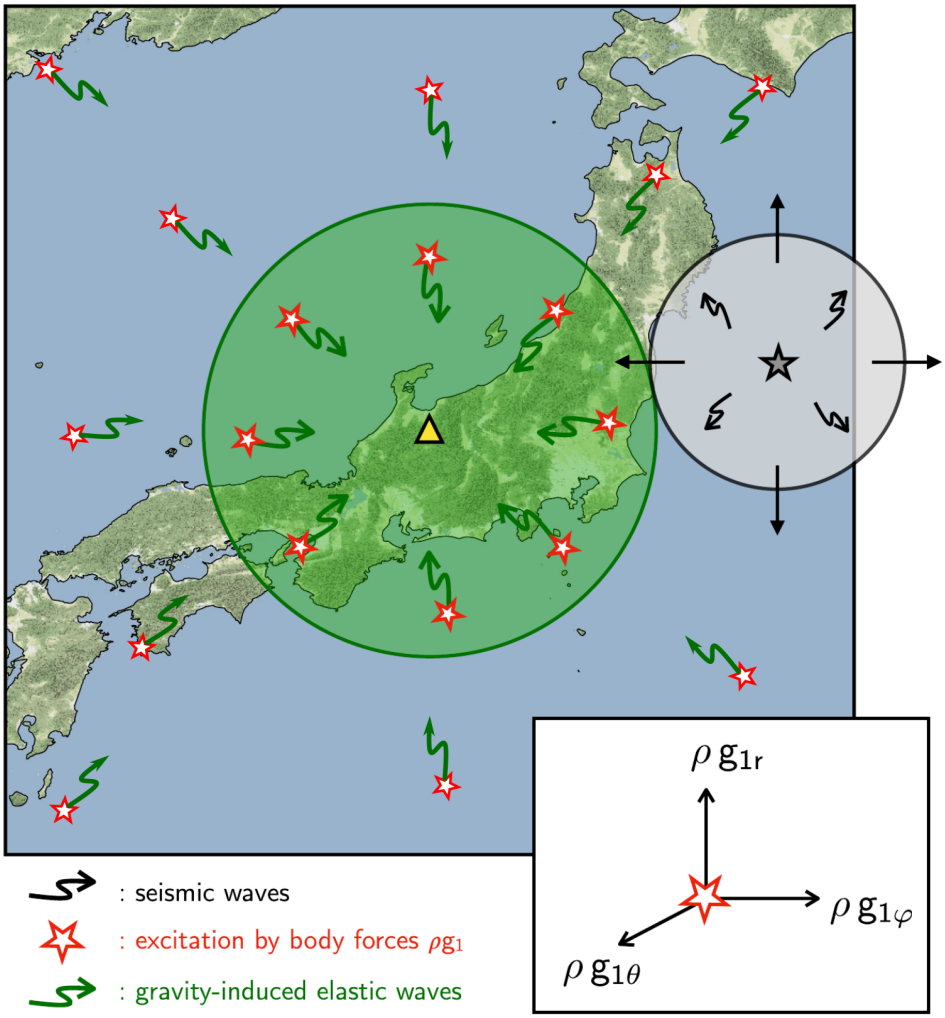

Figure 3.2: **Principle sketch of the origin of the ground acceleration of prompt elasto-gravity signals.** An earthquake with the epicentre at the grey star occurs. Up to now seismic waves (marked in black) have propagated within the grey circle and changed the density within the grey circle. This causes a change in gravity at the station (yellow triangle) and everywhere else. The change in gravity acts as a body force with force density $\boldsymbol{f} = \rho \boldsymbol{g}$ inside the Earth (see small sketch on the lower right). As a result new gravity induced elastic waves are exited everywhere inside the Earth. Those which are exited within the green circle still have enough time to reach the station before the arrival of the P-wave. When they arrive at the station ground acceleration is measured in addition to the gravity change. The figure is adapted from Juhel et al. (2018b).

Chapter 4

Theoretical background to the modelling of PEGS

In this chapter the basics of the gravity field and its expansions in spherical harmonics as well as the basics of continuum mechanics will be introduced. Both will be needed in Chapter 6 to understand the methods for modelling prompt elasto-gravity signals.

4.1 The gravity field and its expansion in spherical harmonics

The gravity potential Φ at position $\boldsymbol{r}$ of a body, for example the Earth, fulfils the Poisson equation (Aki and Richards 1980):

$$\nabla^2\Phi(\boldsymbol{r}) = -4\pi G\rho(\boldsymbol{r})\,, \tag{4.1}$$

where G is the gravitational constant and $\rho(\boldsymbol{r})$ is the density distribution inside the body. The gravity field of the body can than be calculated as

$$\boldsymbol{g}(\boldsymbol{r}) = \nabla\Phi(\boldsymbol{r}) \tag{4.2}$$

and the force density inside the body due to the gravitational field is

$$\boldsymbol{f}(\boldsymbol{r}) = \rho(\boldsymbol{r})\nabla\Phi(\boldsymbol{r})\,.$$

As the shape of the Earth is similar to a sphere it is suitable to use spherical coordinates. In this thesis I use r for the radius, ϑ for the colatitude and φ for the longitude, as sketched in Figure 4.1.

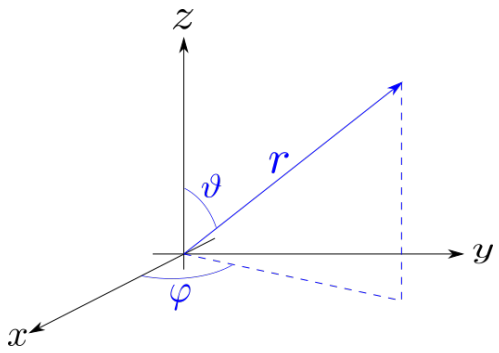

Figure 4.1: **Spherical Coordinates**

In spherical coordinates the ∇-operator, and the ∇^2-operator have the following forms:

$$\begin{aligned}\nabla =& \boldsymbol{e}_r \frac{\partial}{\partial r} + \boldsymbol{e}_\vartheta \frac{1}{r}\frac{\partial}{\partial \vartheta} + \boldsymbol{e}_\varphi \frac{1}{r\sin\vartheta}\frac{\partial}{\partial \varphi}\,,\\ \nabla^2 =& \frac{1}{r^2}\frac{\partial}{\partial r}\left(r^2\frac{\partial}{\partial r}\right) + \frac{1}{r^2\sin\vartheta}\frac{\partial}{\partial\vartheta}\left(\sin\vartheta\frac{\partial}{\partial\vartheta}\right) + \frac{1}{r^2\sin^2\vartheta}\frac{\partial^2}{\partial\varphi^2}\,,\end{aligned}$$

where $\boldsymbol{e}_r$, $\boldsymbol{e}_\vartheta$ and $\boldsymbol{e}_\varphi$ are the unit basis vectors of the coordinate system. If the Poisson equation is written in spherical coordinates it can be shown that its solutions are of the following form (see for example Aki and Richards (1980)):

$$\Phi(r,\vartheta,\varphi) = \sum_{l=0}^{\infty}\sum_{m=-l}^{l} \phi_{lm}(r) Y_{lm}(\vartheta,\varphi)\,, \tag{4.3}$$

where $Y_{lm}(\vartheta,\varphi)$ are the so-called spherical harmonic functions. In this thesis orthonormalised complex spherical harmonics with the Condon-Shortly phase factor are used:

$$Y_{lm}(\vartheta,\varphi) = \bar{P}_l^m(\cos\vartheta)e^{im\varphi}\,, \tag{4.4}$$

where $\bar{P}_l^m$ are the normalised associated Legendre functions, whose definition and some useful relations can be found in Appendix A.

From Equation 4.3 we can derive expressions for the gravity field and the gravity gradient tensor:

The gravity field can be written as

$$\begin{aligned}&\boldsymbol{g}(r,\vartheta,\varphi) = \nabla\Phi(\vartheta,\varphi)\\ &= \sum_{l=0}^{\infty}\sum_{m=-l}^{l}\left(\frac{\partial\phi_{lm}(r)}{\partial r}Y_{lm}(\vartheta,\varphi)\boldsymbol{e}_r + \frac{1}{r}\phi_{lm}(r)\frac{\partial Y_{lm}(\vartheta,\varphi)}{\partial\vartheta}\boldsymbol{e}_\vartheta + \frac{1}{r\sin\vartheta}\phi_{lm}(r)\frac{\partial Y_{lm}(\vartheta,\varphi)}{\partial\varphi}\boldsymbol{e}_\varphi\right).\end{aligned} \tag{4.5}$$

The gravity gradient tensor $\boldsymbol{T}$ is a tensor which consists of the second derivatives of the gravity potential. It describes the gradients of each component of the gravity field. The SI unit for a gravity gradient is $1/\mathrm{s}^2$, but it is often given in units of Eötvös:

$$1\,\mathrm{E} = 1 \times 10^{-9}\,1/\mathrm{s}^2$$

It can be shown that the gravity gradient tensor is symmetric. In spherical coordinates its components are

$$\begin{aligned}
T_{\vartheta j} &= \frac{1}{r}\frac{\partial}{\partial \vartheta}\left(\nabla\Phi(\vartheta,\varphi)\right)\boldsymbol{e}_j\,,\\
T_{\varphi j} &= \frac{1}{r\sin\vartheta}\frac{\partial}{\partial \varphi}\left(\nabla\Phi(\vartheta,\varphi)\right)\boldsymbol{e}_j\,,\\
T_{rj} &= \frac{\partial}{\partial r}\left(\nabla\Phi(\vartheta,\varphi)\right)\boldsymbol{e}_j\,, \qquad j \in \{r,\vartheta,\varphi\}\,.
\end{aligned}$$

For the six independent components we obtain the following equations:

$$\begin{aligned}
T_{\vartheta\vartheta} &= \frac{1}{r^2}\frac{\partial^2\Phi(r,\vartheta,\varphi)}{\partial\vartheta^2} + \frac{1}{r}\frac{\partial\Phi(r,\vartheta,\varphi)}{\partial r}\\
&= \sum_{l=0}^{\infty}\sum_{m=-l}^{l}\left(\frac{1}{r^2}\phi_{lm}(r)\frac{\partial^2 Y_{lm}(\vartheta,\varphi)}{\partial\vartheta^2} + \frac{1}{r}\frac{\partial\phi_{lm}(r)}{\partial r}Y_{lm}(\vartheta,\varphi)\right) \qquad (4.6)\\
T_{\vartheta\varphi} &= -\frac{1}{r^2\tan\vartheta\sin\vartheta}\frac{\partial\Phi(r,\vartheta,\varphi)}{\partial\varphi} + \frac{1}{r^2\sin\vartheta}\frac{\partial^2\Phi(r,\vartheta,\varphi)}{\partial\vartheta\partial\varphi}\\
&= \sum_{l=0}^{\infty}\sum_{m=-l}^{l}\left(-\frac{1}{r^2\tan\vartheta\sin\vartheta}\phi_{lm}(r)\frac{\partial Y_{lm}(\vartheta,\varphi)}{\partial\varphi} + \frac{1}{r^2\sin\vartheta}\phi_{lm}(r)\frac{\partial^2 Y_{lm}(\vartheta,\varphi)}{\partial\vartheta\partial\varphi}\right) \qquad (4.7)\\
T_{\vartheta r} &= -\frac{1}{r^2}\frac{\partial\Phi}{\partial\vartheta} + \frac{1}{r}\frac{\partial^2\Phi(r,\vartheta,\varphi)}{\partial\vartheta\partial r}\\
&= \sum_{l=0}^{\infty}\sum_{m=-l}^{l}\left(-\frac{1}{r^2}\phi_{lm}(r)\frac{\partial Y_{lm}}{\partial\vartheta} + \frac{1}{r}\frac{\partial\phi_{lm}(r)}{\partial r}\frac{\partial Y_{lm}}{\partial\vartheta}\right) \qquad (4.8)\\
T_{\varphi\varphi} &= \frac{1}{r^2\tan\vartheta}\frac{\partial\Phi(r,\vartheta,\varphi)}{\partial\vartheta} + \frac{1}{r^2\sin^2\vartheta}\frac{\partial^2\Phi(r,\vartheta,\varphi)}{\partial\varphi^2} + \frac{1}{r}\frac{\partial\Phi(r,\vartheta,\varphi)}{\partial r}\\
&= \sum_{l=0}^{\infty}\sum_{m=-l}^{l}\Big(\frac{1}{r^2\tan\vartheta}\phi_{lm}(r)\frac{\partial Y_{lm}(\vartheta,\varphi)}{\partial\vartheta}\\
&\qquad + \frac{1}{r^2\sin^2\vartheta}\phi_{lm}(r)\frac{\partial^2 Y_{lm}(\vartheta,\varphi)}{\partial\varphi^2} + \frac{1}{r}\frac{\partial\phi_{lm}(r)}{\partial r}Y_{lm}(\vartheta,\varphi)\Big) \qquad (4.9)
\end{aligned}$$

$$T_{\varphi r} = -\frac{1}{r^2 \sin\vartheta}\frac{\partial\Phi(r,\vartheta,\varphi)}{\partial\varphi} + \frac{1}{r\sin\varphi}\frac{\partial^2\Phi(r,\vartheta,\varphi)}{\partial\varphi\partial r}$$
$$= \sum_{l=0}^{\infty}\sum_{m=-l}^{l}\left(-\frac{1}{r^2\sin\vartheta}\phi_{lm}(r)\frac{\partial Y_{lm}(\vartheta,\varphi)}{\partial\varphi} + \frac{1}{r\sin\vartheta}\phi_{lm}(r)\frac{\partial^2 Y_{lm}(\vartheta,\varphi)}{\partial\varphi\partial r}\right) \tag{4.10}$$

$$T_{rr} = \frac{\partial^2\Phi(r,\vartheta,\varphi)}{\partial r^2} = \sum_{l=0}^{\infty}\sum_{m=-l}^{l}\left(\frac{\partial^2\phi_{lm}(r)}{\partial r^2}Y_{lm}(\vartheta,\varphi)\right) \tag{4.11}$$

Similar equations can for example be found in Petrovskaya and Vershkov (2006), but they differ a bit, as they are for real spherical harmonics and only for the outer gravity field of the Earth, where the dependency on r is known to be $\phi_{lm}(r) = C_{lm}\frac{GM}{r_0}\left(\frac{r_0}{r}\right)^{l+1}$. Hereby is M the mass of the Earth, r_0 the Earth radius and C_{lm} is a coefficient. Furthermore, they use a slightly different coordinate system.

In Equation 4.5 and 4.6 to 4.11 derivatives of spherical harmonics are needed:

$$\begin{aligned}
\frac{\partial Y_{lm}(\vartheta,\varphi)}{\partial\varphi} &= imY_{lm}(\vartheta,\varphi)\,,\\
\frac{\partial^2 Y_{lm}(\vartheta,\varphi)}{\partial\varphi^2} &= -m^2 Y_{lm}(\vartheta,\varphi),\\
\frac{\partial Y_{lm}(\vartheta,\varphi)}{\partial\vartheta} &= \frac{\partial\bar{P}_l^m}{\partial\vartheta}\exp(im\varphi)\,,\\
\frac{\partial^2 Y_{lm}(\vartheta,\varphi)}{\partial\vartheta^2} &= \frac{\partial^2\bar{P}_l^m}{\partial\vartheta^2}\exp(im\varphi)\,,\\
\frac{\partial^2 Y_{lm}(\vartheta,\varphi)}{\partial\varphi\partial\vartheta} &= im\frac{\partial Y_{lm}(\vartheta,\varphi)}{\partial\vartheta}\,,
\end{aligned}$$

where $\frac{\partial\bar{P}_l^m}{\partial\vartheta} = \frac{\partial\bar{P}_l^m(\cos\vartheta)}{\partial\vartheta}$ and $\frac{\partial^2\bar{P}_l^m}{\partial\vartheta^2} = \frac{\partial^2\bar{P}_l^m(\cos\vartheta)}{\partial\vartheta^2}$ are derivatives of the normalised associated Legendre functions. Recursion formulas for them can be found in Appendix A.

4.2 Basics of continuum mechanics

Inside the Earth, kinematics is governed by the Lagrangian equation of motion of continuum mechanics:

$$\rho(\boldsymbol{r})\frac{\partial^2\boldsymbol{u}(\boldsymbol{r},t)}{\partial t^2} = \boldsymbol{f}(\boldsymbol{r},t) + \nabla\cdot\boldsymbol{\tau}(\boldsymbol{r},t)\,, \tag{4.12}$$

where $\boldsymbol{u}(\boldsymbol{r},t)$ is a vector describing the displacement inside the body at point $\boldsymbol{r}$ and time t, $\boldsymbol{f}(\boldsymbol{r},t)$ is the force density acting on the body and $\boldsymbol{\tau}(\boldsymbol{r},t)$ is the stress inside the body. There exists always a dependence between stress and displacement inside the body, which

is different for different material properties. Therefore, this dependence is called material equation. For elastic bodies the material equation is given by Hooke's law, which is a linear relation between the stress tensor $\boldsymbol{\tau}(\boldsymbol{r})$ and the strain tensor $\boldsymbol{\epsilon}(\boldsymbol{r})$. The strain tensor describes the deformation of a body and is composed of spatial derivatives of the displacement $\boldsymbol{u}(\boldsymbol{r})$:

$$\boldsymbol{\epsilon} = \frac{1}{2} \sum_{\alpha,\beta=1}^{3} \left(\frac{\partial u_\beta}{\partial r_\alpha} + \frac{\partial u_\alpha}{\partial r_\beta} \right) \boldsymbol{e}_\alpha \otimes \boldsymbol{e}_\beta \,, \tag{4.13}$$

where $\boldsymbol{e}_\alpha \otimes \boldsymbol{e}_\beta$ is a tensorial product between the unit basis vectors of the coordinate system. For a homogeneous isotropic body, Hooke's law only contains two elastic parameters of the material, the Lamé parameters λ and μ:

$$\boldsymbol{\tau} = \lambda(\nabla \cdot \boldsymbol{u}) \cdot I + 2\mu\boldsymbol{\epsilon} \,, \tag{4.14}$$

where I is the identity matrix. For a given force distribution $\boldsymbol{f}(\boldsymbol{r})$, the equation of motion and Hooke's law determine the displacement field.

Displacement inside a body produces density change. The density change $\delta\rho(\boldsymbol{r}, t)$ is given by the continuity equation of mass:

$$\delta\rho(\boldsymbol{r}, t) = -\nabla \cdot \big(\rho_0(\boldsymbol{r})\boldsymbol{u}(\boldsymbol{r}, t)\big) = -\rho_0(\boldsymbol{r})\nabla \cdot \boldsymbol{u}(\boldsymbol{r}, t) - (\nabla\rho_0(\boldsymbol{r})) \cdot \boldsymbol{u}(\boldsymbol{r}, t) \tag{4.15}$$

Hereby $\rho_0(\boldsymbol{r})$ is the density distribution before the displacement. The density change can be split up into two terms. The first is describing density change due to compression or dilatation of the material and will be called bulk perturbation in the following:

$$\delta\rho_{\text{bulk}}(\boldsymbol{r}, t) = -\rho_0(\boldsymbol{r})\nabla \cdot (\boldsymbol{u}(\boldsymbol{r}, t)) \tag{4.16}$$

It causes the change $\delta\Phi_{\text{bulk}}$ in the gravity potential:

$$\delta\Phi_{\text{bulk}}(\boldsymbol{r}_0, t) = G \int_V \frac{\delta\rho_{\text{bulk}}(\boldsymbol{r}, t)}{|\boldsymbol{r} - \boldsymbol{r}_0|} \mathrm{d}V = -G \int_V \frac{\rho_0(\boldsymbol{r})\nabla \cdot (\boldsymbol{u}(\boldsymbol{r}, t))}{|\boldsymbol{r} - \boldsymbol{r}_0|} \mathrm{d}V \tag{4.17}$$

The second term of Equation 4.15 describes density change due to the displacement of materials carrying different densities, it will be called displacement perturbation in the following:

$$\delta\rho_{\text{disp}}(\boldsymbol{r}, t) = -\boldsymbol{u}(\boldsymbol{r}, t) \cdot \nabla(\rho_0(\boldsymbol{r})) \tag{4.18}$$

Examples for those perturbations are the displacement of the free surface or the deformation of layer boundaries inside the Earth. The related change in gravity potential is

$$\delta\Phi_{\mathrm{disp}}(\boldsymbol{r}_0,t) = G\int\limits_V \frac{\delta\rho_{\mathrm{disp}}(\boldsymbol{r},t)}{|\boldsymbol{r}-\boldsymbol{r}_0|}\mathrm{d}V = -G\int\limits_V \frac{\boldsymbol{u}(\boldsymbol{r},t)\cdot\nabla(\rho_0(\boldsymbol{r}))}{|\boldsymbol{r}-\boldsymbol{r}_0|}\mathrm{d}V\,. \tag{4.19}$$

More details of these basics of continuum mechanics can be found for example in Aki and Richards (1980).

Chapter 5

Gravity gradiometers

The aim of this chapter is to get an overview on existing gradiometers and their noise spectra. In Chapter 7 the noise spectra will be compared to simulated gravity gradients of prompt elasto-gravity signals (PEGS) in order to analyse if these instruments are suitable to detect PEGS. Before, the principles of gravity strainmeters are compared with the principles of gravity gradiometers. This will help to identify advantages of one or the other type of instrument in Chapter 7.

5.1 Principles of gravity strainmeters and gravity gradiometers

As discussed in Chapter 3, one of the main challenges when measuring PEGS is the partial cancellation of the gravity change by the ground acceleration induced by this very same gravity change. This problem could be solved by using gravity strainmeters or gravity gradiometers, which are both insensitive to ground acceleration.

Earlier studies have shown a high potential of gravity strainmeters for the detection of PEGS (Juhel et al. 2018a, Shimoda et al. 2020). These instruments are under development

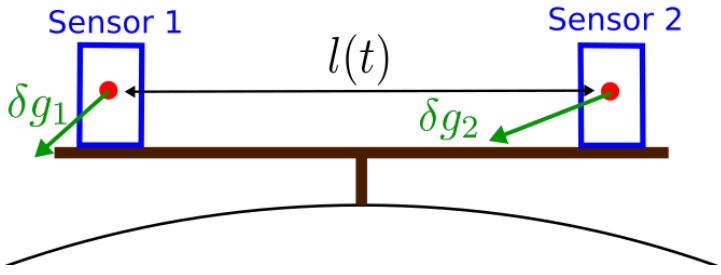

Figure 5.1: **Sketch of a gravity strainmeter.** A gravity strainmeter consists of two sensors. In each of the sensors a test mass (red circle) is levitated against the static gravity field. Different variations of the gravity field at the two test masses result in different movements of each of them. The variation of distance between the two test masses is then measured.

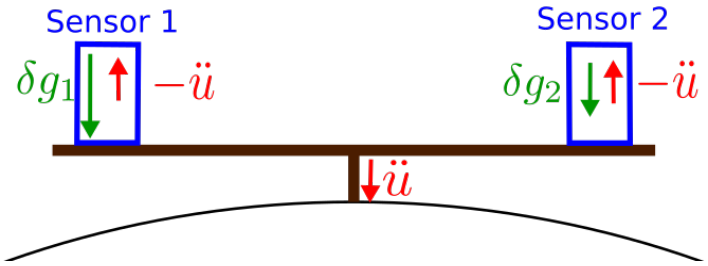

Figure 5.2: **Sketch of a gravity gradiometer.** A gravity gradiometer consists of two sensors. At each of them the total acceleration $\boldsymbol{a} = \boldsymbol{\delta g} - \boldsymbol{\ddot{u}}$ is measured. The difference of these two accelerations is taken.

mainly for the purpose of gravitational wave detection. A simplified sketch of a gravity strainmeter can be seen in Figure 5.1. The instrument consists of two test masses levitated against the static gravity field. The variation of distance between them $\Delta l(t)$ is measured and divided by the original distance $l(0)$. For example for the xx-component of the gravity strain s_{xx}:

$$s_{xx} = \frac{\Delta l_x(t)}{l_x(0)}$$

This is a very good approximation of the true gravity strain, which is the double time integral of the gravity gradient $\boldsymbol{T}$ (Juhel et al. 2018a):

$$\boldsymbol{s} = \int_{t_0}^{t} \int_{t_0}^{t'} \boldsymbol{T}(t'')\mathrm{d}t''\mathrm{d}t' \tag{5.1}$$

If the gravity field changes, the test masses move. If the change in gravity is different at the two ends, the movement of the test masses is also different, which results in a change of distance between them. Consequently, the instrument is sensitive to changes in the gravity gradient. On the other hand, ground acceleration only results in an acceleration of the frame around the test masses but not of the test masses themselves. Therefore, in this case the distance between the test masses remains identical. As a result the instrument is not sensitive to ground acceleration.

The other type of instruments which are sensitive to changes in the gravity gradient, but not to ground acceleration are gravity gradiometers. The main principle of all gravity gradiometers is to measure the difference between the accelerations at two points in the instrument. A simplified sketch of a gravity gradiometer can be seen in Figure 5.2. The gravity gradient relates to the difference of the accelerations $\boldsymbol{a}$ at the two sensors divided

by the distance l between the sensors, for example for the xx-component

$$T_{xx} = \frac{a_{1x} - a_{2x}}{l_x} \,.$$

The accelerations can be caused by movements of the instrument or by the gravity field, but all common movements of the sensors cancel each other in the difference. As a result the instrument is insensitive to ground accelerations. Some gravity gradiometers measure directly the difference of the accelerations as for example the torsion balance of Eötvös (1896), but most of them are measuring the accelerations at two different points separately. If this is the case the instrument can be used in the common mode or the differential mode. In the common mode the accelerations are summed up, so that the mid point acceleration can be approximated. In the differential mode the difference of the accelerations is calculated to estimate the gradient. In an ideal instrument a common acceleration would be completely cancelled out in the differential mode, but for a real instrument this is not the case. Instead of $\boldsymbol{a}_1 - \boldsymbol{a}_2$ it measures:

$$c_1\boldsymbol{a}_1 - c_2\boldsymbol{a}_2 = \frac{1}{2}(c_1 + c_2)(\boldsymbol{a}_1 - \boldsymbol{a}_2) + \frac{1}{2}(c_1 - c_2)(\boldsymbol{a}_1 + \boldsymbol{a}_2) \,,$$

where c_1 and c_2 both are close to 1.0 , but not exactly 1.0. The quotient between the factor in front of the differential signal $\frac{1}{2}(c_1 + c_2)$ and the factor in front of the common signal $\frac{1}{2}(c_1 - c_2)$ is called Common Mode Rejection Ratio (CMRR)

$$\mathrm{CMRR} = \frac{c_1 + c_2}{c_1 - c_2} \,.$$

A good instrument should have a high CMRR.

5.2 Gravity gradiometers that exist or that are under development

In the following I will give a short overview of gravity gradiometers that exist or are under development and their sensitivities. A detailed overview of the history and the today's development in the field of gravity gradiometers can be found in Veryaskin (2018), which was the main source for this section.

5.2.1 The torsion balance of Roland Eötvös

The first gravity gradiometers were based on the torsion balance developed by Eötvös (1896). The principle of this instrument relies on an arm with one test mass at each end, which hangs at a fine torsion filament. A gradient in the gravity field induces different forces on the two test masses, which results in a torsion of the filament. This torsion can be measured and related to the applied torque and the gravity gradient.

5.2.2 Commercial gradiometers

In the recent decades most gradiometers were developed to be used on aircraft or ships for regional mapping of the gravity field in the context of exploration. For measurements on ships or aircraft the rejection of the accelerations of the vehicle in the measurements is very important. The majority of them are using multiple electrical accelerometers on a platform. Examples are the full tensor gradiometers dFTG and eFTG, produced by Lockheed Martin, which are two of the most accurate commercial gravity gradiometers until now. They have a sensitivity of 2.5 to $4\,\mathrm{E}/\sqrt{\mathrm{Hz}}$. Improvements and changes of these instruments are planned (FTG plus) for which the performance goals are $0.5\,\mathrm{E}/\sqrt{\mathrm{Hz}}$ in a frequency range from 0.1 mHz to 5 Hz.

5.2.3 The GREMLIT gradiometer

Another gradiometer for aircraft applications based on electrical accelerometers is the gravity gradiometer GREMLIT described in Douch et al. (2014). They used accelerometers which were initially developed for the GRACE and GOCE missions. The gradiometer can measure the T_{xx}, T_{yy} and T_{xy} components. The following formula for the square root of the power spectral density (PSD) of the intrinsic noise of the sensor is given for frequencies f:

$$\sqrt{S_T(f)} = 0.08\,\mathrm{E}/\sqrt{\mathrm{Hz}}\sqrt{\left(\frac{f_{c1}}{f}\right)^2 + \left(\frac{f_{c0}}{f}\right)^4 + 1 + \left(\frac{f}{f_{c2}}\right)^4}$$

with $f_{c1} = 3 \times 10^{-3}\,\mathrm{Hz}$, $f_{c0} = 2 \times 10^{-5}\,\mathrm{Hz}$ and $f_{c2} = 0.12\,\mathrm{Hz}$. That results in values below $1\,\mathrm{E}/\sqrt{\mathrm{Hz}}$ in a frequency range of 10^{-3} to $3 \times 10^{-2}\,\mathrm{Hz}$.

5.2.4 Gradiometer developed by Moody et al. (2002)

In the last decades a group of scientists at the University of Maryland developed several gradiometers based on superconducting accelerometers. One of them is described in Moody et al. (2002). The accelerometers consist of test masses suspended with high quality mechanical springs, whose displacement is measured with superconducting coils and SQUIDS. Their prototype instrument could measure all three diagonal elements of the gradient tensor. They presented the following estimated PSD of the intrinsic noise of the instrument. This estimate consists of thermal noise and readout noise:

$$S_T(f) = \frac{8}{ml^2}\left(\frac{k_B T \omega_d}{Q_d} + \frac{\omega_d^2}{2\nu\beta} E_{\mathrm{SQ}}(f)\right) \qquad \text{for } \omega = 2\pi f \ll \omega_d\,. \tag{5.2}$$

Hereby $k_B \approx 1.38 \times 10^{-23}\,\mathrm{J/kg}$ is the Boltzmann constant, m is the mass of the test masses and l is the baseline between them. $T = 4.2\,\mathrm{K}$ is the temperature at which the accelerometers are operating. Q_d is the quality factor of the differential mode, which is increasing with decreasing pressure in the vacuum chamber. ω_D is the resonance frequency of the differential mode. β and η are the electromechanical energy coupling and the energy coupling efficiency from circuit to SQUID and $E_{\mathrm{SQ}}(f)$ is the energy resolution of the SQUID. Values for m, l, ω_d, Q_d, β and η are given in Table 5.1. The energy resolution of the SQUID can reach $E_{\mathrm{SQ}}(f) = (1 + \frac{0.1\,\mathrm{Hz}}{f}) \cdot 5 \times 10^{-31}\,\mathrm{J/Hz}$ in a ideal experimental setup but it was measured to be about 10 times larger in the instrument. $E_{\mathrm{SQ}}(f) = (1 + \frac{0.1\,\mathrm{Hz}}{f}) \cdot 5 \times 10^{-30}\,\mathrm{J/Hz}$ is used in the following. Inserting these values to Equation 5.2 gives values for $\sqrt{S(f)}$ below $10^{-2}\,\mathrm{E}/\sqrt{\mathrm{Hz}}$ at frequencies between 0.1 Hz and 10 Hz. However, the measured noise was about 5 times bigger. With further improvements of the instrument, the theoretic intrinsic noise level (Formula 5.2) seems to be reachable.

5.2.5 Gradiometer developed by Griggs et al. (2017)

The concept of the gradiometer presented in Moody et al. (2002) was further developed by Griggs et al. (2017). The test masses in the accelerometers which where suspended mechanically before are here levitated by magnetic fields in a superconducting environment. A prototype can measure two components of the gradient tensor, one diagonal and one off-diagonal, for example T_{xx} and T_{yz}. It is mainly developed for space applications where the gravity acceleration g is nearly zero, but it could be tested in a laboratory as well, where $g \ncong 0$. Due to misalignment of the sensitive axes of the accelerometers the CMRR was limited and the sensitivity of the instrument could not be demonstrated. They give formulas for the PSD of the intrinsic sensitivity, similar to Moody et al. (2002),

but extended for $\omega_d < \omega$ and non-diagonal elements:

$$\text{For the diagonal element:} \qquad S_T(f) = \frac{8}{ml^2}\left(\frac{k_B T \omega_d}{Q_d} + \frac{(\omega - \omega^2)^2}{2\nu\beta\omega_d^2} E_{\mathrm{SQ}}(f)\right) \tag{5.3}$$

$$\text{For the off-diagonal element:} \qquad S_T(f) = \frac{2}{\zeta^2 J}\left(\frac{k_B T \omega_d}{Q_d} + \frac{(\omega - \omega^2)^2}{2\nu\beta\omega_d^2} E_{\mathrm{SQ}}(f)\right) \tag{5.4}$$

ζ is the gradient to angular acceleration conversion factor and J is the moment of inertia of the rotating arms. Values for m, l, ζ, J, ω_d, Q_d, β and η are given in Table 5.1. Here, it is assumed that the best performance of the SQUID can be reached ($E_{\mathrm{SQ}}(f) = (1 + \frac{0.1\,\mathrm{Hz}}{f}) \cdot 5 \times 10^{-31}\,\mathrm{J/Hz}$). This gives values below $10^{-3}\,\mathrm{E}/\sqrt{\mathrm{Hz}}$ at frequencies below 0.1 Hz. It will be challenging to reach the theoretic intrinsic noise level of the instrument (Formulas 5.3 and 5.4), especially when $g \ncong 0$, but it could be possible. According to the authors (Griggs et al. 2017) it is planned to expand the instrument to a full tensor gradiometer for space ($g \approx 0$). However, they did not clearly state, if the measurement principle works in an environment with $g \ncong 0$ for the components T_{zz} and T_{xy}.

The gradiometers developed at the University of Maryland were also considered in the study of Juhel et al. (2018a) concerning the capabilities of gravity strainmeters for PEGS detection. However, in that article they were considered to be used as gravity strainmeters.

Figure 5.3 shows a comparison of measured or estimated square roots of the PSD of the noise levels of the instruments described above. These will be compared to simulated gravity gradients of PEGS in Chapter 7.

Other ideas to measure gravity gradients came up in the last decades. Examples are quantum gravity gradiometer with free falling cold atoms or two superconducting gravimeters measuring next to each other. However, they could not reach sensitivities below $1\,\mathrm{E}/\sqrt{\mathrm{Hz}}$ yet.

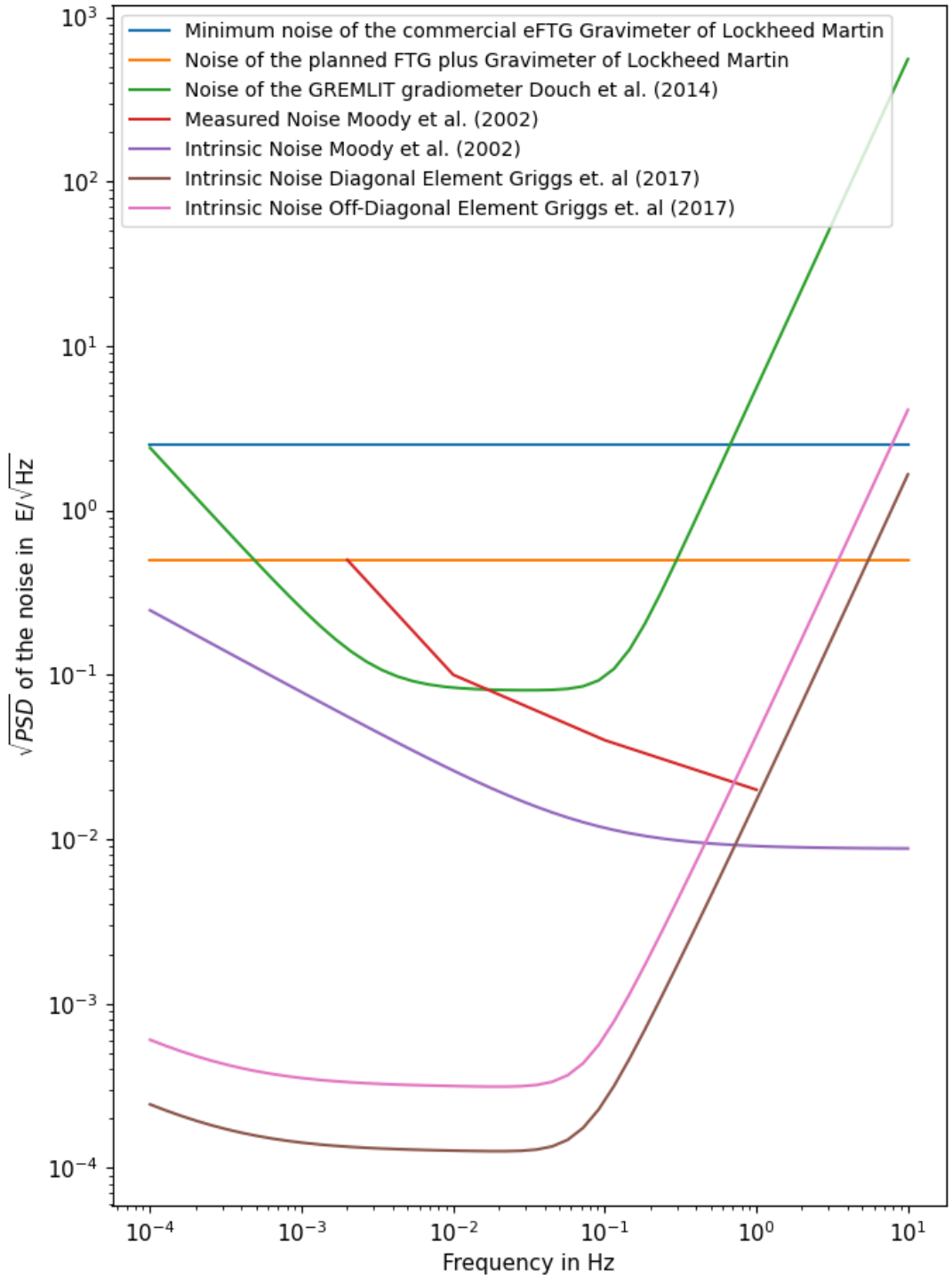

Figure 5.3: **Noise spectra of gradiometers**

Table 5.1: **Design parameters of superconducting gravity gradiometers.** The table shows the design parameters of the superconducting gravity gradiometers developed by Moody et al. (2002) and Griggs et al. (2017).

Parameter	Moody et al. (2002)	Griggs et al. 2017
m(kg)	1.07	0.10
l(m)	0.19	0.135
J(kgm^2)		8.1×10^{-5}
ζ		0.96
$2\pi\omega_d = f_d$(Hz)	10.40	0.02
Q_d	5×10^4	2×10^6
β	0.28	1
ν	0.13	0.4

Chapter 6

Modelling gravity gradients of prompt elasto-gravity signals

In this chapter two existing methods for the modelling of prompt-elasto gravity signals (PEGS) are presented: the method of Harms (2016), which uses a rather simplified Earth model, a flat homogeneous Earth, and the method of Juhel et al. (2018b) which is based on normal mode summation and considers a self-gravitating, spherical, radial inhomogeneous Earth. By small adaptations they can be used to model gravity gradients of PEGS. For both of the methods tests of this modelling are performed in this chapter.

6.1 The method of Harms (2016)

Harms (2016) found a semi-analytic method to calculate prompt gravity signals in a homogeneous half-space. The model covers the change in gravity but not the ground acceleration due elastic response of the Earth. For modelling the outputs of gravity gradiometers, this is sufficient as they are not sensitive to ground acceleration. I will introduce the basic ideas of the method in this chapter. Afterwards I will explain how I use it to calculate gravity gradients of PEGS in a half-space.

6.1.1 Theory

The coordinate system used for the half-space is sketched in Figure 6.1. Cartesian coordinates are used. The z-axis is pointing upwards. I will denote position vectors as $\boldsymbol{r} = (\boldsymbol{\sigma}, z)$, where $\boldsymbol{\sigma}$ is a vector in the x-y plane. Similarly other vectors are split in their x-y-component and their z-component. For example, the displacement vector $\boldsymbol{u}$ can be written as $\boldsymbol{u} = (\boldsymbol{u}_\sigma, u_z)$. The density is constant for $z \leq 0$ and zero for $z > 0$.

The displacement field of the earthquake $\boldsymbol{u}$ causes a change in density given by the continuity equation of mass (see Chapter 4, Equation 4.15). That will cause a change in the gravity potential. Inserting the density distribution of the half-space into Equation 4.17

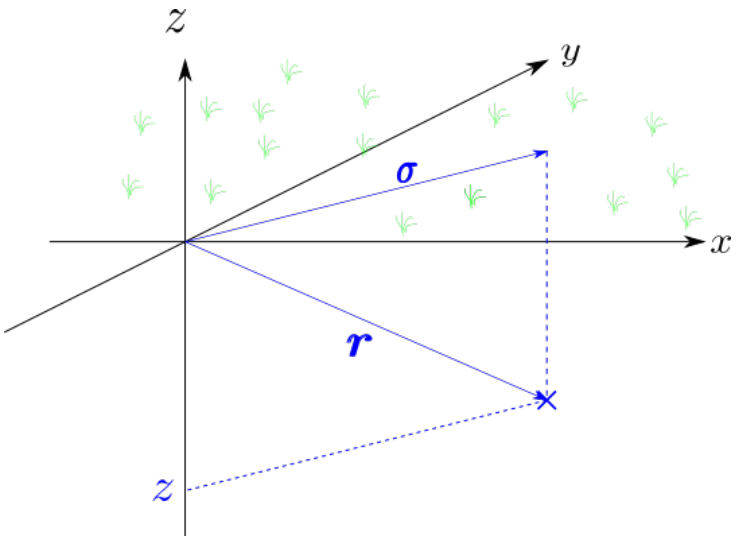

Figure 6.1: **Coordinate system for the half space.** Cartesian coordinates are used to describe points in the half space. The vector $\boldsymbol{\sigma}$ is the projection of the position vector $\boldsymbol{r}$ to the x-y-plane. The Earth surface is at $z = 0$.

gives the first contribution to the change in gravity, which is the bulk perturbation of the gravity potential:

$$\delta\Phi_{\text{bulk}}(\boldsymbol{r}_0, t) = -G\rho_0 \int\limits_{V(z\leq 0)} \frac{\nabla(\boldsymbol{u}(\boldsymbol{r}, t))}{|\boldsymbol{r} - \boldsymbol{r}_0|} \mathrm{d}V \tag{6.1}$$

For the second contribution, the displacement perturbation of the gravity potential, we need the gradient of the density distribution of the half space:

$$\nabla(\rho_0(\boldsymbol{r})) = -\rho_0 \boldsymbol{n}(\boldsymbol{r})\delta(z)\,, \tag{6.2}$$

where $\boldsymbol{n}(\boldsymbol{r})$ is the surface normal and $\delta(z)$ is the delta distribution. The gradient of the density distribution is zero everywhere beside at the Earth's surface ($z = 0$). There it points in the direction of the surface normal which is

$$\boldsymbol{n}(\boldsymbol{r}) = \begin{pmatrix} 0 \\ 0 \\ 1 \end{pmatrix} \tag{6.3}$$

in the used coordinate system.

$$\Rightarrow \boldsymbol{u}(\boldsymbol{r}, t) \cdot \boldsymbol{n}(\boldsymbol{r}) = u_z(\boldsymbol{r}, t) \tag{6.4}$$

Inserting Equations 6.2 and 6.4 into Equation 4.19 gives

$$\delta\Phi_{\text{disp}}(\boldsymbol{r}_0, t) = G\rho_0 \int\limits_S \frac{u_z(\boldsymbol{r}, t)}{|\boldsymbol{r} - \boldsymbol{r}_0|} \mathrm{d}S \tag{6.5}$$

with S as the surface of the half-space.

The calculations are continued in the Fourier domain of $\boldsymbol{\sigma}_0$. The Fourier transforms of Equations 6.1 and 6.5 are

$$\begin{aligned}
\delta\tilde{\Phi}_{\text{bulk}}(\boldsymbol{k}_\sigma, z, t) &= 2\pi G\rho_0 \frac{1}{k_\sigma} \int\limits_{-\infty}^{0} \mathrm{e}^{-k_\sigma|z-z_0|} \left(\partial_z \tilde{u}_z(\boldsymbol{k}_\sigma, z, t) + i\boldsymbol{k}_\sigma \tilde{\boldsymbol{u}}(\boldsymbol{k}_\sigma, z, t)\right) \mathrm{d}z\,, \\
\delta\tilde{\Phi}_{\text{disp}}(\boldsymbol{k}_\sigma, z, t) &= -2\pi G\rho_0 \frac{1}{k_\sigma} \tilde{u}_z(\boldsymbol{k}_\sigma, 0, t) \mathrm{e}^{-k_\sigma|z_0|}\,.
\end{aligned}$$

This can be simplified by partial integration of the first summand of the integrand of $\delta\Phi_{\text{bulk}}(\boldsymbol{k}_\sigma, z, t)$. The total gravity change then becomes

$$\delta\tilde{\Phi}(\boldsymbol{k}_\sigma, z, t) = 2\pi G\rho_0 \int\limits_{-\infty}^{0} \mathrm{e}^{-k_\sigma|z-z_0|} \left(\mathrm{sgn}(z - z_0)\tilde{u}_z(\boldsymbol{k}_\sigma, z, t) + \mathrm{i}\frac{\boldsymbol{k}_\sigma}{k_\sigma}\tilde{\boldsymbol{u}}_\sigma(\boldsymbol{k}_\sigma, z, t)\right) \mathrm{d}z\,. \tag{6.6}$$

The next step is to express the displacement field $\boldsymbol{u}(\boldsymbol{r}, t)$ in terms of potentials. Following the Helmholtz theorem the vector field $\boldsymbol{u}(\boldsymbol{r}, t)$ can be expressed in terms of a gradient of a scalar potential $\phi_s(\boldsymbol{r}, t)$ and the rotation of a vector potential $\boldsymbol{\psi}_s(\boldsymbol{r}, t)$:

$$\boldsymbol{u}(\boldsymbol{r}, t) = \nabla\phi_s(\boldsymbol{r}, t) + \nabla \times \boldsymbol{\psi}_s(\boldsymbol{r}, t)$$

with $\nabla \cdot \boldsymbol{\psi}_s(\boldsymbol{r}, t) = 0$. With this constrain $\boldsymbol{\psi}_s(\boldsymbol{r}, t)$ can itself be expressed by two scalar potentials:

$$\begin{aligned}
\boldsymbol{\psi}_s(\boldsymbol{r}, t) &= \nabla \times \begin{pmatrix} 0 \\ 0 \\ \psi_S(\boldsymbol{r}, t) \end{pmatrix} + \begin{pmatrix} 0 \\ 0 \\ \chi_s(\boldsymbol{\sigma}, t) \end{pmatrix} = \begin{pmatrix} \partial_y\psi_S(\boldsymbol{r}, t) \\ -\partial_x\psi_S(\boldsymbol{r}, t) \\ \chi_s(\boldsymbol{\sigma}, t) \end{pmatrix}\,, \\
\Rightarrow \boldsymbol{u}(\boldsymbol{r}, t) &= \begin{pmatrix} \partial_x\phi_S(\boldsymbol{r}, t)) \\ \partial_y\phi_S(\boldsymbol{r}, t) \\ \partial_z\phi_S(\boldsymbol{r}, t) \end{pmatrix} + \begin{pmatrix} \partial_y\chi_S(\boldsymbol{\sigma}, t) + \partial_z\partial_x\psi_S(\boldsymbol{r}, t) \\ \partial_z\partial_y\psi_S(\boldsymbol{r}, t) - \partial_x\chi_S(\boldsymbol{\sigma}, t) \\ -\partial_x^2\psi_S(\boldsymbol{r}, t) - \partial_y^2\psi_S(\boldsymbol{r}, t) \end{pmatrix}\,,
\end{aligned}$$

or in the Fourier domain of $\boldsymbol{\sigma}$:

$$\tilde{\boldsymbol{u}}(\boldsymbol{k}_\sigma, z, t) = \begin{pmatrix} \mathrm{i}k_x\tilde{\phi}_S(\boldsymbol{k}_\sigma, z, t) \\ \mathrm{i}k_y\tilde{\phi}_S(\boldsymbol{k}_\sigma, z, t) \\ \partial_z\tilde{\phi}_S(\boldsymbol{k}_\sigma, z, t) \end{pmatrix} + \begin{pmatrix} \mathrm{i}k_y\tilde{\chi}_S(\boldsymbol{k}_\sigma, t) + \mathrm{i}k_x\partial_z\tilde{\psi}_S(\boldsymbol{k}_\sigma, z, t) \\ \mathrm{i}k_y\partial_z\tilde{\psi}_S(\boldsymbol{k}_\sigma, z, t) - \mathrm{i}k_x\tilde{\chi}_S(\boldsymbol{k}_\sigma, t) \\ (k_x^2 + k_y^2)\tilde{\psi}_S(\boldsymbol{k}_\sigma, z, t) \end{pmatrix} . \tag{6.7}$$

Inserting Equation 6.7 into Equation 6.6 leads to

$$\delta\tilde{\Phi}(\boldsymbol{k}_\sigma, z, t) = 2\pi G\rho_0 \int_{-\infty}^{0} \mathrm{e}^{-k_\sigma|z-z_0|}\Big(\operatorname{sgn}(z-z_0)\Big(\partial_z\tilde{\phi}_S(\boldsymbol{k}_\sigma, z, t) + k_\sigma^2\tilde{\psi}_S(\boldsymbol{k}_\sigma, z, t)\Big) - k_\sigma\big[\tilde{\phi}_S(\boldsymbol{k}_\sigma, z, t) + \partial_z\tilde{\psi}_S(\boldsymbol{k}_\sigma, z, t)\big]\Big)\mathrm{d}z\,.$$

By smart partial integration, one can obtain

$$\delta\tilde{\Phi}(\boldsymbol{k}_\sigma, z_0, t) = -2\pi G\rho_0\Big(\mathrm{e}^{-k_\sigma|z_0|}\Big(\operatorname{sgn}(z_0)\tilde{\phi}_S(\boldsymbol{k}_\sigma, 0, t) + k_\sigma\tilde{\psi}_s(\boldsymbol{k}_\sigma, 0, t)\Big) + 2\tilde{\phi}_s(\boldsymbol{k}_\sigma, z_0, t)\Big)\,. \tag{6.8}$$

So, to calculate the gravity change in the Fourier domain of $\boldsymbol{\sigma}$ at the observation height z_0 we only need the seismic potentials $\tilde{\phi}_S(\boldsymbol{k}_\sigma, z, t)$ and $\tilde{\psi}_S(\boldsymbol{k}_\sigma, z, t)$ at the surface $z = 0$ and the observation height $z = z_0$. Most of the time measurements are taken above the Earth surface $z_0 > 0$ where the seismic potentials are equal to zero. In this case Equation 6.8 simplifies to

$$\delta\tilde{\Phi}(\boldsymbol{k}_\sigma, z_0, t) = -2\pi G\rho_0\mathrm{e}^{-k_\sigma z_0}\Big(\tilde{\phi}_S(\boldsymbol{k}_\sigma, 0, t) + k_\sigma\tilde{\psi}_s(\boldsymbol{k}_\sigma, 0, t)\Big)\,.$$

For a measurement at the surface we have

$$\delta\tilde{\Phi}(\boldsymbol{k}_\sigma, 0, t) = -2\pi vG\rho_0\Big(\tilde{\phi}_S(\boldsymbol{k}_\sigma, 0, t) + k_\sigma\tilde{\psi}_s(\boldsymbol{k}_\sigma, 0, t)\Big)\,. \tag{6.9}$$

Equation 6.9 can be easily transformed to the Laplace domain of time ($t \to s$):

$$\delta\hat{\Phi}(\boldsymbol{k}_\sigma, z_0, s) = -2\pi G\rho_0\Big(\hat{\phi}_S(\boldsymbol{k}_\sigma, 0, s) + k_\sigma\hat{\psi}_s(\boldsymbol{k}_\sigma, 0, s)\Big) \tag{6.10}$$

To calculate the gravity change caused by an earthquake with moment tensor $\boldsymbol{M}$, first the seismic potentials $\phi_S(\boldsymbol{k}_\sigma, 0, s)$ and $\psi_s(\boldsymbol{k}_\sigma, 0, s)$ at the Earth's surface have to be found. This can be achieved by solving the equation of motion and Hooke's Law (see chapter 4, Equations 4.12 and 4.14) in the Fourier domain of space ($(x, y, z) \to (k_x, k_y, k_z)$) and the Laplace domain of time ($t \to s$). The force term related to a sudden release of the moment

tensor of the earthquake is

$$\boldsymbol{f}(\boldsymbol{r}) = -\boldsymbol{M} \cdot \nabla\delta(\boldsymbol{r} - \boldsymbol{r}_s)H(t)\,, \tag{6.11}$$

where $\boldsymbol{r}_s$ is the hypocentre of the earthquake and $H(t)$ is the step function with $H(t) = 0$ for $t < 0$ and $H(t) = 1$ for $t \geq 0$.

Attention: I use the opposite sign convention for the moment tensor than Harms (2016) here to be coherent with section 6.2.1. This is the sign convention of Aki and Richards (1980).

After having solved the equation of motion and Hooke's Law, the inverse Fourier transforms of $\hat{\phi}_S(\boldsymbol{k}, s)$ and $\hat{\psi}_s(\boldsymbol{k}, 0, s)$ can be calculated with respect to k_z and then be inserted into Equation 6.10. This gives an analytic expression for the gravity change induced by the earthquake in the Fourier domain of x and y and the Laplace domain of time:

$$\delta\hat{\Phi}(\boldsymbol{k}_\sigma, 0, s) = \delta\hat{\Phi}_\infty(\boldsymbol{k}_\sigma, 0, s) + \delta\hat{\Phi}_\alpha(\boldsymbol{k}_\sigma, 0, s) + \delta\hat{\Phi}_\beta(\boldsymbol{k}_\sigma, 0, s) \tag{6.12}$$

with

$$\delta\hat{\Phi}_\infty(\boldsymbol{k}_\sigma, 0, s) = -2\pi G \mathrm{e}^{k_\sigma z_s} \frac{1}{k_\sigma s^2}(k_x, k_y, ik_\sigma) \cdot \boldsymbol{M} \cdot \begin{pmatrix} k_x \\ k_y \\ ik_\sigma \end{pmatrix}\,,$$

$$\delta\hat{\Phi}_\alpha(\boldsymbol{k}_\sigma, 0, s) = 4\pi G \mathrm{e}^{\nu_\alpha z_s} \frac{1}{s^2} \frac{k_\sigma(k_\sigma - \nu_\beta)^2}{(\nu_\beta^2 + k_\sigma^2)^2 - 4\nu_\alpha\nu_\beta k_\sigma^2}(k_x, k_y, i\nu_\alpha) \cdot \boldsymbol{M} \cdot \begin{pmatrix} k_x \\ k_y \\ i\nu_\alpha \end{pmatrix}\,,$$

$$\delta\hat{\Phi}_\beta(\boldsymbol{k}_\sigma, 0, s) = 4\pi G \mathrm{e}^{\nu_\beta z_s} \frac{1}{s^2} \frac{k_\sigma^2 - 2k_\sigma\nu_\alpha + \nu_\beta^2}{(\nu_\beta^2 + k_\sigma^2)^2 - 4\nu_\alpha\nu_\beta k_\sigma^2}(k_x\nu_\beta, k_y\nu_\beta, ik_\sigma^2) \cdot \boldsymbol{M} \cdot \begin{pmatrix} k_x \\ k_y \\ i\nu_\beta \end{pmatrix}$$

and

$$\nu_\alpha = \sqrt{\frac{s^2}{\alpha^2} + k_\sigma^2}\,,$$
$$\nu_\beta = \sqrt{\frac{s^2}{\beta^2} + k_\sigma^2}\,,$$

where α and β are the P- and S-wave velocities.
As we are normally interested in the gravity change in spatial and time domain, inverse Fourier transforms from k_x and k_y to x and y and an inverse Laplace Transform from s

to t have to be calculated. In the method of Harms (2016) this is done by the so called Cangniard-de Hoop method. The basic idea of this method is to write the inverse Fourier transform of $\delta\Phi(\boldsymbol{k}_\sigma, 0, s)$:

$$\delta\bar{\Phi}(x, z, 0, s) = \frac{1}{(2\pi)^2} \int_{-\infty}^{\infty} \int_{-\infty}^{\infty} \mathrm{e}^{\mathrm{i}\boldsymbol{k}_\sigma \boldsymbol{\sigma}} \delta\hat{\Phi}(\boldsymbol{k}_\sigma, 0, s) \mathrm{d}k_y \mathrm{d}k_x$$

and manipulate the integrals by substitutions to get an expression of the form

$$\delta\bar{\Phi}(x, z, 0, s) = \int_0^{\infty} A(t) \mathrm{e}^{-st} \mathrm{d}t \,. \tag{6.13}$$

As this is the same form as the definition of the Laplace transform (see Appendix B), $A(t)$ is the searched solution for $\delta\Phi(x, y, 0, t)$. In general $A(t)$ will be an integral itself, which has to be solved numerically. However, compared to direct numerical inverse Fourier and Laplace transform of Equation 6.12 only one integral instead of three has to be calculated numerically. The substitutions needed to get the form of Equation 6.13 will lead to integrals in the complex plane, which causes several difficulties related to complex analysis. A detailed description of the Cangniard-de Hoop method can be found in Aki and Richards (1980). The substitutions needed for the inverse transformations of 6.12 are described in Harms (2016).

The result of the Cangniard-de Hoop method $\delta\Phi(x, y, 0, t)$ gives the change of the gravity potential for a step-like evolution of the body-force equivalent of the earthquake, see Equation 6.11. For a realistic earthquake, the time evolution of the force is more complicated than a simple step function. It can be expressed as a convolution of the normalised source-time function $\dot{m}(t)$ with the step-like evolution of the body force:

$$\boldsymbol{f}(t) = -\int_{\tau=-\infty}^{+\infty} \dot{m}(t) \boldsymbol{M} \cdot \nabla\delta(\boldsymbol{r} - \boldsymbol{r}_s) H(t - \tau) \mathrm{d}\tau$$

The source-time-function describes how much moment is released per unit of time. It is often modelled as a triangle. The change in gravity potential for this time evolution is given by the convolution with the change in gravity potential for a step-like evolution:

$$\delta\Phi_{\text{realistic}}(x, y, 0, t) = \delta\Phi(x, y, 0, t) * \dot{m}(t)$$

6.1.2 Simulations

To simulate gravity gradients of PEGS with the method of Harms (2016) I use a python code written by Juhel, which is available on GitHub (Juhel 2018). This code is mainly a translation of a Matlab code written by Harms, where he implemented the method described in the previous section. The python code was originally written to compute the xz- and the yz-component of the gravity strain of PEGS. The computation gravity strain is carried out by taking the difference of the z-component of the gravity vector at two points with a distance of 10 m, dividing the result by 10 m and performing two numerical integrations in time. By leaving out these integrations, the code can be used to calculate gravity gradients. I slightly extended the code to compute also the xx-, the xy-, and the yy-component of the gravity gradient tensor. I keep the distance of 10 m between the two points where gravity is computed, although in contrast to gravity strainmeters, most gravity gradiometers are smaller than 10 m. This linear approximation should remain below other errors, for example the one of the simplified Earth model, because the spatial wavelength of the gravity signal is much longer. To compute the zz-component of the gravity gradient I make use of the property that the gradient tensor is trace free above the Earth's surface, where measurements are usually carried out:

$$T_{\mathrm{zz}} = -T_{\mathrm{xx}} - T_{\mathrm{yy}}$$

The results of these simulations for the Tohoku-Oki earthquake will be shown and discussed in Chapter 7. For the computations in Chapter 7 I use the same P- and S-wave velocities as Juhel et al. (2018a): $v_P = 6400\,\mathrm{m/s}$ and $v_S = 3200\,\mathrm{m/s}$.

6.1.3 Limitations of the method

Although the method of Harms (2016) is very useful for an estimation of the size of the gravity gradient signals, it has some limitations if accurate time series of gravity gradients should be calculated.

The first limitation of the method is related to the actual inhomogeneity of the Earth: As the method solves the problem for a homogeneous half space, we have to choose one P- and one S-wave velocity which should be valid for the whole Earth. However, in reality the velocities change especially with depth. Therefore, the optimal choice of the velocities is not clear. That is why Harms (2016), Juhel et al. (2018a) and Juhel et al. (2018b) used each a different combination of P- and S-wave velocities, when applying the method of Harms (2016). The values can be found in Table 6.1. To test the sensitivity of simulated

gravity gradients on the chosen P- and S-wave velocities for one station I calculated the gravity gradients with the three different values for P- and S-wave velocities. This test was done for the Tohoku-Oki earthquake and a station 150 km away from the epicentre in the west direction perpendicular to the strike. The results can be seen in Figure 6.2. The higher P-wave velocity of Juhel et al. (2018a) shortens the signals about around 5 s compared to the signals simulated with the P-wave velocity of Harms (2016) and Juhel et al. (2018b), which are around 25 s long. This shortening also results in a decrease of the maximum amplitude of each component of the gravity gradient by about two third of the signal. For most of the components (EE, NN, EN, ZZ) beside this shortening the signals are nearly not influenced by the different velocities. As a result, the signals simulated with the velocities of Harms (2016) and those simulated with the velocities of Juhel et al. (2018b) are nearly the same, as they use the same P-wave velocity and therefore have the same length. However, for example for the EZ-component the forms of the signal differ clearly between the three different velocity models. Here, the signal simulated with the velocity model of Juhel et al. (2018b) is about three times bigger at the end of the time series than the one simulated with the velocities of Harms (2016). In conclusion, on the one hand, significant differences between the results of the different velocity models can be seen, which would become important for example if measured data should be analysed. On the other hand the magnitude of the signals is similar for all the velocity models, hence for estimating the order of magnitude of gravity gradients the differences between the different velocity models are not important.

A second limitations of the method of Harms (2016) is the negligence of the full coupling between gravity change and ground motion. This means, that Harms (2016) considers that the displacement field of the earthquake changes the gravity field, but he does not consider that the change of the gravity field itself changes the displacement field, which then changes the gravity field again and so on. This would lead to a complete coupling between the equation of motion and the Poisson equation. However, at least for the gravity field Juhel et al. (2018b) found, that the influence of this coupling is smaller than 14 % and I expect it to be at the same order of magnitude for the gravity gradient. Whereas for the simulation of outputs of gravity gradiometers the coupling of the equation of motion and the Poisson equation may be neglected, it is indeed not negligible anymore, when simulating the output of gravimeters or seismometers, as then it is this coupling which leads to the additional ground acceleration.

Another limitation of the method pf Harms (2016) is the negligence of the sphericity of the Earth. However, all stations studied in this thesis are not more than 1000 km away from the earthquake. Therefore, I expect the influence of the negligence of the Earth's

Table 6.1: **P- and S-wave velocities used by different authors, when applying the method of Harms (2016).**

	P-wave velocity	S-wave velocity
Harms (2016)	$6.4\,\frac{\mathrm{km}}{\mathrm{s}}$	$3.2\,\frac{\mathrm{km}}{\mathrm{s}}$
Juhel et al. (2018a)	$7.8\,\frac{\mathrm{km}}{\mathrm{s}}$	$4.4\,\frac{\mathrm{km}}{\mathrm{s}}$
Juhel et al. (2018b)	$6.4\,\frac{\mathrm{km}}{\mathrm{s}}$	$3.7\,\frac{\mathrm{km}}{\mathrm{s}}$

sphericity to be much smaller than the influence of the assumption that the Earth's material is homogeneous.

6.2 The method of Juhel et al. (2018b)

One possibility to overcome the limitations of the method of Harms (2016) that were stated above is to use the method of normal mode summation. It facilitates the simulation of PEGS for a spherical, radial inhomogeneous, self gravitating Earth.

Juhel et al. (2018b) were the first one, who used the method of normal mode summation to calculate PEGS. Originally normal mode summation was developed to calculate low period synthetic seismograms for teleseismic earthquakes. But with very little modification it can be used to calculate prompt-gravity signals of earthquakes. As Juhel et al. (2018b) simulated seismometer outputs, they also had to simulate the pre P-wave ground acceleration. Due to numerical difficulties, this is not possible with a direct normal mode summation. However, for the simulation of gravity gradiometer outputs ground acceleration is not relevant. Hence for this purpose all results can be calculated by a direct normal mode summation.

6.2.1 Normal mode theory

This section gives an introduction to the theory of normal modes. First, I discuss the equations of motion for a spherical, non-rotating, self-gravitating symmetric Earth. Based on this, normal modes are introduced. Afterwards, I derive how the whole wave field of an earthquake can be described as a sum of normal modes. In the end, it is shown how these formulas can easily be changed to calculate the change in gravity or the change in the gravity gradient instead of the displacement. Except for the last part, a more detailed introduction can be found for example in Aki and Richards (1980).

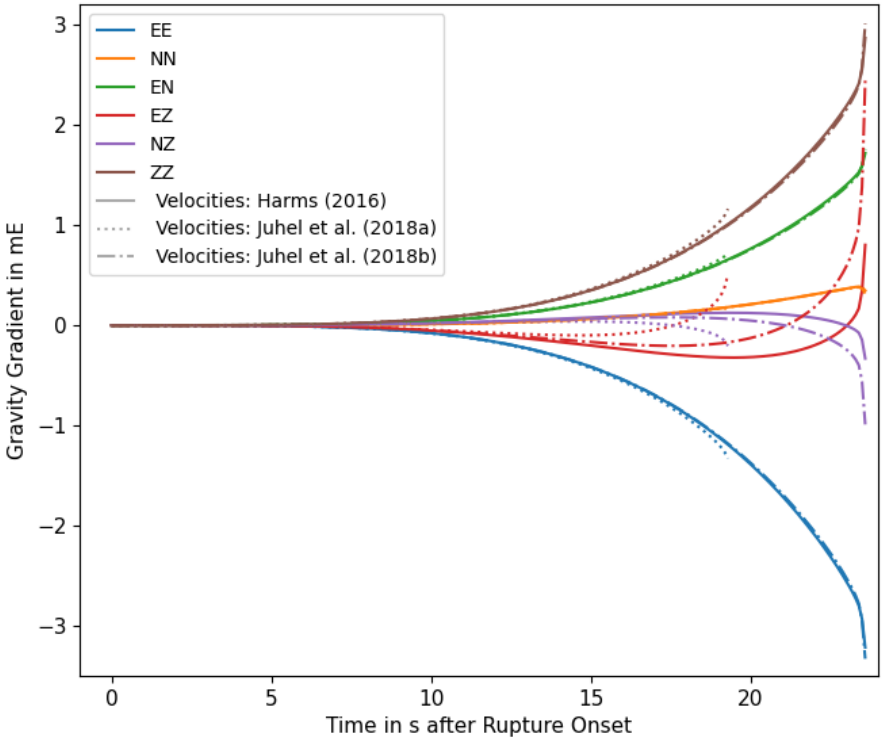

Figure 6.2: **Sensitivity of the method of Harms (2016) to different choices for P- and S-wave velocities.** The figure shows the time evolution of all six components of the gravity gradient simulated with the method of Harms (2016). The computations were done with three different velocity models used by other authors when applying the method of Harms (2016). The results are shown for the Tohoku-Oki earthquake and a station 150 km away from the earthquake in the west direction perpendicular to the strike.

The equations of motion for a spherical, non-rotating, self-gravitating, symmetric Earth

The governing equations for elastic processes inside the Earth, for example seismic wave propagation caused by an earthquake, are the equation of motion of continuum mechanics and Hooke's law (see Chapter 4, Equations 4.12 and 4.14).

If Hooke's law is inserted into the equation of motion and the strain $\boldsymbol{\epsilon}$ is written in terms of the displacement $\boldsymbol{u}(\boldsymbol{r})$, one differential equation in space and time for the displacement $\boldsymbol{u}$ can be obtained. This differential equation depends on the density distribution, the distribution of the Lamé parameters and the force density.

The main part of the force term is the body force $\boldsymbol{f}_{\mathrm{EQ}}(\boldsymbol{r}, t)$ connected to the moment tensor $\boldsymbol{M}(\boldsymbol{r}_s)$ of the earthquake at the hypocentre $\boldsymbol{r}_s$ (see Equation 6.11). However, especially for low frequencies, the change in gravity due to the deformation of the Earth is also a significant part of the force term. Then, the force term becomes

$$\boldsymbol{f}(\boldsymbol{r}, t) = \boldsymbol{f}_{\mathrm{EQ}}(\boldsymbol{r}, t) + \nabla \delta\Phi(\boldsymbol{r}, t)\,.$$

The change of the gravity potential during the earthquake $\delta\Phi(\boldsymbol{x}, t)$ and the change in the density distribution $\delta\rho(\boldsymbol{x}, t)$ satisfy the Poisson equation (Equation 4.1):

$$\nabla^2 \delta\Phi(\boldsymbol{r}, t) = -4\pi G \delta\rho(\boldsymbol{r}, t)$$

Furthermore, the continuity equation of mass gives a relation between the density change and the displacement, see Chapter 4, Equation 4.15. As the change in gravity enters into the force density of the equation of motion by $\nabla\delta\Phi(\boldsymbol{r}, t)$, this leads to a coupling of the equation of motion and the Poisson equation. They need then to be simultaneously solved for the displacement $\boldsymbol{u}(\boldsymbol{r}, t)$ and the change in gravity potential $\delta\Phi(\boldsymbol{r}, t)$. For seismic waves the displacement is small and the solution can be assumed to be a small perturbation away from the equilibrium configuration.

If these equations should be solved for a spherical symmetric Earth where the Lamé parameters $\lambda(\boldsymbol{x})$ and $\mu(\boldsymbol{x})$ only depend on the radius r it turns out to be useful to express the spatial variation of the change in gravity potential $\delta\Phi(\vartheta, \varphi)$ and the displacement $\boldsymbol{u}(r, \vartheta, \varphi)$

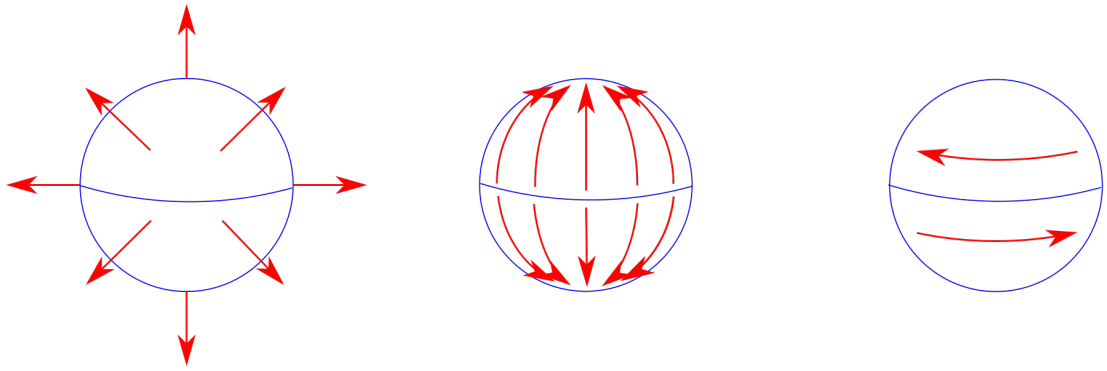

(a) $Y_{00}(\vartheta,\varphi)\boldsymbol{e}_r$ (b) $\nabla_1 Y_{20}(\vartheta,\varphi)$ (c) $e_r \times (\nabla_1 Y_{20}(\vartheta,\varphi))$

Figure 6.3: **Vector Spherical Harmonics.** The figure shows examples for the three summands of a vector spherical harmonic expansion: The radial part (Subfigure 6.3a), rotation free part of the tangential displacement (Subfigure 6.3b) and the incompressible part of the tangential displacement (Subfigure 6.3c).

in terms of spherical harmonics and so-called vector spherical harmonics:

$$\delta\Phi(r,\vartheta,\varphi,t) = \sum_{l=0}^{\infty}\sum_{m=-l}^{m=l} \tilde{\phi}_{lm}(r,t)Y_{lm}(\vartheta,\varphi) \tag{6.14}$$

$$\boldsymbol{u}(r,\vartheta,\varphi,t) = \sum_{l=0}^{\infty}\sum_{m=-l}^{m=l} \tilde{U}_{lm}(r,t)Y_{lm}(\vartheta,\varphi)\boldsymbol{e}_r + \tilde{V}_{lm}(r,t)\nabla_1 Y_{lm}(\vartheta,\varphi) + \tilde{W}_{lm}(r,t)\boldsymbol{e}_r \times (\nabla_1 Y_{lm}(\vartheta,\varphi)) \tag{6.15}$$

with ∇_1 being the tangential part of the gradient:

$$\nabla_1 = \boldsymbol{e}_\vartheta \frac{\partial}{\partial\vartheta} + \boldsymbol{e}_\varphi \frac{1}{\sin\vartheta}\frac{\partial}{\partial\varphi}$$

In the vector spherical harmonic expansion of $\boldsymbol{u}(r,\vartheta,\varphi,t)$, $\tilde{U}_{lm}(r,t)$ describes the radial part of the displacement, $\tilde{V}_{lm}(r,t)$ describes the rotation free part of the tangential displacement ($\nabla \times \left[\tilde{V}_{lm}(r,t)\nabla_1 Y_{lm}(\vartheta,\varphi)\right] = 0$) and $\tilde{W}_{lm}(r,t)$ describes the divergence-free or incompressible part of the tangential displacement ($\nabla \left(\tilde{W}_{lm}(r,t)\boldsymbol{e}_r \times [\nabla_1 Y_{lm}(\vartheta,\varphi)]\right) = 0$). Possible examples of these three parts of the displacement are shown in Figure 6.3. As the displacement described by $\tilde{W}_{lm}(r,t)$ is divergence-free and for a radial symmetric Earth $\rho_0(\boldsymbol{x})$ only varies in radial direction, Equation 4.15 shows that the displacement described by $\tilde{W}_{lm}(r,t)$, the so-called toroidal displacement, does not cause density change and consequently no gravity change. Furthermore, it can be shown that the equation for $\tilde{W}_{lm}(r,t)$ completely decouples from the others. Therefore $\tilde{W}_{lm}(r,t)$ and the toroidal displacement will not be further considered here.

If the spherical harmonic expansions of the gravity potential and the displacement are inserted into the equation of motion, Hooke's law and the Poisson equation, three coupled differential equations for $\tilde{U}_{lm}(r,t)$, $\tilde{V}_{lm}(r,t)$ and $\tilde{\phi}_{lm}(r,t)$ can be obtained. In theory, also the force term would have to be expressed in vector spherical harmonics, but I will now first discuss the solutions for the homogeneous equation, that is for $\boldsymbol{f}(\boldsymbol{r}) = 0$.

If the force term is set to zero, the ansatz

$$\begin{aligned}\tilde{U}_{lm}(r,t) &= U_{lm}(r)\mathrm{e}^{i\omega t}\,,\\ \tilde{V}_{lm}(r,t) &= V_{lm}(r)\mathrm{e}^{i\omega t}\,,\\ \tilde{\phi}_{lm}(r,t) &= \phi_{lm}(r)\mathrm{e}^{i\omega t}\end{aligned}$$

can be made. Then three differential equations of second order for $U_{lm}(r)$, $V_{lm}(r)$ and $\phi_{lm}(r)$ are obtained, which contain only $\lambda(r)$, $\mu(r)$, ρ_0, $g_0(r)$, l and ω. The differential equations and their complete derivation is given for example by Takeuchi and Saito (1992). It can be found, that there only exist solutions for discrete values of ${}_n\omega_l$. They are called eigenfrequencies of the Earth corresponding to the eigenmodes (n,l,m). The corresponding solutions ${}_nU_l(r)$, ${}_nV_l(r)$ and ${}_n\phi_l(r)$ are called eigenfunctions. As the equations for $U_{lm}(r)$, $V_{lm}(r)$ and $\phi_{lm}(r)$ do not depend on m, eigenmodes with different m but same n and l, have the same eigenfrequencies and the same radial dependency, but they have different dependencies in ϑ and φ, which are described by the spherical harmonic functions. On the contrary, eigenmodes with different n but same l and m have the same dependency on ϑ and φ but different frequency and different radial dependence. The modes with $n > 0$ are called overtones with respect to the mode with $n = 0$.

The just discussed eigenmodes, for which the corresponding displacement is described by $U_{lm}(r)$ and $V_{lm}(r)$ are called spheroidal modes in contrast to the toroidal modes. For $l = 0$, $V_{lm}(r) = 0$, so the eigenmodes with $l = 0$ only contain radial movement. Normally they are treated separately, as the differential equations simplify for them. They are then called radial modes. A sketch of the spatial patterns of some of the modes can be found in Figure 6.4.

These solutions to the homogeneous problem without a force term describe free oscillations of the whole Earth, which can for example be excited by earthquakes. Figure 6.5 shows the frequency spectrum of a seismogram observed after the great Sumatra 2004 earthquake together with the theoretical spectrum for a spherical, non-rotating Earth, based on normal mode theory. A match between the peaks at frequencies of normal modes, can clearly be seen. This match further improves for more realistic Earth models. It is also possible to describe the whole wave field caused by an earthquake as a large sum

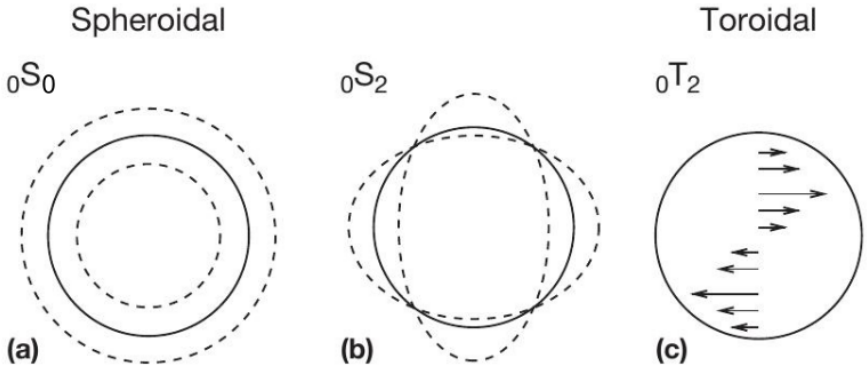

Figure 6.4: **Spatial Patterns of the first normal modes.** The sketch shows the spatial pattern of (a) the ${}_0S_0$-mode also called the "breathing"-mode, (b) the ${}_0S_2$-mode also called the "football" mode and (c) the ${}_0T_2$-mode. All the modes are shown for $m = 0$. The figure is taken from Woodhouse and Deuss (2015).

of eigenmodes. I will later introduce how the solution for the inhomogeneous problem with an excitation force, for example the equivalent body force of the earthquake, can be build up from eigenfrequencies and eigenfunctions. But I will first discuss the simplified problem of N particles oscillating around an equilibrium.

Summation of normal modes

This formulation of the summation of normal modes follows the work of Gilbert (1970).

Let us consider a system of N particles, which can move in three dimensions. The α-th particle has mass m_α. Its displacement from equilibrium is described by the three dimensional vector $\boldsymbol{u}_\alpha$ ($\alpha \in \{1..N\}$). The internal elastic force $\boldsymbol{f}_\alpha^{\text{elastic}}$ on the α-th particle depends linearly on the displacements $\boldsymbol{u}_\beta$ of all other β particles. The linear relation is described by the N^2 3×3 matrices $\boldsymbol{V}_{\alpha\beta}$, which are called the potential energy matrices:

$$\boldsymbol{f}_\alpha^{\text{elastic}}(t) = -\sum_{\beta=1}^{N} \boldsymbol{V}_{\alpha\beta} \cdot \boldsymbol{u}_\beta(t)$$

Additionally, different external forces $\boldsymbol{f}_\alpha(t)$ can act on each particle. This gives the following equation of motion:

$$m_\alpha \frac{d^2\boldsymbol{u}_\alpha(t)}{dt^2} + \sum_{\beta=1}^{N} \boldsymbol{V}_{\alpha\beta} \cdot \boldsymbol{u}_\beta(t) = \boldsymbol{f}_\alpha(t) \tag{6.16}$$

This system has eigenfunctions of the form ${}_n\boldsymbol{s}_\alpha e^{i\omega_n t}$ which solve 6.16 for $\boldsymbol{f}_\alpha(t) = 0$. For

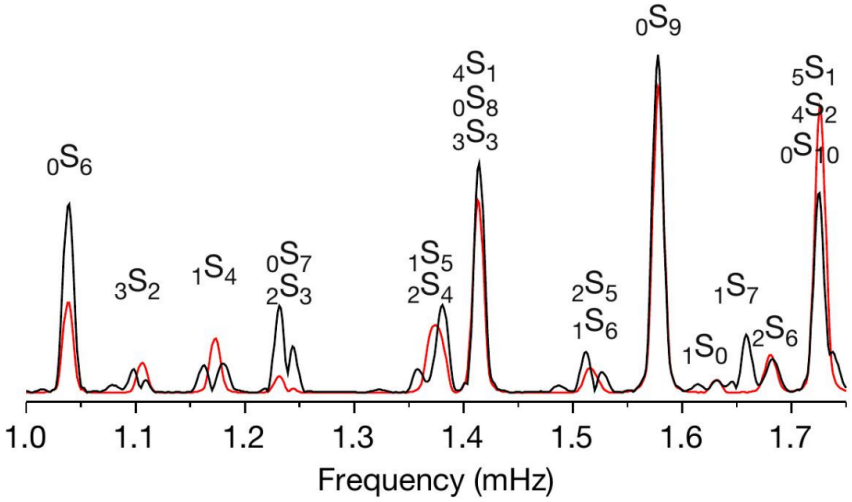

Figure 6.5: **Observations of normal modes after the great Sumatra event 2004.** The black line shows the frequency spectrum of a seismogram observed at station ANMO. In red the theoretical spectrum for a spherical non-rotating Earth model based on normal mode theory is shown. The figure is adapted from Woodhouse and Deuss (2015)

each eigenfunction n the N vectors $\boldsymbol{s}_\alpha$ describe the spatial pattern of the eigenfunction, whereas $e^{i\omega_n t}$ describes the temporal evolution of this special pattern.

$$\Rightarrow -\omega_n^2 m_\alpha \, {}_n\boldsymbol{s}_\alpha + \sum_{\beta=1}^{N} \boldsymbol{V}_{\alpha\beta} \cdot {}_n\boldsymbol{s}_\beta = 0 \tag{6.17}$$

$3N$ eigenvectors ${}_n\boldsymbol{s}_\alpha$, which are orthonormal to each other, can be found:

$$\sum_{\alpha=1}^{N} m_\alpha \, {}_n\boldsymbol{s}_\alpha^* \cdot {}_l\boldsymbol{s}_\alpha = \delta_{nl} \tag{6.18}$$

As the movement of the N particles has $3N$ degrees of freedom the eigenfunctions form a complete orthonormal basis for any movement of the particles.

The Laplace transform (for definition see Appendix B) of Equation 6.16 gives

$$m_\alpha p^2 \bar{\boldsymbol{u}}_\alpha(p) + \sum_{\beta=1}^{N} \boldsymbol{V}_{\alpha\beta} \cdot \bar{\boldsymbol{u}}_\beta(p) = \bar{\boldsymbol{f}}_\alpha(p)\,. \tag{6.19}$$

As the eigenfunctions form a complete basis for the solutions of the system, $\bar{\boldsymbol{u}}_\beta(p)$ can be

written as

$$\bar{\boldsymbol{u}}_\beta(p) = \sum_{n=1}^{3N} a_n(p)\, {}_n\boldsymbol{s}_\beta \,. \tag{6.20}$$

Multiplying Equation 6.20 by $m_\beta\, {}_l\boldsymbol{s}^*_\beta$, taking the sum over β and using Equation 6.18 gives

$$a_l(p) = \sum_{\beta=1}^{N} m_\beta\, {}_l\boldsymbol{s}^*_\beta \cdot \bar{\boldsymbol{u}}_\beta(p), \tag{6.21}$$

where * denotes complex conjugation.

Now Equation 6.19 is multiplied with ${}_n\boldsymbol{s}^*_\alpha$. Afterwards the sum over α is taken by making use of Equations 6.21 and 6.20:

$$p^2 a_n(p) + \sum_{\alpha=1}^{N}\sum_{\beta=1}^{N} {}_n\boldsymbol{s}^*_\alpha \cdot \boldsymbol{V}_{\alpha\beta} \cdot \sum_{l=1}^{3N} a_l(p)\, {}_l\boldsymbol{s}_\beta = \sum_{\alpha=1}^{N} {}_n\boldsymbol{s}^*_\alpha \cdot \bar{\boldsymbol{f}}_\alpha(p) \tag{6.22}$$

This can further be simplified with the help of Equation 6.17. Multiplying Equation 6.17 with ${}_l\boldsymbol{s}^*_\alpha$ and taking the sum over α leads to

$$\sum_{\alpha=1}^{N}\sum_{\beta=1}^{N} {}_l\boldsymbol{s}^*_\alpha \cdot \boldsymbol{V}_{\alpha\beta} \cdot {}_n\boldsymbol{s}_\beta = \omega_n^2 \delta_{nl} \,.$$

Which simplifies Equation 6.22 to

$$\begin{aligned} p^2 a_n(p) + \omega_n^2 a_n(p) &= \sum_{\alpha=1}^{N} {}_n\boldsymbol{s}^*_\alpha \cdot \bar{\boldsymbol{f}}_\alpha(p) \,. \\ \Rightarrow a_n(p) &= \sum_{\alpha=1}^{N} \frac{{}_n\boldsymbol{s}^*_\alpha \cdot \bar{\boldsymbol{f}}_\alpha(p)}{p^2 + \omega_n^2} \end{aligned}$$

If the time evolution of the force has a step like form: $\boldsymbol{f}_\alpha(t) = \boldsymbol{F}_\alpha H(t - t_0)$, its Laplace transform is $\bar{\boldsymbol{f}}_\alpha(p) = \frac{\boldsymbol{F}_\alpha}{p}$ and from Equation 6.20 follows

$$\bar{\boldsymbol{u}}_\beta(p) = \sum_{n=1}^{3N} \left(\sum_{\alpha=1}^{N} \frac{{}_n\boldsymbol{s}^*_\alpha \cdot \boldsymbol{F}_\alpha}{p(p^2 + \omega_n^2)} \right) {}_n\boldsymbol{s}_\beta \,.$$

Taking the inverse Laplace transform finally leads to

$$\boldsymbol{u}_\beta(t) = \sum_{n=1}^{3N} \left(\sum_{\alpha=1}^{N} {}_n\boldsymbol{s}^*_\alpha \cdot \boldsymbol{F}_\alpha \right) \frac{1 - \cos\omega_n t}{\omega_n^2} H(t - t_0)\, {}_n\boldsymbol{s}_\beta \,. \tag{6.23}$$

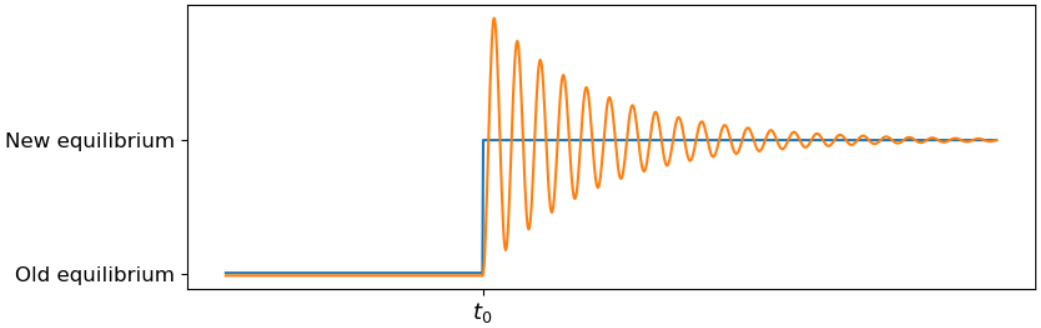

Figure 6.6: **Time evolution of one normal mode.** At time t_0 happens a sudden release of the moment of the earthquake source. From that time on the Earth is oscillating around the new equilibrium.

Up to now I only discussed ideal elastic interaction between the particles. But there is always some friction which leads to attenuation. The attenuation of the n-th eigenmode can be described by the quality factor Q_n. If $Q_n \ll 1$ for all n, Equation 6.23 slightly modifies to

$$\boldsymbol{u}_\beta(t) = \sum_{n=1}^{3N} \left(\sum_{\alpha=1}^{N} {}_n\boldsymbol{s}^*_\alpha \cdot \boldsymbol{F}_\alpha \right) \frac{1 - \cos(\omega_n t) \exp\left(-\frac{\omega_n t}{2Q_n}\right)}{\omega_n^2} H(t - t_0)\, {}_n\boldsymbol{s}_\beta \,. \tag{6.24}$$

Equation 6.24 describes the displacement of the β-th particle in a system of N particles caused by forces $\boldsymbol{F}_\alpha$ applied at some particles α. The forces vary all with the same step function. It can be seen that this displacement is a sum of the displacements ${}_n\boldsymbol{s}_\beta$ related to the n-th n eigenfunction of the system varying in time as $\frac{1-\cos(\omega_n t)\exp\left(-\frac{\omega_n t}{2Q_n}\right)}{\omega_n^2} H(t-t_0)$ which describes a oscillation around the new equilibrium position (see Figure 6.6). The contribution of each eigenmode is calculated by the sum of the scalar products of the forces applied on particle α and the displacement of particle α related to the eigenmode. Now a continuous body like the Earth should be considered. The eigenvectors ${}_n\boldsymbol{s}_\alpha$ then become continuous functions in space ${}_n\boldsymbol{s}(\boldsymbol{r})$. and the number of eigenfunctions gets infinity. The forces at each particle $\boldsymbol{F}_\alpha$ are replaced by the force density $\boldsymbol{f}(\boldsymbol{r})$ and the sum over all particles (the sum over α) is replaced by a volume integral:

$$\boldsymbol{u}(\boldsymbol{r}, t) = \sum_{n=1}^{\infty} \left(\int_V {}_n\boldsymbol{s}^*(\boldsymbol{\xi}) \cdot \boldsymbol{f}(\boldsymbol{\xi}) \mathrm{d}V \right) \frac{1 - \cos(\omega_n t) \exp\left(-\frac{\omega_n t}{2Q_n}\right)}{\omega_n^2} H(t - t_0)\, {}_n\boldsymbol{s}(\boldsymbol{r}) \tag{6.25}$$

The orthonormal relation between the eigenfunctions changes to

$$\int_V \rho(\boldsymbol{\xi})\, {}_n\boldsymbol{s}^*(\boldsymbol{\xi}) \cdot_l \boldsymbol{s}(\boldsymbol{\xi}) \mathrm{d}V = \delta_{nl} \,. \tag{6.26}$$

The force density of an earthquake with hypocentre $\boldsymbol{r}_s$ is the double couple related to the moment tensor $\boldsymbol{M}$ (see also Equation 6.11):

$$f_p(\boldsymbol{\xi}) = -\sum_q M_{pq} \frac{\partial}{\partial \xi_q} \delta(\boldsymbol{\xi} - \boldsymbol{r}_s)$$

The volume integral in Equation 6.25 then turns to

$$\begin{aligned} \int_V {}_n\boldsymbol{s}^*(\boldsymbol{\xi}) \cdot \boldsymbol{f}(\boldsymbol{\xi}) \mathrm{d}V &= -\sum_{p,q} \int {}_n s_p^*(\boldsymbol{\xi}) \frac{\partial}{\partial \xi_q} \delta(\boldsymbol{\xi} - \boldsymbol{r}_s) \mathrm{d}V \\ &= \sum_{p,q} \frac{\partial}{\partial r_q} {}_n s_p^*(\boldsymbol{r}_s) M_{pq} = \sum_{p,q} {}_n \epsilon_{pq}^*(\boldsymbol{r}_s) M_{pq} \,, \end{aligned}$$

where ${}_n\boldsymbol{\epsilon}(\boldsymbol{r}_s)$ is the strain tensor at the hypocentre of the earthquake caused by the displacement of the n-th normal mode. It means that for an earthquake, the excitation amplitude of each eigenmode can be calculated by the so-called double dot product of the moment tensor of the earthquake source and the strain tensor of the normal mode at the hypocentre:

$$\boldsymbol{u}(\boldsymbol{r}, t) = \sum_{n=1}^{\infty} ({}_n\boldsymbol{\epsilon}^*(\boldsymbol{r}_s) : \boldsymbol{M}) \frac{1 - \cos(\omega_n t) \exp\left(-\frac{\omega_n t}{2Q_n}\right)}{\omega_n^2} H(t - t0) \, {}_n\boldsymbol{s}(\boldsymbol{r}) \tag{6.27}$$

with

$$\boldsymbol{a} : \boldsymbol{b} = \sum_{jk} a_{jk} b_{jk}$$

As discussed above for a radial symmetric, self-gravitating Earth the radial variations of the eigenfunctions are ${}_nU_l(r)$, ${}_nV_l(r)$ and ${}_n\phi_l(r)$ and they are degenerate in m. The displacement related to the spheroidal mode (n, l, m) is

$${}_n\boldsymbol{s}_{lm}(r, \vartheta, \varphi) = {}_nU_l(r)\boldsymbol{e}_r Y_{lm}(\vartheta, \varphi) + {}_nV_l(r)\nabla_1 Y_{lm}(\vartheta, \varphi) \,. \tag{6.28}$$

Using the orthonormal relation between eigenfunctions (Equation 6.26), the following normalisation for ${}_nU_l(r)$ and ${}_nV_l(r)$ can be found:

$$\int_V \rho(\boldsymbol{\xi}) \left[{}_nU_l^2(\boldsymbol{\xi}) + l(l+1) \, {}_nV_l^2(\boldsymbol{\xi}) \right] \mathrm{d}V = 1 \tag{6.29}$$

As already discussed when describing the method of Harms (2016) (see Section 6.1.1), for

Table 6.2: **The strain tensor at colatitude $\vartheta = 0$.** The table shows the strain tensor at $\vartheta = 0$ related to the displacement of normal mode (n, l, m) expressed by ${}_nU_l(r)$, ${}_nV_l(r)$ and their radial derivatives ${}_nU_l'(r)$ and ${}_nV_l'(r)$. ${}_nX_l(r) = {}_nV_l'(r) + \frac{{}_nU_l(r) - {}_nV_l(r)}{r}$ and $F = \frac{1}{r}\left(2\,{}_nU_l(r) - l(l+1)\,{}_nV_l(r)\right)$. Each component has to be multiplied by $d_l^{|m|} = \frac{1}{2^{|m|}}\sqrt{\frac{2l+1}{4\pi}\frac{(l+|m|)!}{(l-|m|)!}}$. $'$ denotes the derivative with respect to the radius.

	$m = 0$	$m = \pm 1$	$m = \pm 2$
ϵ_{rr}	${}_nU_l'(r)$	0	0
$\epsilon_{\vartheta\vartheta}$	$\frac{1}{2}\,{}_nF_l(r)$	0	$\frac{{}_nV_l(r)}{r}$
$\epsilon_{\varphi\varphi}$	$\frac{1}{2}\,{}_nF_l(r)$	0	$-\frac{{}_nV_l(r)}{r}$
$2\epsilon_{r\vartheta}$	0	$\mp\,{}_nX_l(r)$	0
$2\epsilon_{r\varphi}$	0	$-i\,{}_nX_l(r)$	0
$2\epsilon_{\vartheta\varphi}$	0	0	$\pm\frac{2i\,{}_nV_l(r)}{r}$

a realistic earthquake the time evolution of the moment tensor is more complicated than a simple step function and can be described with the aid of the source-time function $\dot{m}(t)$. Again the solution for this force evolution is given by the convolution of the solution for the step-like time evolution (Equation 6.27) with the source time function. The radial component of the displacement finally becomes

$$u_r(\boldsymbol{r}, t) = \left(\sum_{n=0}^{\infty} \sum_{l=0}^{\infty} \sum_{m=-l}^{l} ({}_n\boldsymbol{e}^*(\boldsymbol{r}_s) : \boldsymbol{M}) \, \frac{1 - \cos(\omega_n t) \exp\left(-\frac{\omega_n t}{2Q_n}\right)}{\omega_n^2} H(t - t0) \underbrace{{}_nU_l(r) Y_{lm}(\vartheta, \varphi)}_{{}_n\Gamma_{lm}^{u_r}(r,\vartheta,\varphi)} \right) * \dot{m}(t)\,. \tag{6.30}$$

To simplify the form of the strain tensor caused at the hypocentre by the normal mode, it is useful to set up the coordinate system in such a way that the earthquake occurs at the point of colatitude $\vartheta = 0$. Furthermore, the actual geographic north pole is imposed to be located at longitude $\varphi = \pi$ in this new coordinate system (for the transformation to the new coordinate system see Appendix C). Then the strain tensor at $\vartheta = 0$ caused by normal mode (n, l, m) can be derived by inserting Equation 6.28 into the definition of the strain tensor (Equation 4.13) and taking the limits $\varphi \to 0$ and $\vartheta \to 0$ (see for example Masters (lecture notes)). For $m = 0, \pm 1, \pm 2$ the components of the strain tensor at $\vartheta = 0$ expressed by ${}_nU_l(r)$ and ${}_nV_l(r)$ are given in Table 6.2. For $|m| > 2$ the strain tensor at colatitude $\vartheta = 0$ becomes zero for the here considered double couple source. Therefore, the sum over m in Equation 6.30 only has to be evaluated for $-2 \leq m \leq 2$.

The expression I call ${}_n\Gamma_{lm}^{u_r}(r, \vartheta, \varphi)$ in Equation 6.30 describes the radial displacement at the point of measurement produced by the eigenmode (n, l, m). If one is interested in another physical quantity, ${}_n\Gamma_{lm}^{u_r}(r, \vartheta, \varphi)$ must be replaced by the value of this quantity

caused by the eigenmode (n, l, m) at the point of measurement. In this thesis I am mainly interested in the radial component of the gravity vector $g_r(r, \vartheta, \varphi)$ and the gravity gradient tensor $\boldsymbol{T}(r, \vartheta, \varphi)$. For $g_r(r, \vartheta, \varphi)$, ${}_n\Gamma^{g_r}_{lm}(r, \vartheta, \varphi)$ has to be used (see Equations 4.2 and 6.14):

$$ {}_n\Gamma^{g_r}_{lm}(r, \vartheta, \varphi) = \frac{\partial\, {}_n\phi_l(r)}{\partial r} Y_{lm}(\vartheta, \varphi) \tag{6.31} $$

This replacement was also done by Juhel et al. (2018b).

For the six independent components of the gravity gradient tensor T_{xx}, T_{xy}, T_{xz}, T_{yy}, T_{yz}, T_{zz} the following expressions for ${}_n\Gamma_{lm}(r, \vartheta, \varphi)$ have to be used (see Equations 4.6 to 4.11 and 6.14):

$$ {}_n\Gamma^{T_{xx}}_{lm}(r, \vartheta, \varphi) = \frac{1}{r^2}\, {}_n\phi_l(r) \frac{\partial^2 Y_{lm}(\vartheta, \varphi)}{\partial \vartheta^2} + \frac{1}{r} \frac{\partial\, {}_n\phi_l(r)}{\partial r} Y_{lm}(\vartheta, \varphi) \tag{6.32} $$

$$ {}_n\Gamma^{T_{xy}}_{lm}(r, \vartheta, \varphi) = -\frac{1}{r^2 \tan\vartheta \sin\vartheta}\, {}_n\phi_l(r) \frac{\partial Y_{lm}(\vartheta, \varphi)}{\partial \varphi} + \frac{1}{r^2 \sin\vartheta}\, {}_n\phi_l(r) \frac{\partial^2 Y_{lm}(\vartheta, \varphi)}{\partial \vartheta \partial \varphi} \tag{6.33} $$

$$ {}_n\Gamma^{T_{xz}}_{lm}(r, \vartheta, \varphi) = -\frac{1}{r^2}\, {}_n\phi_l(r) \frac{\partial Y_{lm}}{\partial \vartheta} + \frac{1}{r} \frac{\partial\, {}_n\phi_l(r)}{\partial r} \frac{\partial Y_{lm}}{\partial \vartheta} \tag{6.34} $$

$$ \begin{aligned} {}_n\Gamma^{T_{yy}}_{lm}(r, \vartheta, \varphi) =& \frac{1}{r^2 \tan\vartheta}\, {}_n\phi_l(r) \frac{\partial Y_{lm}(\vartheta, \varphi)}{\partial \vartheta} \\ &+ \frac{1}{r^2 \sin^2\vartheta}\, {}_n\phi_l(r) \frac{\partial^2 Y_{lm}(\vartheta, \varphi)}{\partial \varphi^2} + \frac{1}{r} \frac{\partial\, {}_n\phi_l(r)}{\partial r} Y_{lm}(\vartheta, \varphi) \end{aligned} \tag{6.35} $$

$$ {}_n\Gamma^{T_{yz}}_{lm}(r, \vartheta, \varphi) = -\frac{1}{r^2 \sin\vartheta}\, {}_n\phi_l(r) \frac{\partial Y_{lm}(\vartheta, \varphi)}{\partial \varphi} + \frac{1}{r \sin\vartheta}\, {}_n\phi_l(r) \frac{\partial^2 Y_{lm}(\vartheta, \varphi)}{\partial \varphi \partial r} \tag{6.36} $$

$$ {}_n\Gamma^{T_{zz}}_{lm}(r, \vartheta, \varphi) = \frac{\partial^2\, {}_n\phi_l(r)}{\partial r^2} Y_{lm}(\vartheta, \varphi) \tag{6.37} $$

6.2.2 Tests and problems of the simulations

To compute gravity gradients of PEGS with the method of normal mode summation, I first compute the normal modes for a radial symmetric, spherical, self gravitating Earth with the aid of the software Mineos. For the radial structure of the Earth the PREM model (Dziewonski and Anderson 1981) is used. In a second step I use a python program written by myself to perform the summation of Formula 6.30 or their equivalents for gravity or gravity gradients. In the following, I will give an introduction to the Mineos software, present my python program, describe some validation tests and finally point out the problems which prevented me from computing the gradients of PEGS with this method.

The Mineos software

Mineos is a software package to compute synthetic seismograms based on normal mode computation and normal mode summation. It was written by Guy Masters based on former codes by J. Freeman Gilbert and John Woodhouse. It consists of two main parts: first the computation of normal modes for a given frequency range and specified mode indices $(l_{\min}, l_{\max}, n_{\min}, n_{\max})$, second the summation for a specified event and a given receiver. Each of these parts consists of two FORTRAN programs. For the normal mode computation they are called `minos_bran` and `eigcon`, for the normal mode summation `green` and `syndat`.

The main normal mode calculation is done by `minos_bran`. It takes the following input parameters: a 1D Earth model, containing material parameters such as density P- and S-wave velocities, the type of oscillation (radial, toroidal or spheroidal modes), the frequency range and the range of l and n. Furthermore, the accuracy of the integration of the differential equations and a frequency ω_{grav} have to be given. For all eigenmodes of frequencies above ω_{grav} only the equation of motion and Hooke's law without the Poisson equation will be solved. For our calculations it should be set to the same value as $\omega_{\max}$. Based on these inputs, `minos_bran` determines all modes in the given ranges of ω, l and n and calculates their eigenfrequencies ${}_n\omega_l$, their attenuation coefficient ${}_nQ_l$ and their eigenfunctions. The eigenfunctions are returned as FORTRAN binary files. In the case of spheroidal modes in these binary files ${}_nU_l(r)$, ${}_nV_l(r)$ and ${}_n\phi_l(r)$ as well as their first derivatives are given at discrete values of r. In the case of radial modes only ${}_nU_l(r)$ and its derivatives are given, as ${}_nV_l(r)$ and ${}_n\phi_l(r)$ are zero in this case. The other output parameters are given in an ASCII table. To get a portable output, `eigcon` is used to convert the output of `minos_bran` to a portable database. Furthermore, `eigcon` renormalises the eigenfunctions to

$$\omega^2 \int_V \rho(\boldsymbol{\xi}) \left[{}_nU_l^2(\boldsymbol{\xi}) + l(l+1)\, {}_nV_l^2(\boldsymbol{\xi}) \right] \mathrm{d}V = 1\,. \tag{6.38}$$

The calculation of synthetic seismograms is also divided in two parts. First `green` calculates six Green's functions for each component of the moment tensor for an earthquake happening at a given location and measured at specified receivers. Afterwards `syndat` calculates the double dot product between the Green's functions and the moment tensor and convolves the result with a triangle source time function of a given half width. By default the output of `syndat` is given as acceleration, but if specified, also displacement or velocity can be given. In the output of `syndat` not only the ground motion is considered, but the sum of every signal of the earthquake that a seismometer measures. For the

vertical component these are the ground acceleration and two other signals: the change in gravity due to a displacement of the instrument in the static gravity field and the gravity signal induced by the density changes related to the earthquake. The last one is the signal that I want to model. After the arrival of the P-wave for not very low frequencies only the ground acceleration is relevant. For the vertical component of mode ${}_8S_1$ which has a frequency of 2.871 mHz the ground motion already represents 99.1 % of the signal, whereas for mode ${}_0S_2$ with a frequency of 0.309 mHz it represents only 81.5 % of the signal, the remaining 18.5 % are related to the change in gravity due to the displacement of the instrument in the static gravity field and the gravity signal induced by the density change related to the earthquake.

Since 2006 the Mineos code is distributed by the Computational Infrastructure for Geodynamics (CIG) (Masters 2014). A more detailed introduction to the software package and how to use it can be found in the Mineos manual (Masters et al. 2014). The theory behind Mineos is explained in detail by Masters (lecture notes).

The Python program for normal mode summation

The normal mode summation of Mineos (`green` and `syndat`) only gives the sum of the ground acceleration, the gravity change due to a displacement of the instrument in the static gravity field and the gravity signal induced by the density change related to the earthquake. However, for the study of gravity gradients of PEGS we need the last one separated from the two others. To calculate it, I wrote my own python program for normal mode summation. It can be seen as a replacement for `greens` and `syndat`. The computation of the normal mode catalogue still has to be done with `minos_bran` and `eigcon`, whose output is used as input for the python program. The python program is a direct implementation of Formula 6.30. *Attention should be paid to the special normalisation of Mineos (Equation 6.38) which differ by a factor of ω^2 from the normal normalisation (Equation 6.29). Therefore, the eigenfunctions of Mineos contain a factor $\frac{1}{\omega}$. As they occur twice in Equation 6.30 (in the stain tensor and in ${}_n\Gamma_{lm}(r,\vartheta,\varphi)$) this cancels out the factor $\frac{1}{\omega^2}$ in the time-dependent part of Equation 6.30.*

There are three slightly different versions of the normal mode summation program, one for vertical displacement, one for vertical gravity change and one for the six independent components of the gravity gradient tensor. They only differ in the calculation of ${}_n\Gamma_{lm}(r,\vartheta,\varphi)$ (See comments on Formula 6.30.) The code of the programs can be found in Appendix E containing the three main programs and several modules needed by the main programs:

- to read the input parameters and the eigenfunction catalogue created with `minos_bran` and `eigcon`
- to do computations related to time series
- to convert between SI units and the unit system of Mineos
- to find the coordinates of the receiver in epicentric coordinates and to rotate the moment tensor to a local south oriented coordinate system (for further explanation and formulas see Appendix C)
- to calculate the double dot product between the moment tensor and the strain tensor
- to interpolate the eigenfunctions ${}_nU_l(r)$, ${}_nV_l(r)$, ${}_n\phi_l(r)$ which are given at discrete points to the source dept
- to calculate the value of ${}_n\Gamma_{lm}(r, \vartheta, \varphi)$ at the receiver

Testing the program

To validate the implementation of Formula 6.30 I first perform normal mode summations for verical displacement for the first 6 h = 21 600 s after the onset of the Tohoku-Oki earthquake at three different observatories: the Black Forest Observatory in Germany (BFO), the South African Geodynamic Observatory in Sutherland (SUR) and the observatory in Nana, Peru (NNA). For this first test a normal mode catalogue with all radial and spheroidal modes up to 8 mHz is used. It is computed with `mios_bran` and `eigcon`. Toroidal modes are not relevant for vertical displacement. The frequency range is the one of long period surface waves. Numerical differentiation of the outputs of the normal mode summation gives ground velocities. The ground velocities are convolved with the instrument responses of the seismometers at the observatories to get theoretical measurements. These are compared to true measurements after applying the same band-pass Butterworth filter (order 4, corner frequencies 1 mHz and 5 mHz) on both, the measurements and the simulated signal. Furthermore, I simulate the vertical ground velocities with the help of the Mineos subprograms `greens` and `syndat` based on the same normal mode catalogue as for the python program. This results are also convolved with the instrument response, filtered and compared to the others. The comparison can be seen in Figure 6.7. At each of the three stations it can be seen that the order of magnitude of all three signals and their general form is the same. But in the 1500 s long sections on the right of Figure 6.7, differences between the signals can be observed. The differences in amplitude compared to

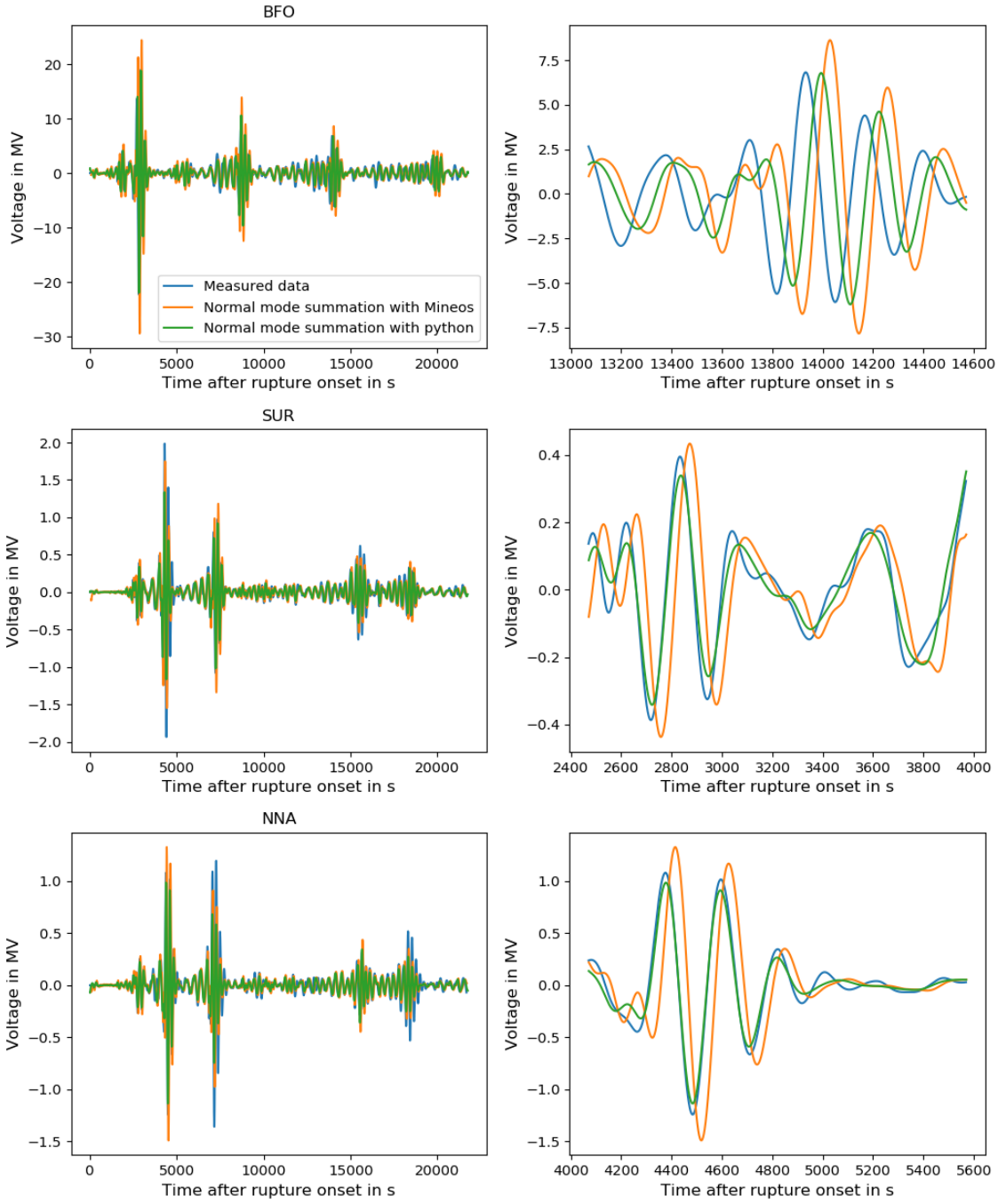

Figure 6.7: **Comparison of theoretical and measured seismograms for the Tohoku-Oki earthquake**

the measured signal reach about 30 % for both simulations. Additionally, we can observe time shifts between the signals which reach 75 s for the normal mode summation with python and 100 s for the normal mode summation with Mineos. In general the results of the normal mode summation with python fit better to the measured data than the results of the normal mode summation with the Mineos subprograms. The results of the normal mode summation with python have especially high agreement to the measurements at the beginning of the time series, whereas the time shift occurs only for later times. This could be due to the simplified Earth model: For a true rotating elliptical Earth with a three dimensional distribution of materials the eigenfrequencies are slightly different than for the spherical non-rotating Earth with only radial variations in the material considered in the computation. These differences become more and more relevant with time.

Theoretically, the normal mode summation with python and with the subprograms of Mineos should give the exactly same results, as the same formula should be implemented and the same moment tensor, half time duration, event and station coordinates are used. Therefore, the differences between the results of the normal mode summations of Mineos and python are surprising. To analyse this further, I also computed "normal mode summations" with only one mode and simplified moment tensors with only one component, but the differences between the output of `syndat` and the python program got even worse and could reach up to a factor of four. However, no systematic difference can be found. It was for example not the case, that the amplitude of the output of one program is always bigger than the amplitude of the output of the other program. There has to be a mistake in the outputs of the normal mode summation with Mineos or the one with python. From the comparison with real data, I would expect the output of the Mineos normal mode summation to be wrong, the reason might be a wrong usage of the `greens` and `syndat` program. The reason for the discrepancies between the python and the Mineos results could not be finally resolved and has to be further investigated. The results of the normal mode summation with python have a good agreement to the measured. Therefore, the python program is used in the following.

In the next step, the normal mode summation with python is tested for the vertical component of gravity. The same normal mode catalogue as before (up to 8 mHz) is used. The signals are calculated for the IC MDJ station (44.62°N, 129.59°E) in order to compare the results to Figure 2 of Juhel et al. (2018b), who also used this station. For the computation of the vertical gravity anomaly ${}_n\Gamma^{u_r}_{lm}(r,\vartheta,\varphi)$ has to be exchanged by ${}_n\Gamma^{g_r}_{lm}(r,\vartheta,\varphi)$ in Formula 6.30. It contains the first derivative of the eigenfunction ${}_n\phi_l(r)$ at the radius of the receiver which is in our case the Earth radius r_0. There are two possibilities to get the value of $\frac{\mathrm{d}\,{}_n\phi_l(r)}{\mathrm{d}r}|_{r=r_0}$: The straightforward one is to use the value

given as a direct output of `eigcon`. Another one, proposed by Masters (lecture notes), is to make use of the fact that the gravity potential is harmonic outside the Earth and measurements are taken above the Earth's surface. This leads to the relation

$$\frac{\mathrm{d}\,{}_n\phi_l(r)}{\mathrm{d}r}|_{r=r_0} = \frac{(l+1)}{r_0}\,{}_n\phi_l(r=r_0)\,. \tag{6.39}$$

So $\frac{\mathrm{d}\,{}_n\phi_l(r)}{\mathrm{d}r}|_{r=r_0}$ can also be calculated based on the values `eigcon` gives for ${}_n\phi_l(r=r_0)$. In theory, the two values should be the same, but I observe that they are not. I perform the normal mode summation with both of these values and filter the results with a Butterworth low-pass filter (order 4, corner frequency 7 mHz). *It should be noted that the corner frequency of 7 mHz might be to high to avoid the Gibb's phenomena completely, but when applying a filter with a lower corner frequency the comparison to the results of Juhel et al. (2018b) is not possible anymore.* The results can be seen in Figure 6.8. For both methods the order of magnitude and the general form of the signal are very similar. The maximum peak occurs at about 500 s after the rupture onset and has a maximum value of 8 µGal for the first method and 10 µGal for the second method. But the waveforms calculated with the two different values of $\frac{\mathrm{d}\,{}_n\phi_l(r)}{\mathrm{d}r}|_{r=r_0}$ clearly differ from each other. However, the general pattern of the gravity change and the size of magnitude are similar to the ones presented in Figure 3 of Juhel et al. (2018b) for both values of $\frac{\mathrm{d}\,{}_n\phi_l(r)}{\mathrm{d}r}|_{r=r_0}$ despite the fact that the high frequencies are missing in my simulations. Furthermore, the maximum peak occurs a bit earlier in Juhel et al. (2018b) at about 425 s. This is very likely related to the time shift I introduce by filtering the data. In general it should be kept in mind that what is mainly seen in these figures are not PEGS but the gravity change when seismic waves have already reached the station, so a signal that will not be measurable. Additionally, it is only the gravity change and not the ground acceleration induced by the gravity change.

For the normal mode summation for the six components of the gravity gradient tensor I need not only the first but also the second derivative of the eigenfunction ${}_n\phi_l(r)$ at the Earth's surface. This is not given directly as an output of `eigcon` and besides that it is not continuous at the Earth's surface. As measurements are taken above the Earth's surface, where the potential is harmonic it is reasonable to use Equation 6.39 for the first derivative and

$$\frac{\mathrm{d}^2\,{}_n\phi_l(r)}{\mathrm{d}r^2}\Big|_{r=r_0} = \frac{(l+2)(l+1)}{r_0^2}\,{}_n\phi_l(r=r_0) \tag{6.40}$$

for the second derivative. With these values for the first and second derivative of ${}_n\phi_l(r)$ at the Earth's surface I perform a normal mode summation for all components of the gravity gradient tensor at the MDJ station. I still use all spheroidal modes up to 8 mHz

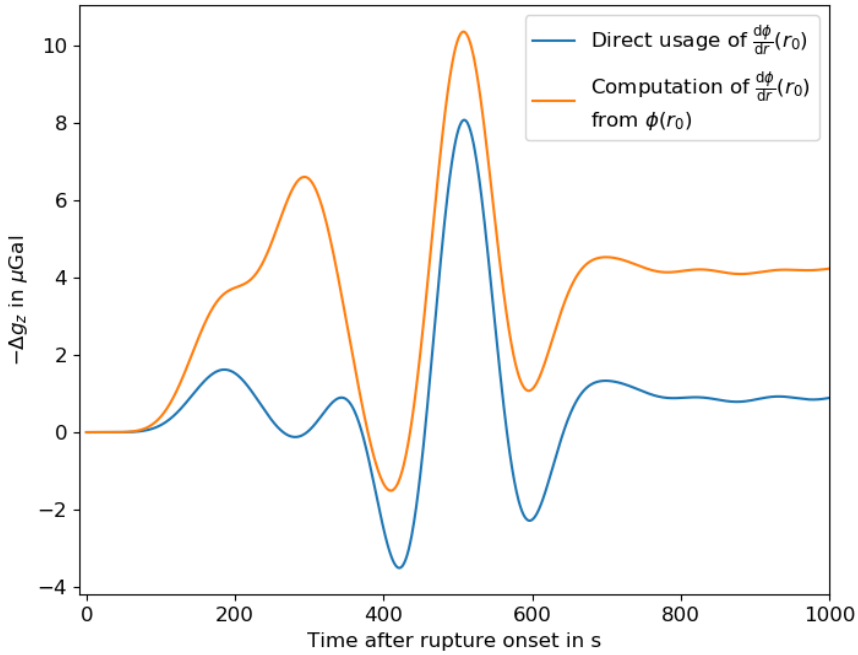

Figure 6.8: **Gravity change at station MDJ during the Tohoku-Oki earthquake calculated with normal mode summation.** The summation is done for eigenmodes up to an eigenfrequency of 8 mHz, afterwards they are low-pass filtered below 7 mHz. For the signal in blue the values for the derivative of ${}_n\phi_l(r)$ at the Earth's surface are directly taken from the output of `eigcon`. For the signal in orange they are calculated from the values of ${}_n\phi_l(r = r_0)$ given by `eigcon`.

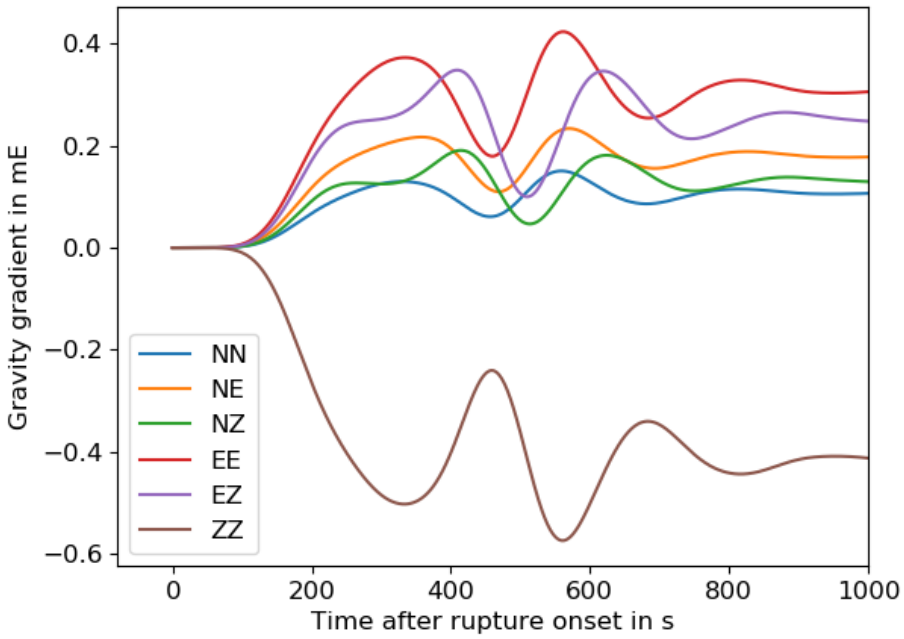

Figure 6.9: **Change in gravity gradient at station MDJ during the Tohoku Oki earthquake calculated with normal mode summation.** The summation is done for eigenmodes up to an eigenfrequency of 8 mHz, afterwards they are low-pass filtered below 4 mHz.

and low-pass filter them afterwards below 4 mHz. The results can be seen in Figure 6.9. Most of the components also have their main peak between 400 s and 500 s and they reach up to 0.6 mE, but again these are not gravity gradients of PEGS but changes in gravity gradients after the seismic waves have reached the station. For validation of the code, I also computed the time series of the trace of the gravity gradient tensor. It vanished below some numerical uncertainties ($\approx 1 \times 10^{-16}$ mE). However, it has to be borne in mind that the trustworthiness of the computations of the gravity gradients suffers from the uncertainty in the computation of the first derivative of ${}_n\phi_l(r)$, which also propagate to the second derivative.

Besides all these problems of the normal mode summation, the main challenge is to compute a normal mode catalogue for high frequencies with Mineos. All the described tests were performed only up to a frequency of 8 mHz which is equivalent to a minimum period of 125 s. For stations, for which I will simulate the gravity gradients associated to PEGS with the method of Harms (2016) in Chapter 7 the pre P-wave window is only between 3 s and 120 s long. As a consequence, higher frequencies might be needed. Further, due to the Gibb's phenomena the normal mode summation should always be performed up to higher frequencies than the needed ones and afterwards the signal should be filtered with a low pass filter to avoid ringing in the seismogram at the cut-off frequency (personal

communication by Rongjiang Wang). Therefore, we even need higher frequencies than the highest frequency we expect in the signal.

Juhel et al. (2018b) wrote in their paper, that they have calculated all eigenmodes and their overtones up to harmonic degree $l = 2695$ and a maximum frequency of 200 mHz which is equivalent to a minimum period of 5 s. On the other hand in the manual of the Mineos package it is written that Mineos works well for low frequency but not for periods of a few seconds. This is also what I observed: By slightly increasing the maximum frequency and adjusting $n_{\max}$ and $l_{\max}$ in a way that all modes up to the maximum frequency are computed, the program could not complete the computation for a maximum frequency of 80 mHz. For a maximum frequency of 50 mHz the computation time is about 7 min, but for a maximum frequency of 80 mHz the program was still running after three days. Therefore, I assume that it enters into an infinite loop somewhere. Probably Juhel et al. (2018b) have used a modified version of Mineos, which is able to calculate eigenmodes for higher frequencies. Unfortunately I do not have access to this version. Therefore, I did not continue simulating gravity gradient of PEGS by normal mode summation.

As a summary, the python code I wrote during this thesis is able to perform normal mode summation for vertical displacement, vertical gravity and all components of the gravity gradient tensor, if a normal mode catalogue is given. This normal mode catalogue can be calculated with the `minos_bran` and the `eigcon` program of Mineos. The output for vertical displacement differs from the one I calculated with the normal mode summation of Mineos, but it agrees well with measured data. This could be due to a wrong usage of the `green` and `syndat` subprograms. For the normal mode summation of vertical gravity and the gravity gradient tensor, it is not clear which are the correct values of the first and second derivatives of ${}_n\phi_l(r)$ at the Earth's surface. However, the magnitude of the vertical gravity change and the general pattern compares quite well to the signal shown in Juhel et al. (2018b) and the trace of the gravity gradient tensor was zero. The major problem remains to compute normal modes for high frequencies (> 50 mHz).

Chapter 7

Results of the simulations

In this Chapter I present gravity gradient signals of prompt elasto-gravity signals (PEGS) for the Tohoku-Oki earthquake simulated with the method of Harms (2016). The results are compared to the noise spectrum of gravity gradiometers presented in Chapter 5 to estimate if gradiometers that exist or are under development could have detected PEGS of the Tohoku-Oki earthquake. Furthermore, the capabilities of gravity gradiometers are compared to those of gravity strainmeters in the context of the detection of PEGS.

7.1 Time series of individual stations

I calculated time series of all six components of the gravity gradient tensor at 55 virtual stations for PEGS of the Tohoku-Oki earthquake. They are located on five lines starting from the epicentre, two in the direction of the strike, two perpendicular to the strike and one in a direction 45° away from the line of strike. The distance to the epicentre varies from 10 km to 1000 km: 10 km, 25 km, 50 km, 100 km, 150 km, 250 km, 375 km, 500 km, 625 km, 750 km and 1000 km. The signals are simulated with a sampling interval of 0.1 s by applying the method of Harms (2016) as described in Section 6.1.2. The moment tensor and the half width of the source time function are taken from the the global CMT catalogue and can be found in Chapter 2.

First, I discuss the angular dependence of the signals. In Figure 7.1 all time series at the stations 250 km away from the epicentre are shown. They are all 32.1 s long, as for all of them the P-wave arrives after 32.1 s. That follows from the distance and the chosen P-wave velocity. It can be seen, that in general the signals of the gradients are smaller at the two stations in the direction of the strike, than at the other three stations. Furthermore, the signals in the direction of compression, that is the direction of the Japanese mainland, are bigger than in the direction of dilatation, that is the direction of the open Pacific ocean. The largest signals occur at the station in the westward direction perpendicular to the strike (Station (c)), where they reach up to 0.6 mE. These characteristics are true for the overall signal but not for each individual component of the gravity gradient, as

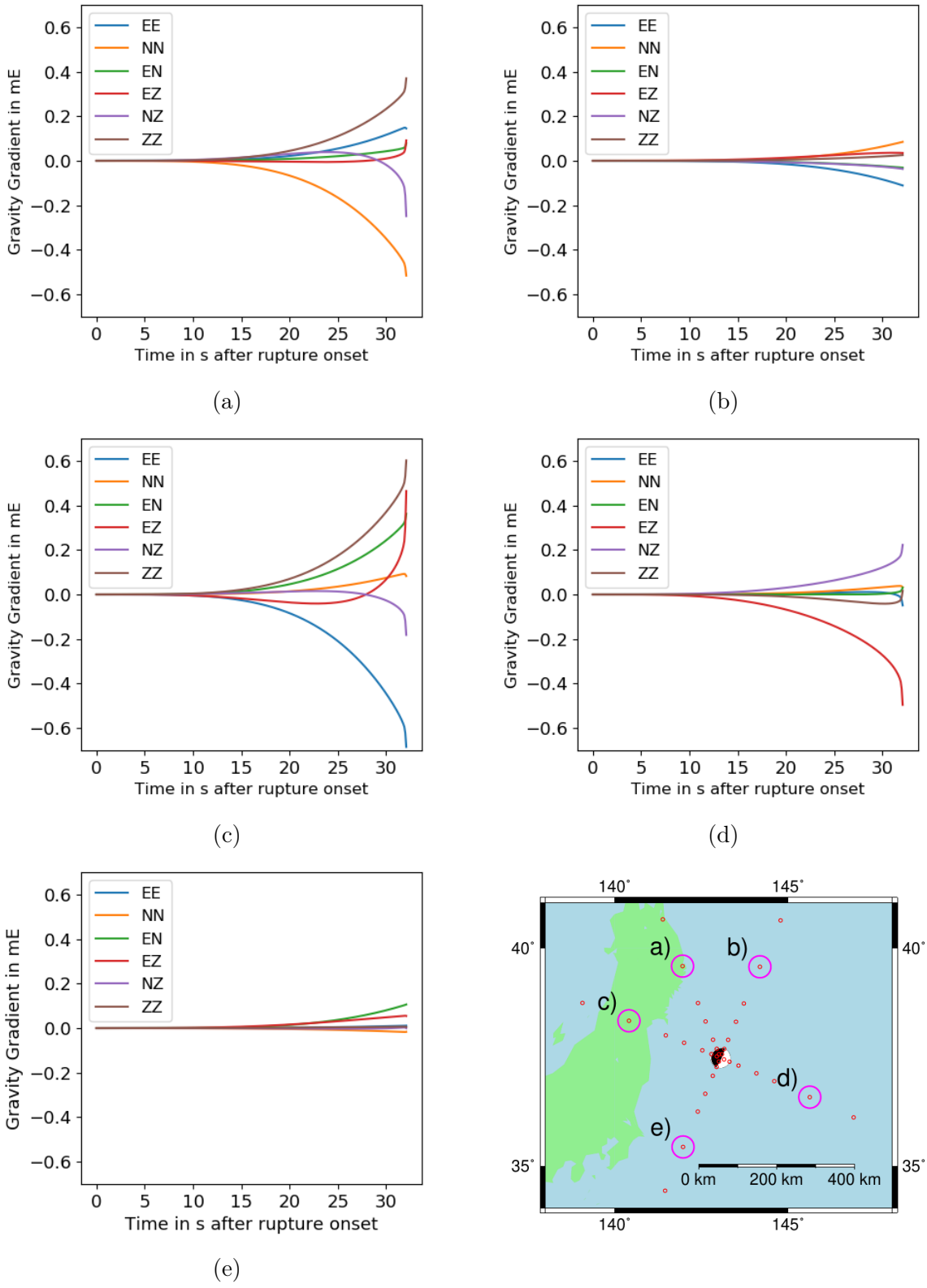

Figure 7.1: **Angular dependence of gravity gradients of PEGS.** The figure shows gravity gradients of PEGS induced by the Tohoku-Oki earthquake at stations 250 km away from the epicentre. The stations are located at 5 different directions, shown on the map.

the highest amplitude components change with the direction. For example at the station in the north direction of the strike (Station (b)) the EE-component is bigger than in the east direction perpendicular to the strike (Station (d)). The reason is, that at Station (b) the EE- and the NN-component are the most prominent ones, whereas at Station (d) the EZ- and the NZ-components have the biggest amplitudes.

Since I observed that the signals are in general the largest in the westward direction perpendicular to the strike (direction of Station (c)), I will focus on these signals to study the dependence on the distance from the epicentre. In Figure 7.2 all time series for stations in this direction are shown with the same time- and gradient-scale. It can be observed, that the length of the time series increases with increasing distance, as the P-wave arrives later. The amplitudes of the signals increase from 10 km to 25 km, where they nearly reach 40 mE. For larger distances they decrease rapidly. As already seen in Figure 7.1 they only reach 0.6 mE at a distance of 250 km. This is very different from the behaviour of PEGS measured with gravimeters or seismometers. For these, as discussed in Section 3.1, Juhel et al. (2018b) found increasing signal amplitudes up to distances of 1000 km to 1500 km. Probably, this difference is linked to the $\frac{1}{r^3}$ decay of gravity gradients of point sources compared to a $\frac{1}{r^2}$ decay of gravity of point sources, where r is the distance to the source.

To get a better idea of the form of the signals, the same time series as in Figure 7.2 are shown again in Figure 7.3, this time with different time- and gradient scales. Here I find it remarkable that the form of the signals is nearly the same for all stations further than 100 km away from the epicentre except for increasing time length and decreasing signal amplitude: For all of them the EE-component is the biggest negative component and the ZZ-component is the biggest positive one. For the three stations closer than 100 km to the epicentre the behaviour of the signals is completely different at each station. For the stations at 25 km and 50 km the signal amplitudes increase rapidly at the very end of the time series. Here it should be taken into account that due to the implementation of the program the last data point of each time series could also be after the arrival of the P-wave, as the last data point is chosen to be as close as possible to the arrival of the P-wave, no matter if it is before or after. However, at least for the station at a distance of 25 km the steep increase already starts one data point before.

To complete the overview of time series at different locations, the signals for all stations in the other directions can be found in Appendix D. The general findings are confirmed by these plots: The amplitudes of the gradients increase up to a distance of 25 km and decrease rapidly afterwards. The length of the time series increase with increasing distance. The change in the forms of the signals is much smaller for stations more than 100 km away from the epicentre than for the closer stations. However, for some direc-

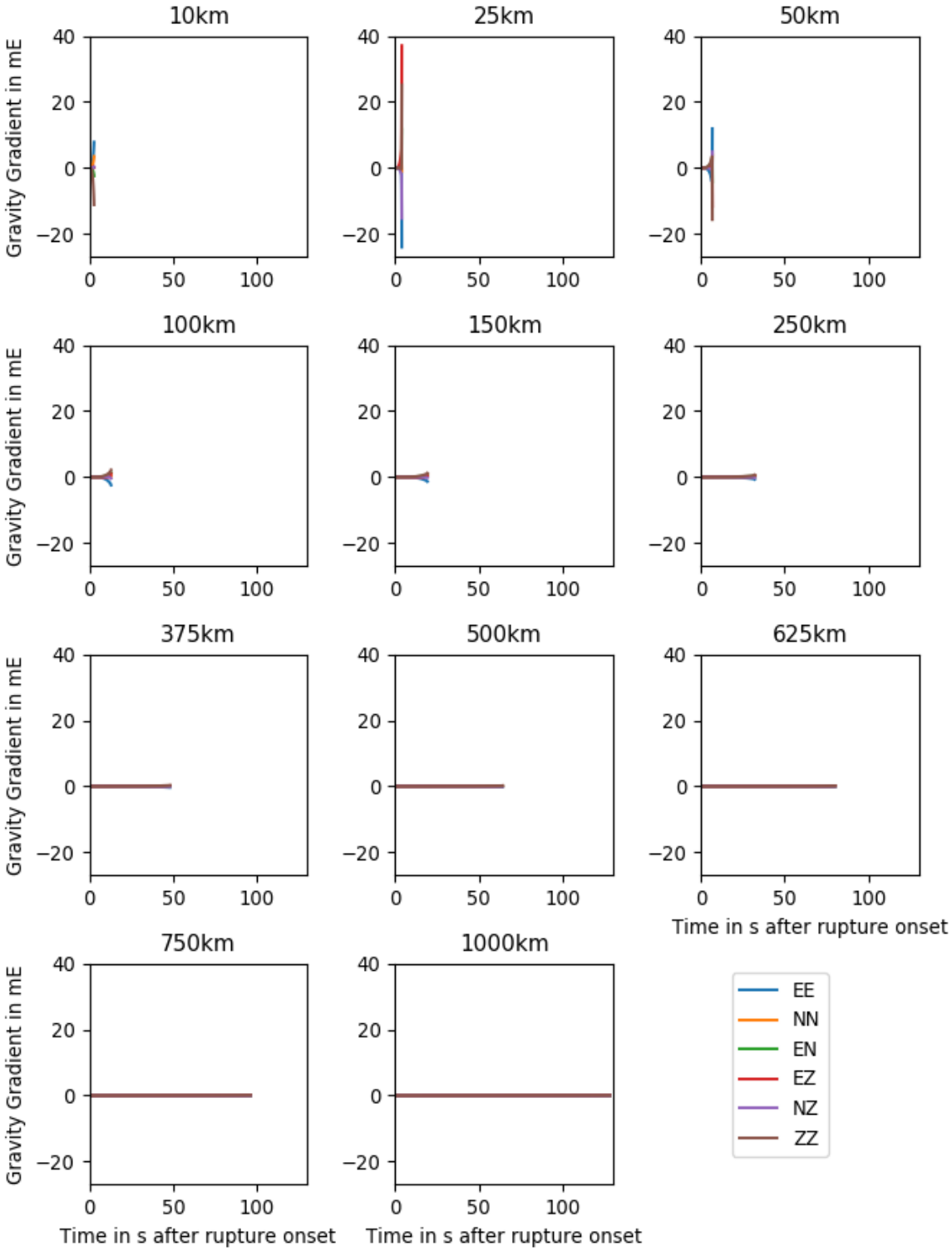

Figure 7.2: **Distance dependence of gravity gradients of PEGS - Amplitude and time span.** The figure shows gravity gradients of PEGS induced by the Tohoku-Oki earthquake at stations in the westward direction perpendicular to the strike (direction of Station (c) in Figure 7.1). The stations are located at eleven different distances from the epicentre, indicated in the titles of the subplots. All plots have the same time- and gradient scale.

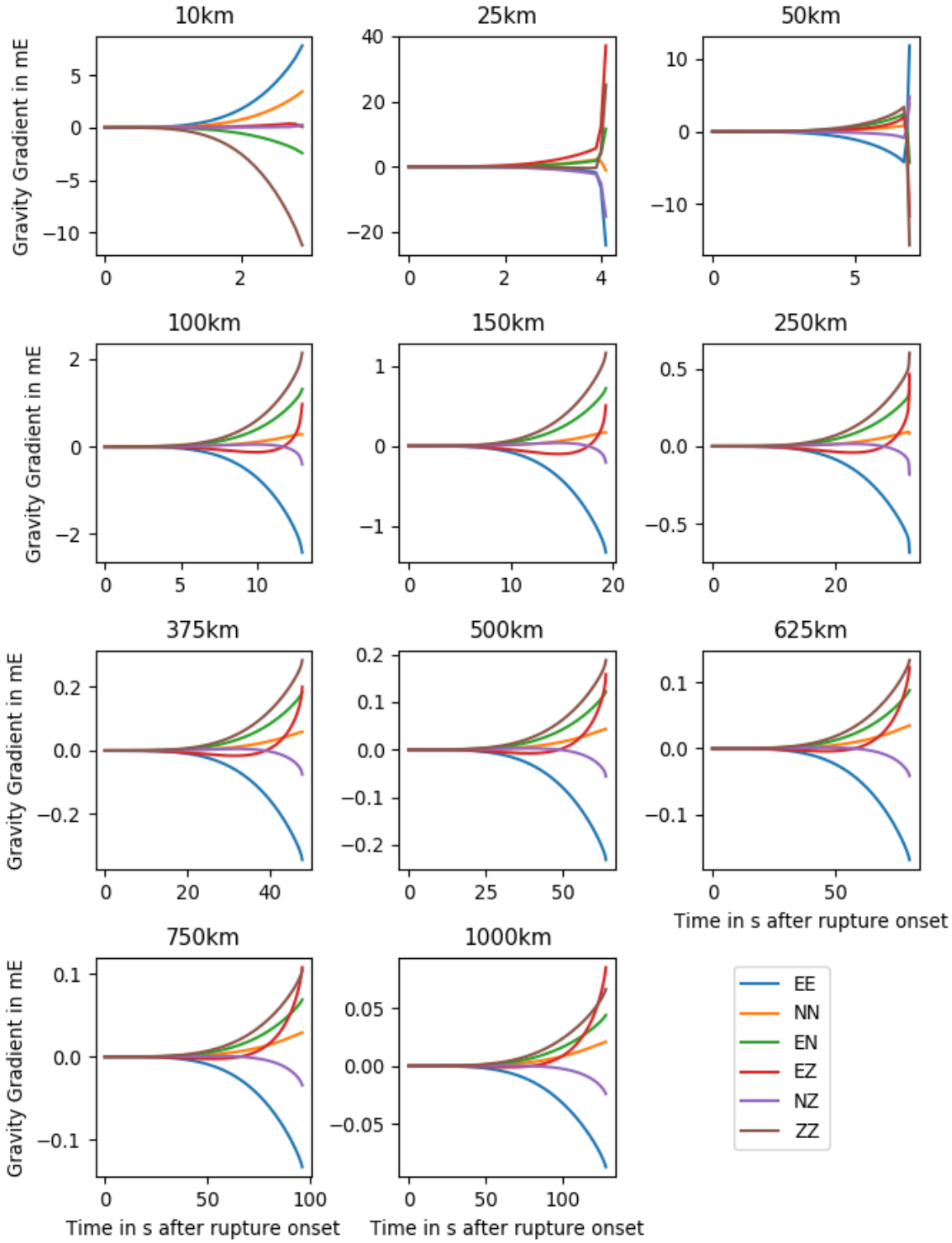

Figure 7.3: **Distance dependence of gravity gradients of PEGS - Pattern of the signals.** The figure shows gravity gradients of PEGS induced by the Tohoku-Oki earthquake at stations in the westward direction perpendicular to the strike (direction of Station (c) in Figure 7.1). The stations are located at eleven different distances from the epicentre, indicated in the titles of the subplots. The plots have different time- and gradient scales.

tions significant changes in the form of the signals, sometimes even a change of sign, are still happening more than 100 km away from the epicentre. But if those changes occur at further distances they are happening very slowly from one station to the next (See for example EE-component in Figure D.3, which shows the signals in the east direction perpendicular to the strike).

Additionally, for each chosen distance the signals are smaller in the direction of the strike, than perpendicular to it. The observation that the signals are bigger in the direction of compression is not confirmed for all distances. Especially, for the stations the furthest away from the epicentre they also become slightly bigger for the direction of dilatation than for the direction of compression.

7.2 Maps of signal amplitudes immediately prior to P-wave arrival time

Figure 7.4 shows maps of the amplitudes of each component of the gravity gradient tensor immediately prior to the P-wave arrival for the Tohoku-Oki earthquake. They are computed on a circular grid with the epicentre at the centre. The radial distance between the computation points is 25 km, the angular distance is 10°. Gravity gradients are computed up to a distance of 250 km. To avoid the described problem that the last data point of each time series can be just before or just after the P-wave arrival, I choose the second to last data point.

For all components in all directions a decrease of the amplitudes with distance can be seen for stations further than 75 km away from the epicentre. The biggest amplitudes always occur at stations 25 km away from the epicentre. Especially the angular pattern of the EE-, the ZZ- and the EZ-component confirm the finding, that signal amplitudes are larger perpendicular to the strike than in the direction of the strike. However these patters can not be clearly observed in the other components. Closer investigation of these maps are needed.

7.3 Comparison to the noise spectrum of gradiometers

In this section I would like to compare the simulated gravity gradients of PEGS presented in the last section to the noise spectrum of the gradiometers presented in Chapter 5. This will lead to an estimation of the detectability of gravity gradients of PEGS with

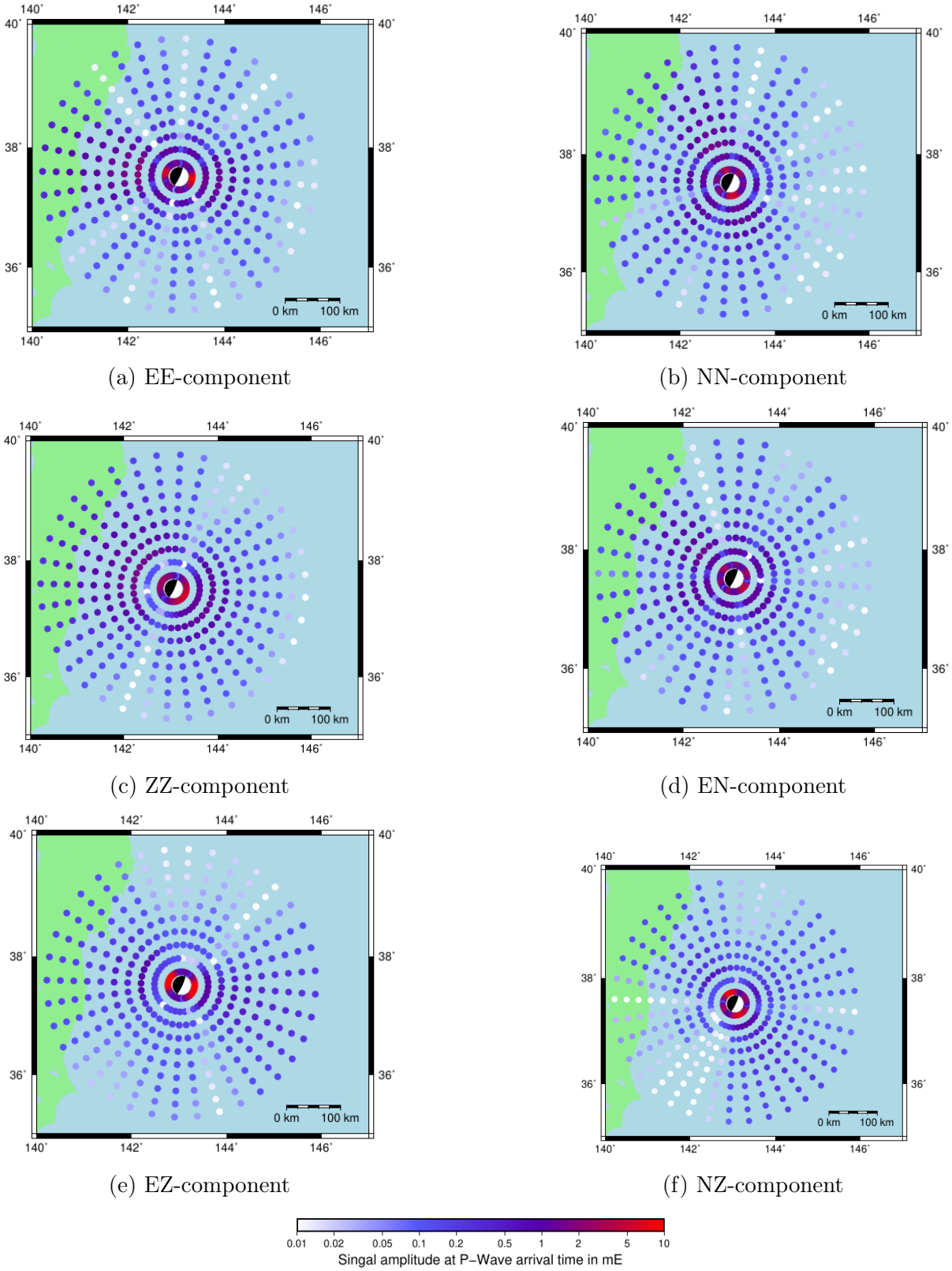

(a) EE-component

(b) NN-component

(c) ZZ-component

(d) EN-component

(e) EZ-component

(f) NZ-component

Figure 7.4: **Map of signal amplitudes at P-wave arrival time** The figure shows a map of the amplitudes of each component of the gravity gradients at the p-wave arrival time. The signals are shown for the Tohoku-Oki earthquake up to 250 km away from the epicentre of the earthquake. The white points can also indicate signal amplitudes lower than 0.01 mE.

gradiometers that exist or are under development.

The important characteristics of a signal in the context of its detectability are both amplitude and frequency content. If the frequency content of the noise and the signal are different, the noise can be filtered out without altering the signal. This is not possible if the frequency content of the signal is in a frequency band where the noise shows a high PSD. Therefore, a signal with low amplitude could be easier to detect than a signal with high amplitude, if they have a different frequency content. For this reason, it is likely that the gravity gradients with the biggest amplitudes, about 25 km away from the source, are not the easiest to detect. They have a very short timescale (for the sharp increase the time scale is less than one second) and for most of the instruments the noise increases for frequencies above 100 mHz (see Figure 5.3). Therefore, it is important to look not only at the simulated time series with the maximum amplitude, but at time series for all the eleven different distances, when analysing the detectability of gravity gradients of PEGS. In the following, I will do this analysis for each of the gradiometers presented in Chapter 5. I concentrate on the signals in the westward direction perpendicular to the strike, as they had the biggest amplitudes and the same time scales as for the other directions.

I will first look at the gradiometers with the lowest instrumental noise levels, presented in Chapter 5, which are the gradiometers developed at the University of Maryland (Moody et al. 2002 and Griggs et al. 2017). For all frequencies below 300 mHz the instrument of Griggs et al. (2017) has a lower noise amplitude than the instrument of Moody et al. (2002). So, for all signals which have a time scale of more than 3 s, there is a better chance of detectability with the instrument of Griggs et al. (2017). As this is the case for most of the stations I will now first study the detectability with the instrument of Griggs et al. (2017) in more detail. Nevertheless, for the three closest stations to the epicentre, the signals are not longer than 3 s. Therefore, afterwards, I will study the detectability of the gravity gradients at these stations with the instrument of Moody et al. (2002). A long time series of noise of the instrument of Griggs et al. (2017) for all the diagonal gradient components was simulated from the noise PSD using the method of Broersen and Waele (2003). In the following, I always use pieces of this time series of the required length. If a time series of filtered noise is needed, the filter is applied to the full time series and a piece of the required length is taken from the middle to avoid undesirable edge effects of the filtering at the start and the end of the time series.

In Figure 7.5 the EE-components of the gravity gradients at stations in the westward direction perpendicular to the strike are shown once without and once with the additive noise of the instrument of Griggs et al. (2017). Additionally, the pure noise is shown. The EE-component is chosen, as it is the biggest one in this direction. It can be seen, that

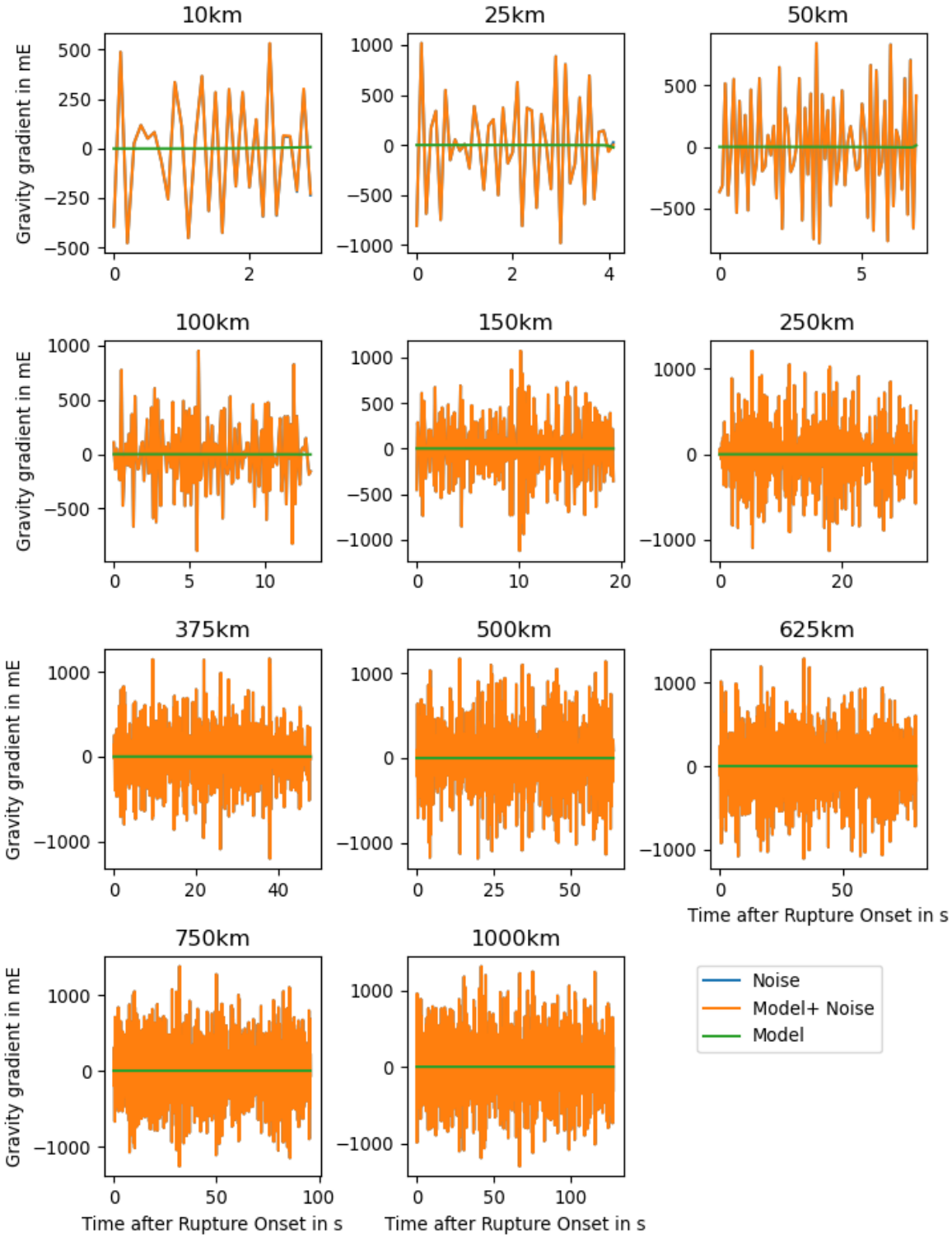

Figure 7.5: **Comparison between simulated gravity gradients and noise of the instrument of Griggs et al. (2017).** In blue the time series of simulated noise of the instrument of Griggs et al. (2017) are shown. However, as the difference is too small, they look the same as the time series of the noisy EE-components of gravity gradients of PEGS shown in orange. As a result the series of simulated noise can not be seen. The pure modelled EE-components of gravity gradients are shown in green. The signals shown here are for the Tohoku-Oki earthquake at stations in the westward direction perpendicular to the strike. The distances to the epicentre are given in the title of the subplots.

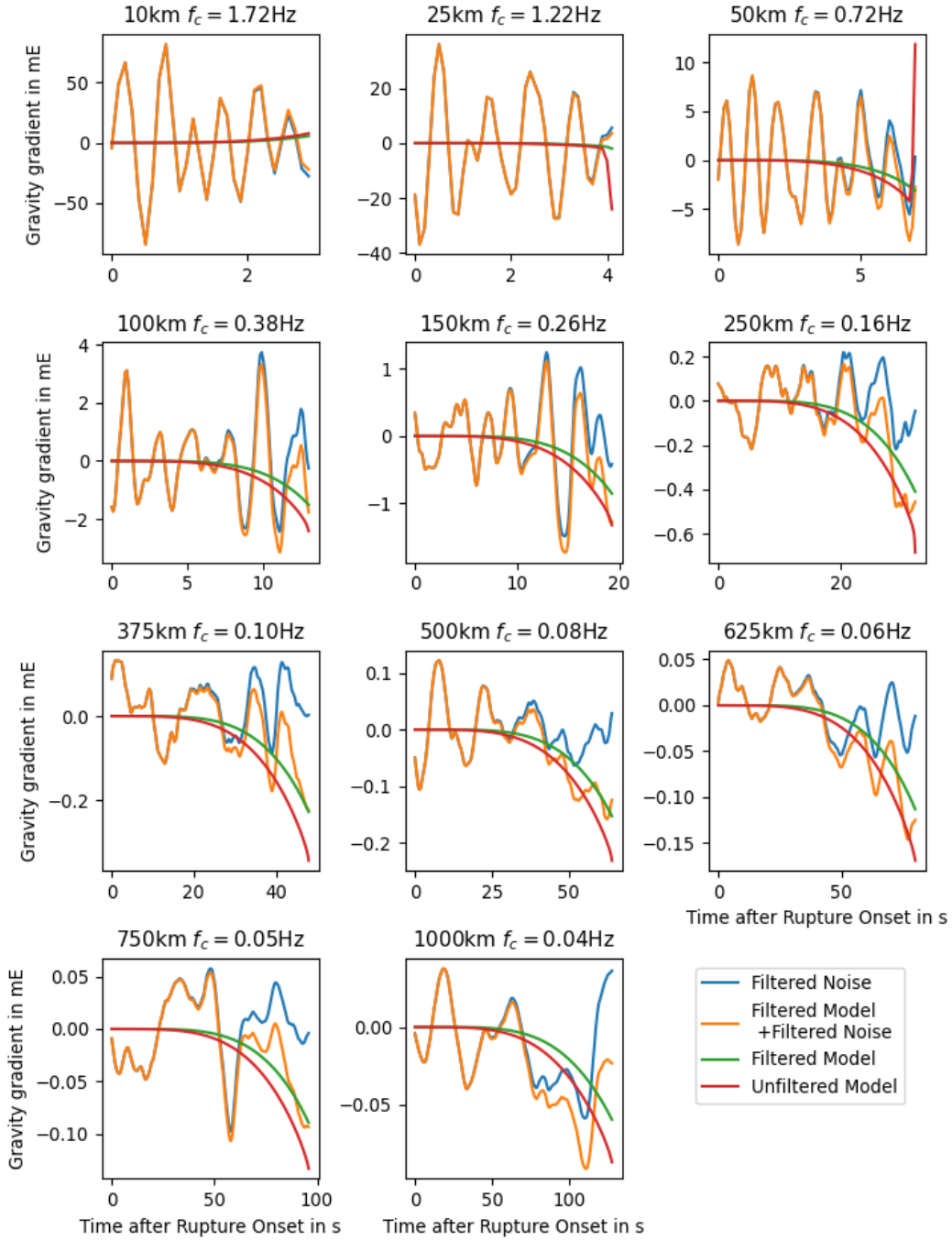

Figure 7.6: **Comparison between simulated gravity gradients and noise of the instrument of Griggs et al. (2017) after applying a lowpass filter.** The same signals as in Figure 7.5 are shown, but after applying a low-pass filter with the corner frequency f_c given in the title of the subplot. Additionally, the unfiltered model is shown in red.

without applying any filter the standard deviation of the noise is for all stations several orders of magnitude larger than the standard deviation of the signal and no difference between the time series of noise alone and the times series of signal with added noise can be seen. However, for most of the stations the main frequency of the noise is much higher than the main frequency of the signal. Therefore, the situation should improve by applying a low pass filter. As the timescale of the signals differ between the stations, the closer the station is to the epicentre the higher the corner frequency should be for not influencing the signal too much by the filtering. By testing different parameters I discover that a Butterworth filter of order 4 and a corner frequency of $\frac{5}{T}$ reduces the noise significantly without reducing the signal too much. Here, T is the length of the time series, that is the arrival time of the P-wave. With a finer tuning a better choice can probably be found, but for a first estimation of the detectability this filter should be sufficient. Also, it is not considered here that the application of the filter introduces a time shift of the signal. Probably, taking this into consideration and correcting this time shift, filters with lower corner frequency would still not have influenced the signal too much and filtered out more noise.

In Figure 7.6 the filtered model with and without the filtered additive noise can be seen for the same stations as before. Additionally, the filtered noise alone and the unfiltered model are shown. The last one is used to control that the filter does not affect the signal too much. In contrast to the unfiltered time series, a clear difference between the pure noise and the signal with added noise can be seen. Compared to the standard deviation of the remaining noise, this difference is the biggest between 250 km and 625 km away from the epicentre, but it never exceeds two times the standard deviation of the remaining noise.

Several methods for signal detection, e.g. the matched-filter technique, are based on the cross-correlation of the model and the measured signal. If the latter one is changing from a value close to zero to a value close to one, the model is expected to be present in the signal. Therefore, the cross-correlation between the model and the simulated signal (model with additive noise) can give a more objective impression of the detectability than just inspecting signal and model by eye. Therefore, for 50 different realisations of the noise at each station I calculate the cross-correlation coefficient between the filtered model and the model with additive noise. For comparison, I also calculate the cross-correlation coefficient between the filtered model and the pure filtered noise. The results are plotted as histograms in Figure 7.7. For a perfect detection of the signal the correlation coefficient between the model and the measured signal should be as close as possible to 1 and the cross-correlation between the pure noise and the model should in theory be 0, but at least

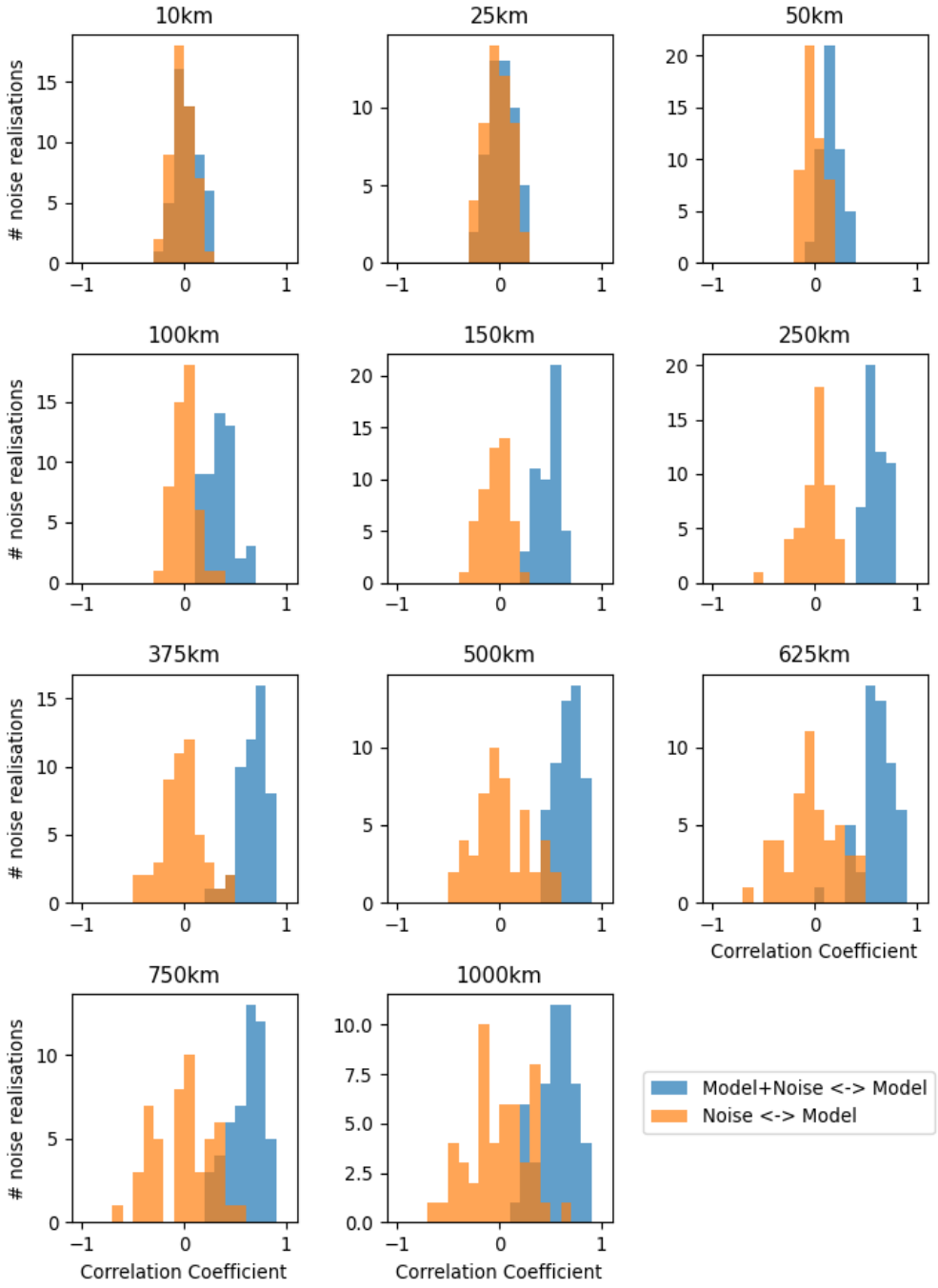

Figure 7.7: **Correlation coefficients between the model and the the simulated gradiometer output (model with additive noise) compared to correlation coefficients between the model and the pure noise.** The correlation coefficients are calculated for 50 different realisations of the noise at each station. Before calculating the correlation coefficient, low-pass filters with the corner frequencies given in Figure 7.6 are applied to all time series.

the cross-correlation coefficient should significantly change when the model is present in the data compared to when there is only noise measured. It can be seen that for stations more than 50 km away from the epicentre the mean of the correlation coefficient between the model and the model with additive noise is closer to 1 than the correlation coefficient between the model and the pure noise, but for most of the stations the distributions of correlation coefficient are not clearly separated. The only station for which they are not overlapping is the one 250 km away from the earthquake. However, also at this station the difference between the highest value of the correlation coefficient between the model and the pure noise is only about 0.15 smaller than the smallest correlation coefficient between the model and the simulated data. I assume when trying with different noise realisations the distributions can very likely overlap as well for the station 250 km away from the epicentre.

To sum things up, the correlation coefficients between the model with and without noise do not differ significantly from those between the model and the pure noise. That will make the detection of the gravity gradients of PEGS very difficult, but maybe it could be possible with very sophisticated methods, which consider several components of the gradient and several stations simultaneously. On the other hand, we should also keep in mind that here only the instruments self-noise was considered, but not seismic noise for example. Additionally, PEGS was assumed to be the only signal present in the measurements, while there could be other natural signals in the same frequency band as PEGS. These two things will complicate the detection of PEGS.

As mentioned before, I will analyse now if for the three closest stations a detection of the gravity gradients of PEGS could be possible with the instrument of Moody et al. (2002) as it has a lower noise level for signals shorter than 3 s. Figure 7.8 shows the modelled signal of the EE-component of the gradient with and without additive noise of the instrument of Moody et al. (2002). The pure noise of the instrument is shown for reference. In contrast to the instrument of Griggs et al. (2017), already before applying any filter a slight difference between the pure noise and the model with added noise can be seen. However, it is far to small for a detection of the signal. For the instrument of Moody et al. (2002), the noise spectrum shows high amplitudes for low frequencies. Thus, a low-pass filter will not help increasing the detectability, but a high-pass filter might help. On the other hand, it can be seen in Figure 7.8 that the noise still contains much of its amplitude at frequencies higher than the dominant frequency of the signal, which will not be filtered out with a high-pass filter. Therefore, I assume that also with the instrument of Moody et al. (2002) the gravity gradients are not detectable at stations up to 50 km away from the epicentre of the earthquake. For further stations anyway the

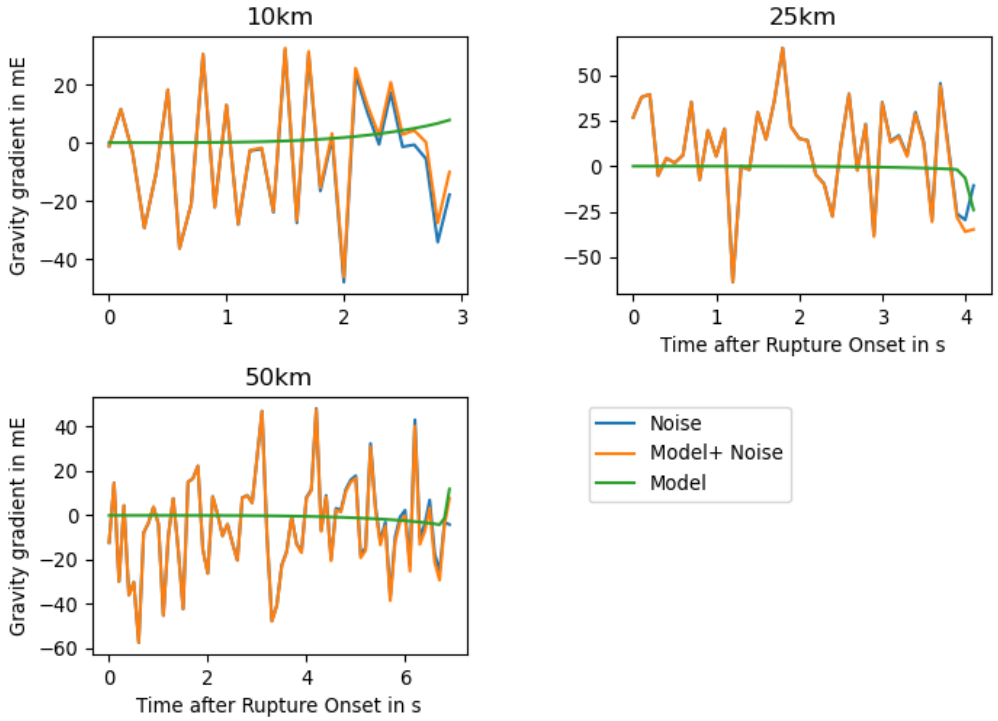

Figure 7.8: **Comparison between simulated gravity gradients and noise of the instrument of Moody et al. (2002).** In blue the time series of simulated noise of the instrument of Moody et al. (2002) are shown, in orange the modelled EE-component gravity gradients of PEGS added with noise. The pure modelled EE-components of gravity gradients are shown in green. The signals are shown for the Tohoku-Oki earthquake for stations in the westward direction perpendicular to the strike. The distances to the epicentre are given in the title of the subplots.

instrument of Griggs et al. (2017) is the more appropriate one.

The analysis for the gradiometers with the lowest noise level already showed it to be very challenging to detect PEGS with them. Therefore, I will now only shortly analyse the instruments with the higher noise level. For the GREMLIT instrument the modelled gravity gradients of PEGS are shown with and without additive noise in Figure 7.9 for the same stations as before. All the signals are filtered with the same low-pass Butterworth filters as for the instrument of Griggs et al. (2017) (order 4 and a corner frequency of $\frac{5}{T}$, with T being the P-wave travel time), as for both of these instruments high noise especially occurs for high frequencies. However, a band-pass filter could be a better choice for the GREMLIT instrument as the PSD is increasing for frequencies lower than 3 mHz. Figure 7.9 shows that after applying an appropriate low-pass filter the standard deviation of the noise is still about thousand times bigger than the signal. I expect the situation not to be much better when a band-pass filter is applied as the noise still shows much variation at the corner frequency of the low-pass filter. Therefore, the detection of PEGS will be impossible with the GREMLIT gradiometer. Since the noise level is even bigger for the dFTG and the FTGplus instrument of Lockheed Martin, also these instruments are not suitable to measure PEGS of an earthquake similar to the Tohoku-Oki earthquake.

7.4 Comparison between gravity gradient and gravity strain signals

Another question of this thesis is, whether there are disadvantages or advantages to detect PEGS with gravity gradiometers compared to gravity strainmeters. To analyse this question, I calculate the signals measured by gravity strainmeters for the stations in the east direction perpendicular to the strike used in Sections 7.1 and 7.3. Gravity strainmeters measure the double time integral of gravity gradients (See Formula 5.1). So, to calculate the strain signal I perform two numerical integrations of the gradient signal. The results for the EE- and the ZZ- component can be seen together with the gravity gradient signals in Figure 7.10. The EE- and the ZZ-component are chosen, because they were the biggest components of the gradient in this direction. It can be seen again, that the amplitudes of the gradients increase up to 25 km and decrease rapidly afterwards. The situation for gravity strains is completely different: They even decrease from 10 km to 25 km but they start to increase afterwards and they are still increasing at a distance of 1000 km. That means, that although the gravity gradient itself gets smaller its double time integral gets larger, as the time over which I integrate twice gets longer. In other words: A gravity

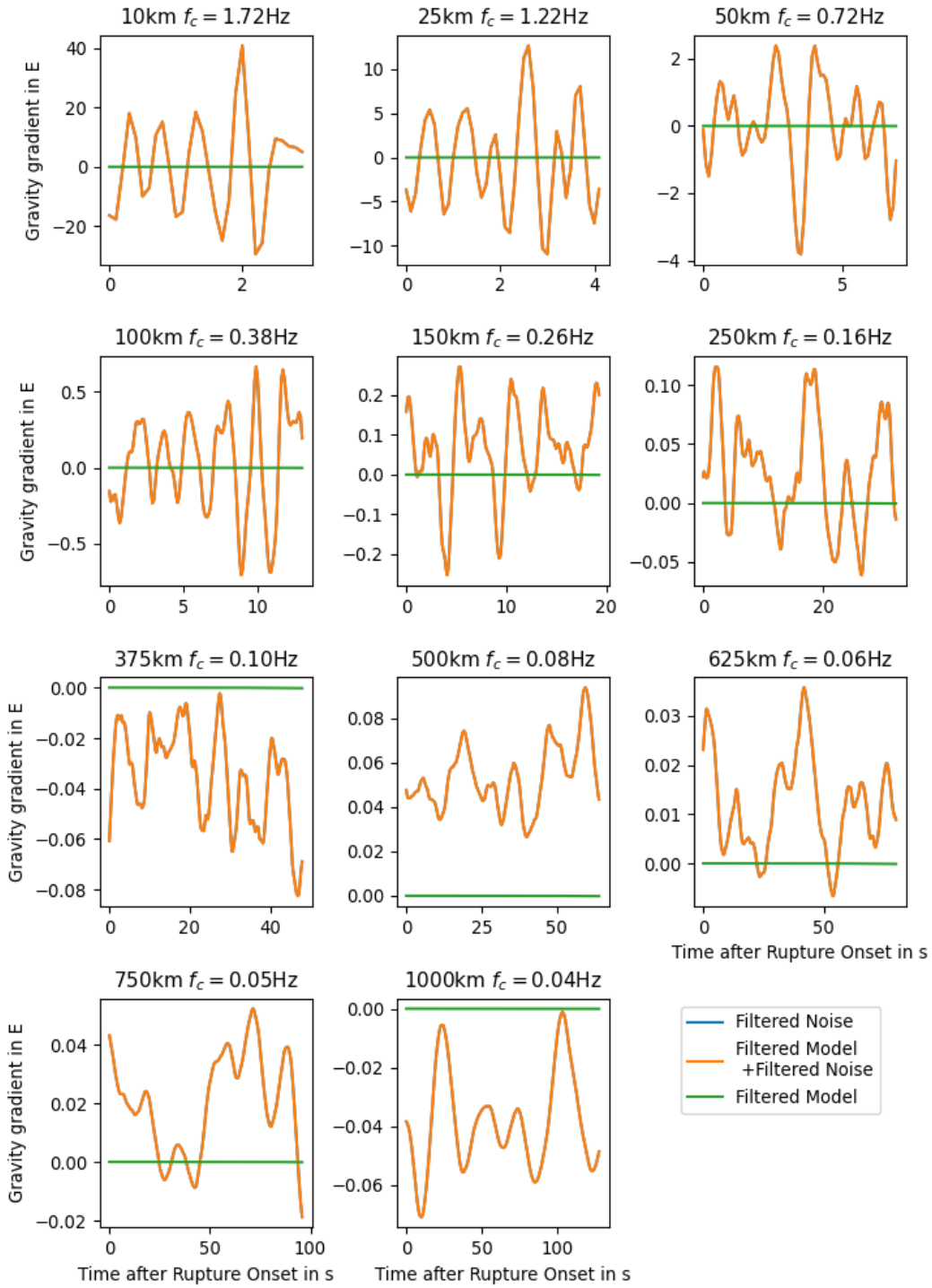

Figure 7.9: **Comparison between simulated gravity gradients and noise of the GREMLIT instrument after applying a low-pass filter.** In blue the time series of filtered simulated noise of the instrument of Griggs et al. (2017) are shown. They are completely overlapped by the time series of the filtered noisy EE-component gravity gradients of PEGS shown in orange. The pure filtered modelled EE-components of gravity gradients are shown in green. For all the signals a low-pass Butterworth filter of order 4 was used. The corner frequency f_c depends on the distance to the epicentre and is given in the subtitles of the plots. The signals shown here are for the Tohoku-Oki earthquake at stations in the westward direction perpendicular to the strike. The distances to the epicentre are given in the title of the subplots.

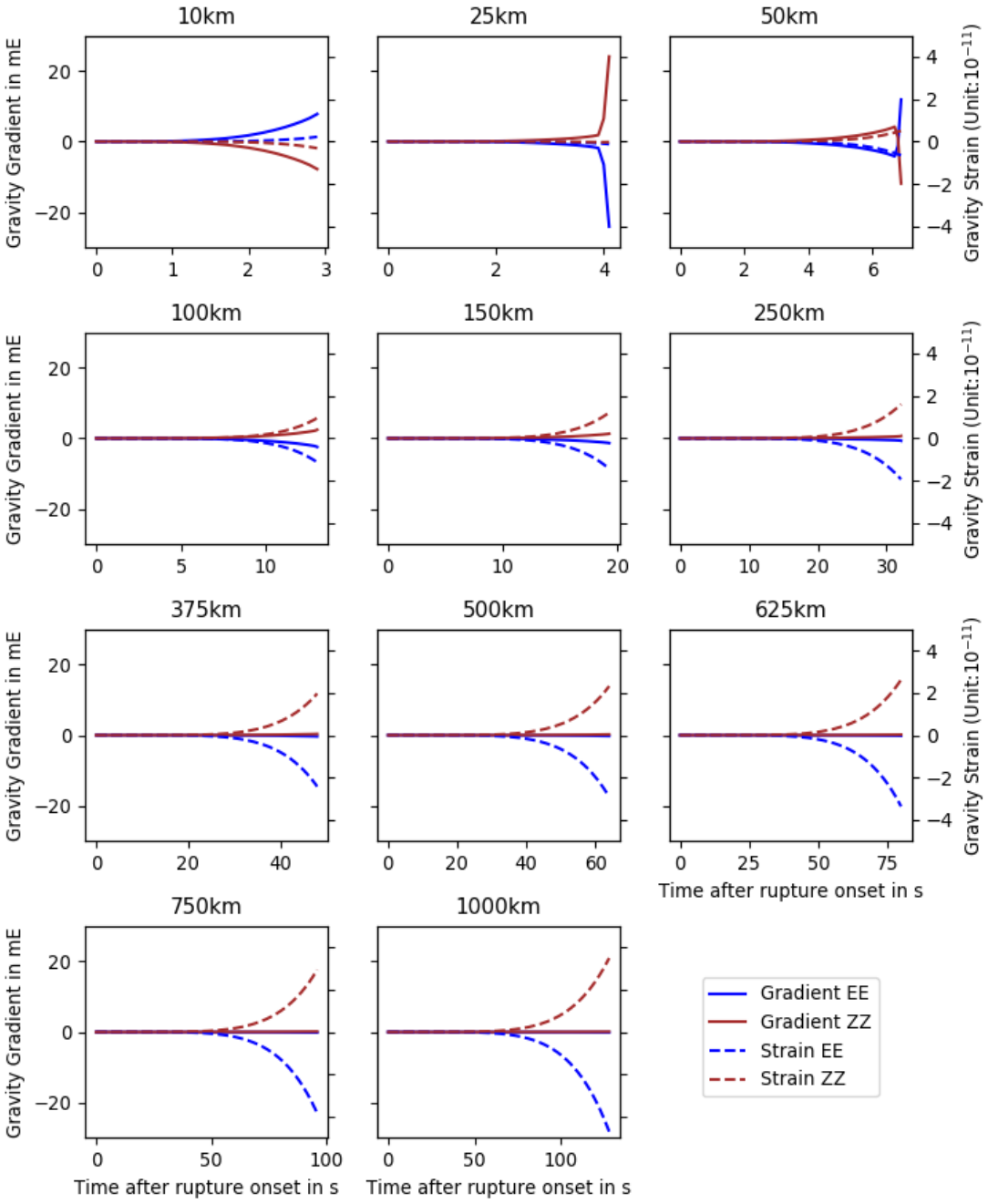

Figure 7.10: **Comparison between gravity gradient signals and strain signals of PEGS.** The figure shows two components of gravity gradients and gravity strains (EE- and ZZ-component) of PEGS induced by the Tohoku-Oki earthquake at stations in the westward direction perpendicular to the strike (direction of Station (c) in Figure 7.1). The stations are located at eleven different distances from the epicentre. All plots have the same gravity gradient- and gravity strain scale, but different time scales.

gradient in a gravity strainmeter produces a differential acceleration on the test masses. Although this acceleration gets smaller for larger distances, the final distance change between the test masses is bigger, because they were accelerated for a longer time. However, as the gravity gradient decays with $\frac{1}{r^3}$ in the far field and the time before the P-wave arrival increases only linearly with r, further away also the gravity strain will finally start to decrease with increasing distance.

I expect this could be an advantage of gravity strainmeters over gravity gradiometers: The gravity strainmeter signal is larger for larger distances where the signal also has a longer time scale and there would be more time to detect the signal. However, the detectability highly depends on the specific form of the noise spectrum of an instrument compared to the amplitude and frequency of the signal. A closer comparison of gravity strainmeters to gravity gradiometers would be needed in order to know if the maximum signal further away from the earthquake is really an advantage for detectability of PEGS with gravity strainmeters.

Anyway, there is a big advantage of gravity strainmeters compared to gravity gradiometers: following previous studies (Juhel et al. 2018a and Shimoda et al. 2020) there are gravity strainmeters under development in the context of gravitational wave detection which could detect PEGS of earthquakes down to a magnitude of $M_{\mathrm{W}} = 7.0$. Compared to this, all gravity gradiometers for which I could find some information, including those under development, would hardly be able to detect PEGS of an earthquake like the Tohoku-Oki earthquake, which had magnitude $M_{\mathrm{W}} = 9.1$.

Chapter 8

Conclusion and outlook

As a summary of this thesis the questions posed in Chapter 1 are answered and an outlook for further investigations is given:

1. **How can existing methods to model gravimeter, seismometer or gravity strainmeter measurements of PEGS be adapted to model gravity gradiometer measurements of PEGS?**

   In this thesis gravity gradients of PEGS were successfully modelled with the method of Harms (2016). This method solves the elastic equation of motion in a homogeneous half-space. From the solution with the help of the Poisson equation the change in gravity is calculated. Although the method is using a very simplified Earth model and ignores the coupling between the equation of motion and the Poisson equation, it is very convenient to estimate the order of magnitude of gravity gradients of PEGS. However, especially the assumption of homogeneity of the Earth is too much of a simplification, to obtain results accurate enough to compare to true measurements. I demonstrated this by showing that the size of the signal for gravity gradients of PEGS can change up to a factor of three when using different realistic values for P- and S-wave velocities.

   To overcome the limitations of the method of Harms (2016), I tested the use of normal mode summation to calculate gravity gradients of PEGS in a similar way as Juhel et al. (2018b) used it to calculate the vertical component of gravity change of PEGS. By this approach, a spherical, self gravitating Earth model with radial changing material and the coupling of the equation of motion and the Poisson equation is realised. I developed three very similar python programs for normal mode summations for vertical displacement, vertical gravity change and the change in all components of the gravity gradient tensor. They take normal mode catalogues calculated with the software package Mineos as input.

   The programs were tested for low frequencies ($\leq 8\,\mathrm{mHz}$) on the Tohoku Oki earthquake. The output of the python program for vertical displacement compares well to measured seismograms. Beside the missing high frequencies the output of the

python program for the vertical component of gravity change compared well to the simulations shown in Juhel et al. (2018b).

However, these tests showed some problems: The results for vertical displacement of the normal mode summation with python were inconsistent with those obtained with the normal mode summation of Mineos. Furthermore, using two different methods for the computation of the derivatives of the gravity potential at the Earth's surface, I obtained two different results. The main problem, which could not be solved, was to compute normal modes including gravity for frequencies higher than 50 mHz. For this reason I did not continue using this method.

The most recent published method for simulating PEGS measured with gravimeters or seismometers is the one proposed by Zhang et al. (2020). They use the same equations and a similar Earth model as the approach of normal mode summation, but they do not solve the eigenvalue problem but they solve the inhomogeneous equations directly. This is implemented in the QSSP code (Wang et al. 2017). In the end of the processing time of my thesis I got in contact with Rongjiang Wang, who provided me with the code of this method. Probably also gravity gradiometer or gravity strainmeter outputs can be simulated with it. I will try this in the future.

2. What do the signals of gravity gradients of PEGS look like?

Gravity gradients tensors of PEGS were simulated with the method of Harms (2016) for the Tohoku Oki earthquake. Most of the simulated signals are monotonically increasing or monotonically decreasing starting from zero. As a result, the largest amplitudes occur just before the P-wave arrival. The biggest amplitudes of about 40 mE are reached in the EZ-component about 25 km from the epicentre in the westward direction perpendicular to the strike. In general signals were bigger in the directions perpendicular to the strike than in all other directions. Furthermore, the maximum signal increases with distance from the epicentre up to a distance of 25 km. Afterwards a strong decrease with distance can be observed. 250 km away from the epicentre the maximum signal is already only 0.6 mE. That means the distance to the epicentre of the maximum signal of PEGS is much smaller for gravity gradients than for the vertical component of gravity. For the vertical component of gravity the maximum signals were obtained between 1000 km and 1500 km away from the epicentre in previous studies (Vallée et al. 2017). The form of the time evolution of the gravity gradients changes a lot up to a distance of 100 km, afterwards it is very stable, except for increasing signal length and decreasing amplitude.

3. **Should it be possible to detect those signals with gravity gradiometers that exist or are under development?**

   The most promising gradiometer to detect PEGS is the one Griggs et al. (2017) are currently developing. However, also with this one the detection of PEGS will be very difficult: Even for the Tohoku Oki earthquake, the fourth largest earthquake in the last 100 years worldwide, the standard deviation of the instrument's noise is still similar to the standard deviation of the signal after appropriate filtering. As the signals get longer with increasing distance from the epicentre, lower corner frequencies for the low-pass filter can be used. This leads to the fact that the signals at stations about 250 km away from the epicentre have the highest chance of detectability with the instrument of Griggs et al. (2017). However, I conclude from the standard deviation of the signal and the noise in Figure 7.6, that for a reliable detection of PEGS of earthquakes similar to the Tohoku Oki earthquake, instruments with at least ten times smaller noise levels would be needed. Maybe further developments in the techniques of gravity gradiometers such as quantum gradiometers will be able to reach these noise levels.

   All the other instruments studied in this thesis (eFTG, FTGplus, GREMLIT and the one of Moody et al. (2002)) were found not to be appropriate for the detection of PEGS, because of their noise level being too high.

4. **Are there advantages or disadvantages of gravity gradiometer signals compared to gravity strainmeter signals with regards to the detection of PEGS?**

   I found that the amplitude of the signals of gravity strain of PEGS increases up to a distance larger than 1000 km to the epicentre, whereas the signals of gravity gradients increase only up to 25 km and decrease quickly afterwards. This could be an advantage of gravity strainmeters.

   There is another more practical advantage of gravity strainmeters: Very accurate gravity strainmeters are planned to be developed for gravitational wave detection. As for gravitational wave detection even higher sensitivities are needed than for PEGS detection, prototypes of the gravitational wave detectors could be used for PEGS detection. Previous studies have shown that with these instruments PEGS of earthquakes down to magnitude $M_W = 7.0$ could be detected. This is much better than the results for gravity gradiometers inspected in this thesis, for which I found that even an earthquake of magnitude $M_W = 9.1$ is hardly detectable with gravity gradiometers under development.

Finally, I come to the conclusion that the gradiometers that have so far been developed and probably also gradiometers currently under development will not help to detect PEGS. For the moment I propose to study PEGS with signals measured by gravimeters or seismometers. In the future gravity strainmeters can eventually be used as well. Beside not being sensitive to ground motion they will have the advantage to carry more directional information compared to the vertical component of gravity. The methods of signal modulation of gravity gradients of PEGS studied in this thesis will also be useful to simulate signals measured with gravity strainmeters, as a gravity strain is the double time integral of a gravity gradient. With those simulations a lot of open questions could be addressed as for example:

1. Which component of the gravity strain shows the signals with the highest amplitude? This component does not need to be one in the local north oriented reference frame but it can be one in any rotated reference frame, depending probably on the direction of the strike. Answering this question could help to install gravity strainmeters in an optimal way, as in a specific region the strike of different earthquakes is often similar.

2. How can PEGS measured with gravity strainmeters be detected in real time?

3. How can measurements of gravity strainmeters contribute to earthquake early warning systems?

Appendix A

Associated Legendre functions

The associated Legendre functions are (Aki and Richards 1980):

$$P_l^m(x) = \frac{\sqrt{(1-x^2)^m}}{2^l l!} \frac{\partial^{l+m}}{\partial x^{l+m}} (x^2-1)^l \,,$$

for positive integers l and m, where $m \leq l$. The corresponding associated Legendre function for negative m are

$$P_l^{-m}(x) = (-1)^m \frac{(l-m)!}{(l+m)!} P_l^m(x) \,.$$

For the definition of the orthonormalised complex spherical harmonics (Equation 4.4) we need $\bar{P}_l^m(\cos\vartheta)$. $\bar{P}_l^m(x)$ are normalised versions of the associated Legendre functions such that

$$\int_{-1}^{1} (\bar{P}_l^m(x))^2 \mathrm{d}x = \frac{1}{2\pi} \,.$$

Additionally, the Condon-Shortly phase factor $(-1)^m$ is used. That leads to the following formula for $\bar{P}_l^m(x)$:

$$\begin{aligned} \bar{P}_l^m(x) &= (-1)^m \sqrt{\frac{2l+1}{4\pi} \frac{(l-m)!}{(l+m)!}} P_l^m(x) \\ \Rightarrow \bar{P}_l^{-m}(x) &= (-1)^m \bar{P}_l^m(x) \end{aligned}$$

Further, for the gravity gradient tensor we need the derivatives $\frac{\partial \bar{P}_l^m(\cos\vartheta)}{\partial\vartheta}$ and $\frac{\partial^2 \bar{P}_l^m(\cos\vartheta)}{\partial\vartheta^2}$ of the normalised associated Legendre functions. For the first derivative of the unnormalised associated Legendre functions Ilk (1983) gives

$$\frac{\partial P_l^m(\cos\vartheta)}{\partial\vartheta} = \frac{1}{2}\left((l+m)(l-m+1)P_l^{m-1}(\cos\vartheta) - P_l^{m+1}(\cos\vartheta)\right) \,,$$

where P_l^m should be set to zero for $m > l$.

From this formula a recursion formula for the second derivative can be derived:

$$\begin{aligned}\frac{\partial^2 P_l^m(\cos\vartheta)}{\partial\vartheta^2} =& \frac{1}{2}\left((l+m)(l-m+1)\frac{\partial P_l^{m-1}(\cos\vartheta)}{\partial\vartheta} - \frac{\partial P_l^{m+1}(\cos\vartheta)}{\partial\vartheta}\right)\\ =& \frac{1}{4}\Big((l+m)(l-m+1)(l+m-1)(l-m+2)P_l^{m-2}\\ &- (l+m)(l-m+1)P_l^m\\ &- (l+m+1)(l-m)P_l^m + P_l^{m+2}\Big)\,.\end{aligned}$$

For the normalised Legendre functions the scaling in the functions leads to a scaling in the derivatives:

$$\begin{aligned}\frac{\partial \bar{P}_l^m(\cos\vartheta)}{\partial\vartheta} &= (-1)^m\sqrt{\frac{2l+1}{4\pi}\frac{(l-m)!}{(l+m)!}}\frac{\partial P_l^m(\cos\vartheta)}{\partial\vartheta}\,,\\ \frac{\partial^2 \bar{P}_l^m(\cos\vartheta)}{\partial\vartheta^2} &= (-1)^m\sqrt{\frac{2l+1}{4\pi}\frac{(l-m)!}{(l+m)!}}\frac{\partial^2 P_l^m(\cos\vartheta)}{\partial\vartheta^2}\,.\end{aligned}$$

Appendix B

Laplace transformation

The definition used in this thesis for the Laplace transform $\mathfrak{L}\{f(t)\} = \bar{f}(s)$ of the function $f(t)$ is

$$\bar{f}(s) = \int_0^\infty f(t) \exp(-st) \mathrm{d}t \qquad \text{for } \mathrm{Re}\{s\} > 0\,.$$

if it exists (Aki and Richards 1980). Otherwise the Laplace transform keeps undefined.

Appendix C

Transformations of the coordinate system

C.1 From a geodetic to a geocentric coordinate system

The locations of epicentres and receivers are normally given as geodetic latitude and longitude. These coordinates must be transformed to geocentric colatitude and longitude. The difference between geodetic and geocentric latitude arises due to the flattening f of the Earth (see Figure C.1). Geocentric latitude $\theta_{\text{geoc.}}$ can be calculated from geodetic latitude $\theta_{\text{geod.}}$(Masters, lecture notes):

$$\tan\theta_{\text{geoc.}} = (1-f)^2 \tan\theta_{\text{geod.}}$$

From the geocentric latitude the geocentric colatitude ϑ can be calculated:

$$\vartheta = \frac{\pi}{2} - \theta_{\text{geoc.}}$$

The geocentric longitude φ is equal to the geodetic longitude.

C.2 From a geocentric to a epicentric coordinate system

As discussed in Section 6.2.1 the summation of normal modes simplifies if the earthquake occurs at colatitude $\vartheta'_{\text{EQ}} = 0$. Therefore, a new coordinate system is defined, where this is true. To completely define this coordinate system the actual geographic North pole is further imposed to be at $\varphi'_{\text{N}} = \pi$. In this section the coordinates of the receiver in this new coordinate system $(\vartheta'_{\text{R}}, \varphi'_{\text{R}})$ must be calculated. The coordinates of the earthquake EQ and the receiver R in geocentric coordinates are noted $(\vartheta_{\text{EQ}}, \varphi_{\text{EQ}})$ and $(\vartheta_{\text{R}}, \varphi_{\text{R}})$, as can be seen in Figure C.2. The imposed conditions for the new coordinate system can be

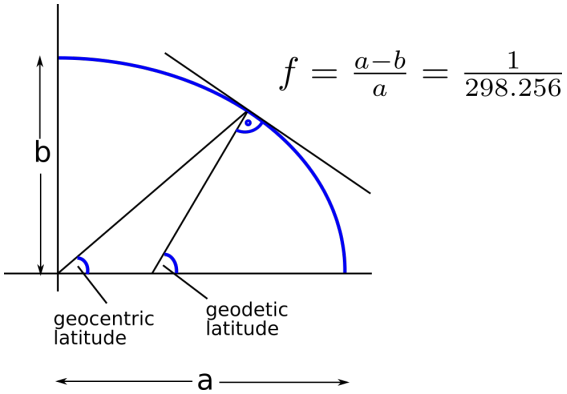

Figure C.1: **Difference between geodetic and geocentric colatitude.** The figure shows a quarter of the Earth as a ellipsoid of rotation with semi-axes a and b. The difference between geocentric and geodetic latitude is shown. Furthermore, the definition and the value of the Earth's flattening f are given. The sketch is adapted from Masters (lecture notes).

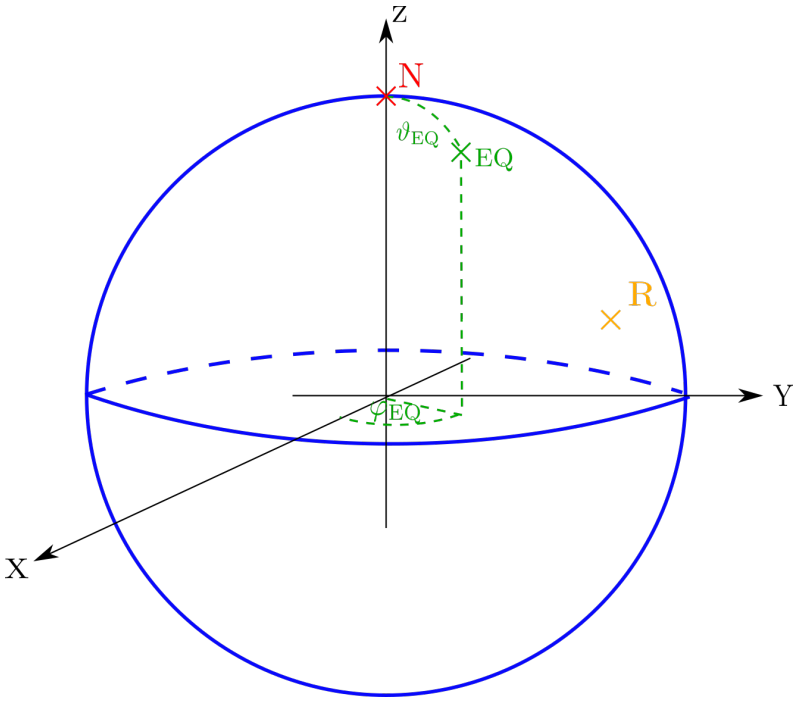

Figure C.2: **From geocentric to epicentric coordinates.** The sketch shows the geographic North pole (N), the epicentre of the earthquake (EQ) and the receiver (R) in geocentric coordinates. To change from a geocentric to an epicentric coordinate system, where the epicentre is at colatitude zero, the coordinate system first has to be rotated around the z-axis by φ_{EQ} and afterwards around the y-axis by ϑ_{EQ}.

achieved by the following transformations of the geocentric coordinate system:

1. $\varphi_{\mathrm{EQ}} \to 0 \quad \Rightarrow$ mathematical positive rotation of the coordinate system by φ_{EQ} around the z-axis:

$$R_1 = \begin{pmatrix} \cos\varphi_{\mathrm{EQ}} & \sin\varphi_{\mathrm{EQ}} & 0 \\ -\sin\varphi_{\mathrm{EQ}} & \cos\varphi_{\mathrm{EQ}} & 0 \\ 0 & 0 & 1 \end{pmatrix}$$

2. $\vartheta_{\mathrm{EQ}} \to 0 \quad \Rightarrow$ mathematical positive rotation of the coordinate system by ϑ_{EQ} around the y-axis:

$$R_2 = \begin{pmatrix} \cos\vartheta_{\mathrm{EQ}} & 0 & -\sin\vartheta_{\mathrm{EQ}} \\ 0 & 1 & 0 \\ \sin\vartheta_{\mathrm{EQ}} & 0 & \cos\vartheta_{\mathrm{EQ}} \end{pmatrix}$$

The coordinates of the receiver after the rotations are

$$\begin{aligned}
\boldsymbol{r}'_{\mathrm{R}} =& \boldsymbol{R}_2 \cdot \boldsymbol{R}_1 \cdot \boldsymbol{r}_{\mathrm{R}} \\
=& \begin{pmatrix} \cos\vartheta_{\mathrm{EQ}} & 0 & -\sin\vartheta_{\mathrm{EQ}} \\ 0 & 1 & 0 \\ \sin\vartheta_{\mathrm{EQ}} & 0 & \cos\vartheta_{\mathrm{EQ}} \end{pmatrix} \cdot \begin{pmatrix} \cos\varphi_{\mathrm{EQ}} & \sin\varphi_{\mathrm{EQ}} & 0 \\ -\sin\varphi_{\mathrm{EQ}} & \cos\varphi_{\mathrm{EQ}} & 0 \\ 0 & 0 & 1 \end{pmatrix} \cdot \begin{pmatrix} \cos\varphi_{\mathrm{R}} \sin\vartheta_{\mathrm{R}} \\ \sin\varphi_{\mathrm{R}} \sin\vartheta_{\mathrm{R}} \\ \cos\vartheta_{\mathrm{R}} \end{pmatrix} \\
=& \begin{pmatrix} \cos\vartheta_{\mathrm{EQ}} & 0 & -\sin\vartheta_{\mathrm{EQ}} \\ 0 & 1 & 0 \\ \sin\vartheta_{\mathrm{EQ}} & 0 & \cos\vartheta_{\mathrm{EQ}} \end{pmatrix} \cdot \begin{pmatrix} \sin\vartheta_{\mathrm{R}} \cos(\varphi_{\mathrm{R}} - \varphi_{\mathrm{EQ}}) \\ \sin\vartheta_{\mathrm{R}} \sin(\varphi_{\mathrm{R}} - \varphi_{\mathrm{EQ}}) \\ \cos\vartheta_{\mathrm{R}} \end{pmatrix} \\
=& \begin{pmatrix} \cos\vartheta_{\mathrm{EQ}} \sin\vartheta_{\mathrm{R}} \cos(\varphi_{\mathrm{R}} - \varphi_{\mathrm{EQ}}) - \sin\vartheta_{\mathrm{EQ}} \cos\vartheta_{\mathrm{R}} \\ \sin\vartheta_{\mathrm{R}} \sin(\varphi_{\mathrm{R}} - \varphi_{\mathrm{EQ}}) \\ \sin\vartheta_{\mathrm{EQ}} \sin\vartheta_{\mathrm{R}} \cos(\varphi_R - \varphi_{\mathrm{EQ}}) + \cos\vartheta_{\mathrm{R}} \cos\vartheta_{\mathrm{EQ}} \end{pmatrix} \\
\stackrel{!}{=}& \begin{pmatrix} \cos\varphi'_{\mathrm{R}} \sin\vartheta'_{\mathrm{R}} \\ \sin\varphi'_{\mathrm{R}} \sin\vartheta'_{\mathrm{R}} \\ \cos\vartheta'_{\mathrm{R}} \end{pmatrix} .
\end{aligned}$$

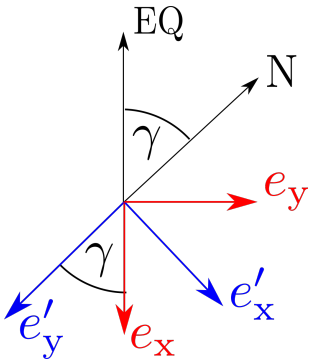

Figure C.3: **Rotation of the gravity gradient tensor.** In the epicentric coordinate system the x-axis of local Cartesian coordinates is pointing away from the epicentre of the earthquake (EQ). By a negative rotation by γ around the z-axis this local Cartesian coordinate system can be transformed to the local south oriented reference frame, where the x-axis is pointing to the South pole.

$$\Rightarrow \cos\vartheta'_{\mathrm{R}} = \sin\vartheta_{\mathrm{EQ}}\sin\vartheta_{\mathrm{R}}\cos(\varphi_R - \varphi_{\mathrm{EQ}}) + \cos\vartheta_r\cos\vartheta_{\mathrm{EQ}} \tag{C.1}$$

$$\sin\vartheta'_{\mathrm{R}} = \sqrt{1-\cos^2\vartheta'_{\mathrm{R}}} \tag{C.2}$$

$$\Rightarrow \sin\varphi'_{\mathrm{R}} = \frac{\sin\vartheta_{\mathrm{R}}\sin(\varphi_{\mathrm{R}} - \varphi_{\mathrm{EQ}})}{\sin\vartheta'_{\mathrm{R}}} \tag{C.3}$$

$$\begin{aligned}\cos\varphi'_{\mathrm{R}} &= \frac{\cos\vartheta_{\mathrm{EQ}}\sin\vartheta_{\mathrm{R}}\cos(\varphi_{\mathrm{R}} - \varphi_{\mathrm{EQ}}) - \sin\vartheta_{\mathrm{EQ}}\cos\vartheta_{\mathrm{R}}}{\sin\vartheta'_{\mathrm{R}}} \\ &= \frac{\cos\vartheta_{\mathrm{EQ}}\cos\vartheta'_{\mathrm{R}} - \cos\vartheta_{\mathrm{R}}}{\sin\vartheta_{\mathrm{EQ}}\sin\vartheta'_{\mathrm{R}}}\end{aligned} \tag{C.4}$$

These formulas are also given by Masters (lecture notes).

C.3 Rotation of the moment tensor to a local south oriented frame

The gravity gradient tensor $\boldsymbol{T}$ is calculated in a local Cartesian coordinate system. In the epicentric coordinate system used for the normal mode summation the x-axis of local Cartesian coordinates is pointing in the opposite direction of the earthquake, the z-axis is pointing upwards and the y-axis is completing the right-hand system. However, we will normally be interested in the gravity gradient tensor in a local south oriented reference frame, with the x-axis pointing towards the South pole, the z-axis again pointing upwards and the y-axis completing the right-hand system. Thus, the gravity gradient tensor has to be rotated around the z-axis by γ, where γ is the azimuth between the North pole and the earthquake observed at the measuring station (see Figure C.3). γ can also be seen as the difference between the longitude of the earthquake and the longitude of the North pole

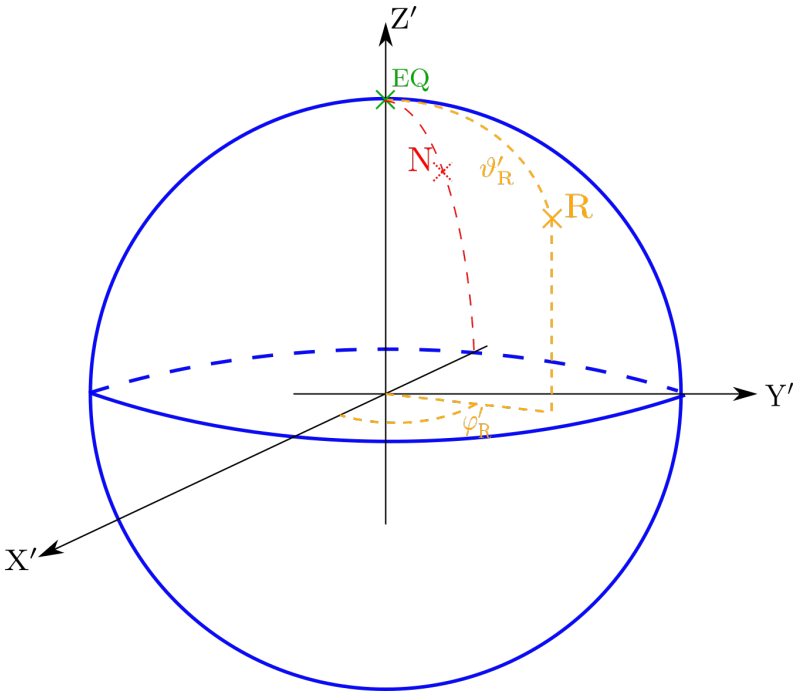

Figure C.4: **From epicentric to receiver-central coordinates.** The sketch shows the geographic North pole (N), the epicentre of the earthquake (EQ) and the receiver (R) in epicentric coordinates. To change from an epicentric to a receiver-central coordinate system, where the receiver is at colatitude zero, the coordinate system first has to be rotated around the z-axis by φ'_R and afterwards around the y-axis by ϑ'_R.

in a coordinate system with the receiver located at the positive z-axis (receiver-central coordinate system). A sketch of the coordinates of the epicentre of the earthquake, the geographic North pole and the receiver in epicentric coordinates is shown in Figure C.4. The transformation from epicentric coordinates to receiver-central coordinates can be achieved by the following transformations:

1. $\varphi'_R \to 0 \quad \Rightarrow$ mathematical positive rotation of the coordinate system by φ'_R around the z-axis:

$$R_3 = \begin{pmatrix} \cos\varphi'_R & \sin\varphi'_R & 0 \\ -\sin\varphi'_R & \cos\varphi'_R & 0 \\ 0 & 0 & 1 \end{pmatrix}$$

2. $\vartheta'_R \to 0 \quad \Rightarrow$ mathematical positive rotation of the coordinate system by ϑ'_R around the y-axis:

$$R_4 = \begin{pmatrix} \cos\vartheta'_R & 0 & -\sin\vartheta'_R \\ 0 & 1 & 0 \\ \sin\vartheta'_R & 0 & \cos\vartheta'_R \end{pmatrix}$$

The coordinates of the earthquake in receiver-central coordinates are

$$\boldsymbol{r}''_{\mathrm{EQ}} = \boldsymbol{R}_4 \cdot \boldsymbol{R}_3 \cdot \begin{pmatrix} 0 \\ 0 \\ 1 \end{pmatrix} = \begin{pmatrix} -\sin\vartheta'_{\mathrm{R}} \\ 0 \\ \cos\vartheta'_{\mathrm{R}} \end{pmatrix} \stackrel{!}{=} \begin{pmatrix} \cos\varphi''_{\mathrm{EQ}} \sin\vartheta''_{\mathrm{EQ}} \\ \sin\varphi''_{\mathrm{EQ}} \sin\vartheta''_{\mathrm{EQ}} \\ \cos\vartheta''_{\mathrm{EQ}} \end{pmatrix} .$$

$$\Rightarrow \vartheta''_{\mathrm{EQ}} = \vartheta'_{\mathrm{R}}$$

$$\Rightarrow \varphi''_{\mathrm{EQ}} = \pi$$

The coordinates of the North pole in receiver-central coordinates are

$$\begin{aligned}
\boldsymbol{r}''_{\mathrm{N}} =& \boldsymbol{R}_4 \cdot \boldsymbol{R}_3 \cdot \begin{pmatrix} -\sin\vartheta_{\mathrm{EQ}} \\ 0 \\ \cos\vartheta_{\mathrm{EQ}} \end{pmatrix} \\
=& \begin{pmatrix} \cos\vartheta'_{\mathrm{R}} & 0 & -\sin\vartheta'_{\mathrm{R}} \\ 0 & 1 & 0 \\ \sin\vartheta'_{\mathrm{R}} & 0 & \cos\vartheta'_{\mathrm{R}} \end{pmatrix} \cdot \begin{pmatrix} \cos\varphi'_{\mathrm{R}} & \sin\varphi'_{\mathrm{R}} & 0 \\ -\sin\varphi'_{\mathrm{R}} & \cos\varphi'_{\mathrm{R}} & 0 \\ 0 & 0 & 1 \end{pmatrix} \cdot \begin{pmatrix} -\sin\vartheta_{\mathrm{EQ}} \\ 0 \\ \cos\vartheta_{\mathrm{EQ}} \end{pmatrix} \\
=& \begin{pmatrix} \cos\vartheta'_{\mathrm{R}} & 0 & -\sin\vartheta'_{\mathrm{R}} \\ 0 & 1 & 0 \\ \sin\vartheta'_{\mathrm{R}} & 0 & \cos\vartheta'_{\mathrm{R}} \end{pmatrix} \cdot \begin{pmatrix} -\cos\varphi'_{\mathrm{R}} \sin\vartheta_{\mathrm{EQ}} \\ \sin\varphi'_{\mathrm{R}} \sin\vartheta_{\mathrm{EQ}} \\ \cos\vartheta_{\mathrm{EQ}} \end{pmatrix} \\
=& \begin{pmatrix} -\cos\vartheta'_{\mathrm{R}} \cos\varphi'_{\mathrm{R}} \sin\vartheta_{\mathrm{EQ}} - \sin\vartheta'_{\mathrm{R}} \cos\vartheta_{\mathrm{EQ}} \\ \sin\varphi'_{\mathrm{R}} \sin\vartheta_{\mathrm{EQ}} \\ -\sin\vartheta'_{\mathrm{R}} \cos\varphi'_{\mathrm{R}} \sin\vartheta_{\mathrm{EQ}} + \cos\vartheta'_{\mathrm{R}} \cos\vartheta_{\mathrm{EQ}} \end{pmatrix} .
\end{aligned}$$

And making use of C.3 and C.4,

$$\begin{aligned}
\boldsymbol{r}''_{\mathrm{N}} &= \begin{pmatrix} -\frac{\cos\vartheta'_{\mathrm{R}}(\cos\vartheta_{\mathrm{EQ}} \cos\vartheta'_{\mathrm{R}} - \cos\vartheta_{\mathrm{R}})}{\sin\vartheta'_{\mathrm{R}}} - \sin\vartheta'_{\mathrm{R}} \cos\vartheta_{\mathrm{EQ}} \\ \frac{\sin\vartheta_{\mathrm{EQ}} \sin\vartheta_{\mathrm{R}} \sin(\varphi_{\mathrm{R}} - \varphi_{\mathrm{EQ}})}{\sin\vartheta'_{\mathrm{R}}} \\ -\cos\vartheta_{\mathrm{EQ}} \cos\vartheta'_{\mathrm{R}} + \cos\vartheta_{\mathrm{R}} + \cos\vartheta_{\mathrm{EQ}} \cos\vartheta'_{\mathrm{R}} \end{pmatrix} \\
&= \begin{pmatrix} \frac{-\cos\vartheta_{\mathrm{EQ}} + \cos\vartheta'_{\mathrm{R}} \cos\vartheta_{\mathrm{R}}}{\sin\vartheta'_{\mathrm{R}}} \\ \frac{\sin\vartheta_{\mathrm{EQ}} \sin\vartheta_{\mathrm{R}} \sin(\varphi_{\mathrm{R}} - \varphi_{\mathrm{EQ}})}{\sin\vartheta'_{\mathrm{R}}} \\ \cos\vartheta_{\mathrm{R}} \end{pmatrix} \stackrel{!}{=} \begin{pmatrix} \cos\varphi''_{\mathrm{N}} \sin\vartheta''_{\mathrm{N}} \\ \sin\varphi''_{\mathrm{N}} \sin\vartheta''_{\mathrm{N}} \\ \cos\vartheta''_{\mathrm{N}} \end{pmatrix} .
\end{aligned}$$

$$\Rightarrow \vartheta''_{\mathrm{N}} = \vartheta_{\mathrm{R}}$$

$$\Rightarrow \cos\varphi''_{\mathrm{N}} = \frac{-\cos\vartheta_{\mathrm{EQ}} + \cos\vartheta'_{\mathrm{R}}\cos\vartheta_{\mathrm{R}}}{\sin\vartheta'_{\mathrm{R}}\sin\vartheta_{\mathrm{R}}} \qquad \sin\varphi''_{\mathrm{N}} = \frac{\sin\vartheta_{\mathrm{EQ}}\sin(\varphi_{\mathrm{R}} - \varphi_{\mathrm{EQ}})}{\sin\vartheta'_{\mathrm{R}}}$$

$$\gamma = \varphi''_{\mathrm{EQ}} - \varphi''_{\mathrm{N}} = \pi - \varphi''_{\mathrm{N}}$$

$$\Rightarrow \cos\gamma = \frac{\cos\vartheta_{\mathrm{EQ}} - \cos\vartheta'_{\mathrm{R}}\cos\vartheta_{\mathrm{R}}}{\sin\vartheta'_{\mathrm{R}}\sin\vartheta_{\mathrm{R}}} \qquad \sin\gamma = \frac{\sin\vartheta_{\mathrm{EQ}}\sin(\varphi_{\mathrm{R}} - \varphi_{\mathrm{EQ}})}{\sin\vartheta'_{\mathrm{R}}}$$

Again, these formulas can also be found in Masters (lecture notes).

Finally, as can be seen in Figure C.3, the rotation we need for the gravity gradient tensor is a negative rotation of the coordinate system by γ around the z-axis:

$$\boldsymbol{T'} = \begin{pmatrix} \cos\gamma & -\sin\gamma & 0 \\ \sin\gamma & \cos\gamma & 0 \\ 0 & 0 & 1 \end{pmatrix} \cdot \boldsymbol{T} \cdot \begin{pmatrix} \cos\gamma & \sin\gamma & 0 \\ -\sin\gamma & \cos\gamma & 0 \\ 0 & 0 & 1 \end{pmatrix} .$$

Appendix D

Distance dependency of gravity gradients of PEGS for other directions

In Section 7.1 the dependency of gradients of PEGS of the Tohoku-Oki earthquake on the distance was only shown for stations in the westward direction perpendicular to the strike. To complete the overview of time series of gravity gradients of PEGS for the Tohoku-Oki earthquake the dependence on the distance is shown for four more directions in Figure D.1, D.2, D.3 and D.4.

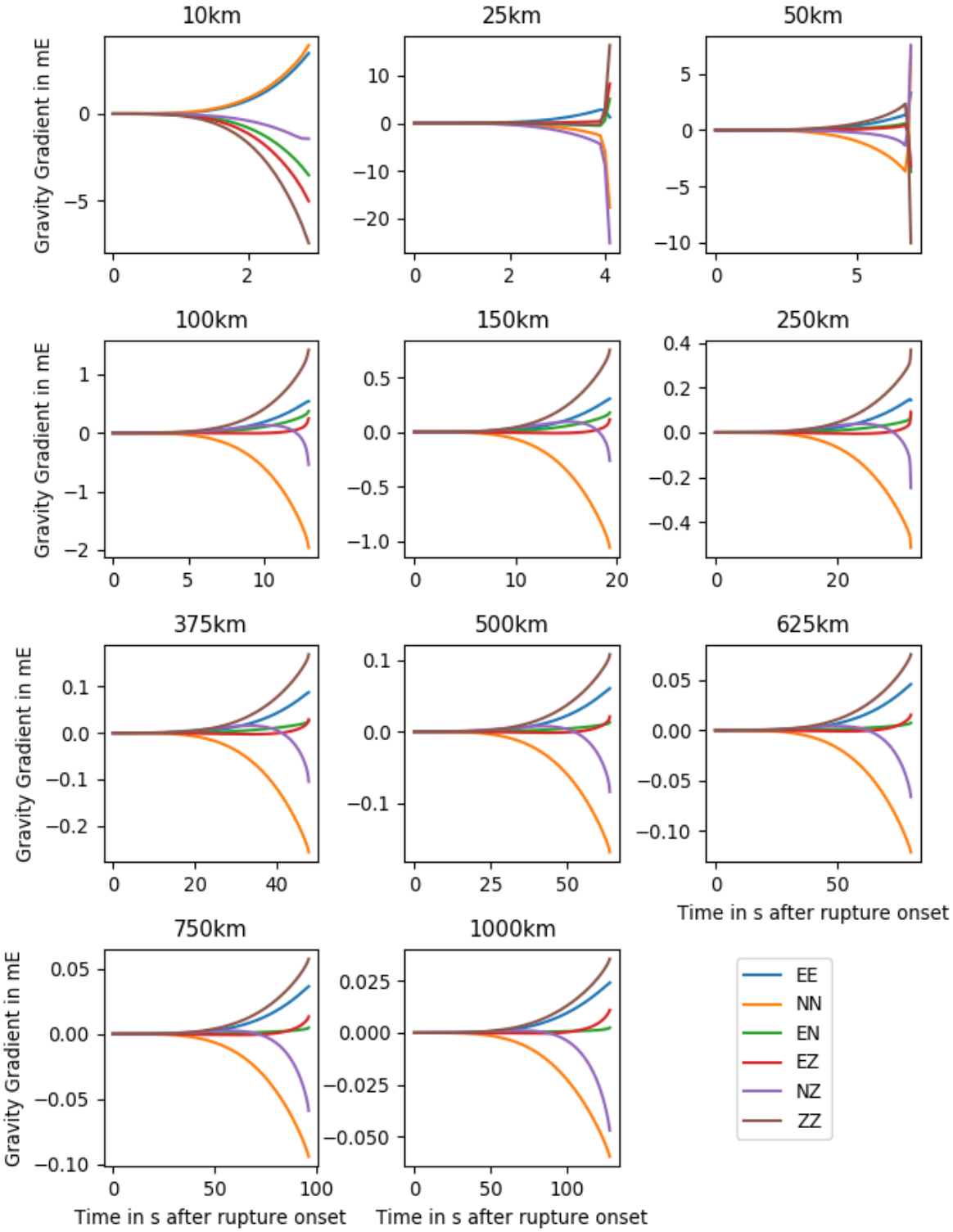

Figure D.1: **Distance dependency of gravity gradients of PEGS in a direction of 45° away from the strike.** The figure shows gravity gradients of PEGS induced by the Tohoku-Oki earthquake at stations in the north west direction 45° away from the strike (direction of station (a) in Figure 7.1). The stations are located at 11 different distances from the epicentre, which are given in the titles of the subplots.

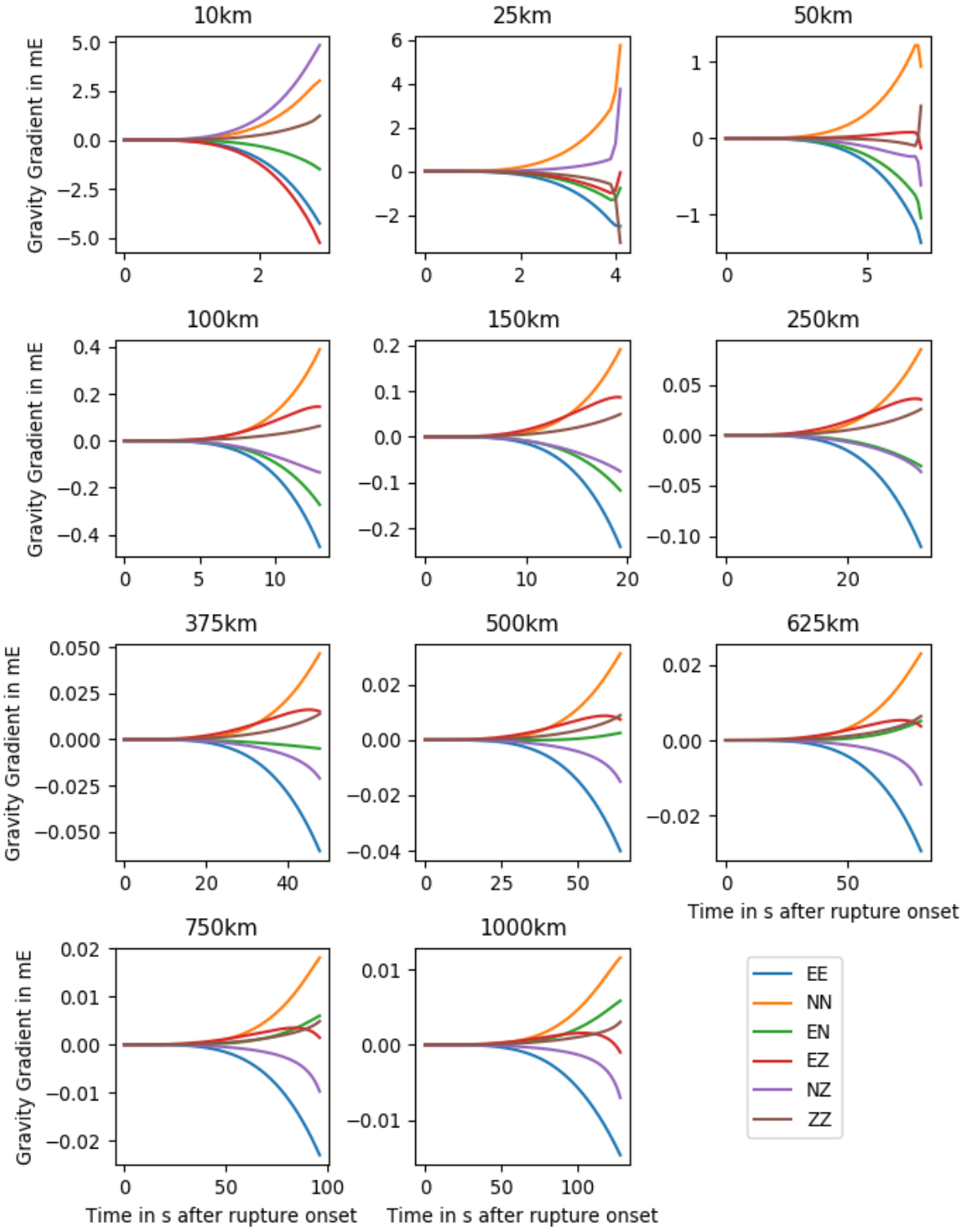

Figure D.2: **Distance dependency of gravity gradients of PEGS in the north direction of the strike.** The figure shows gravity gradients of PEGS induced by the Tohoku-Oki earthquake at stations in the northward direction of the strike (direction of station (b) in Figure 7.1). The stations are located at 11 different distances from the epicentre, which are given in the titles of the subplots.

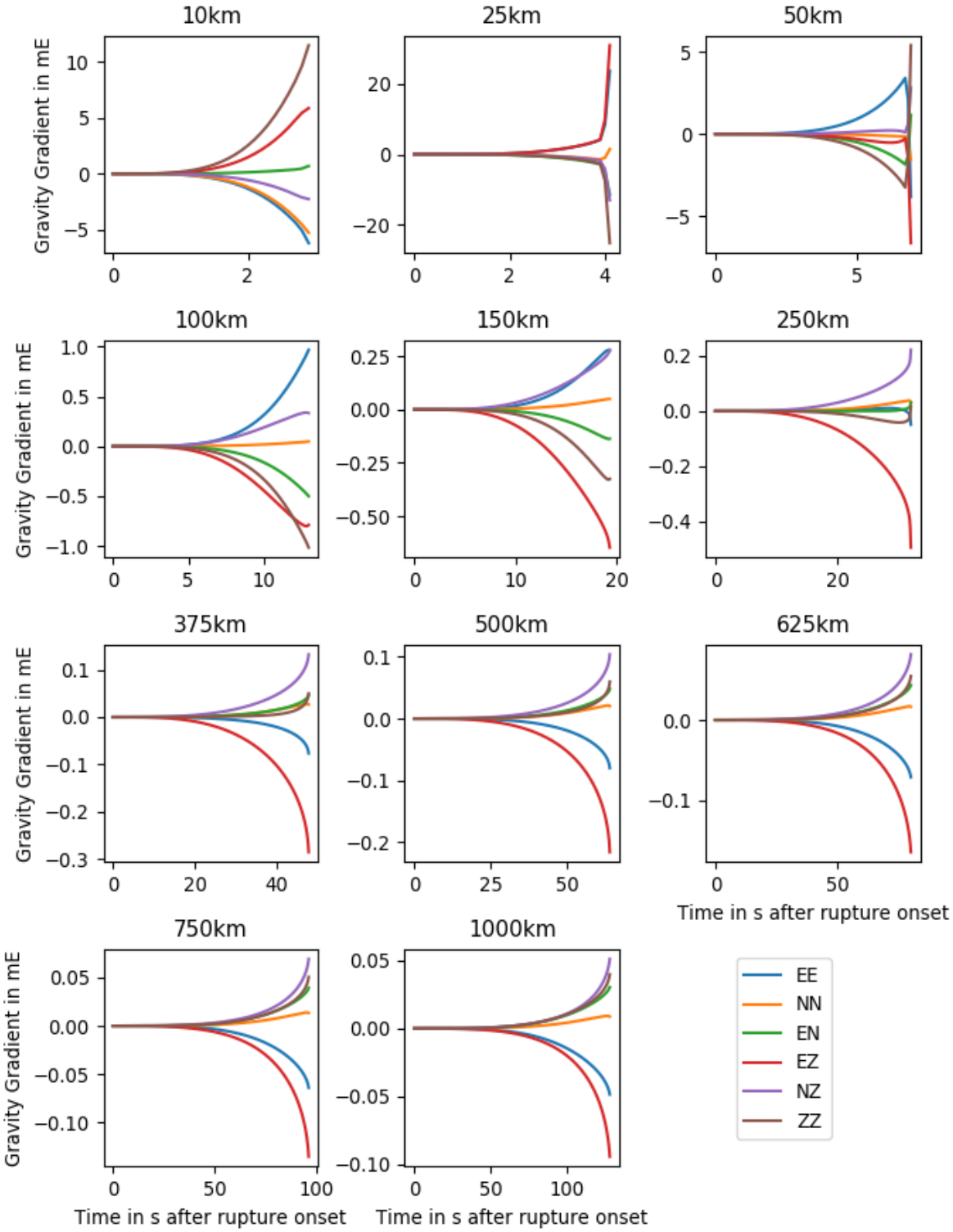

Figure D.3: **Distance dependency of gravity gradients of PEGS in the east direction perpendicular to the strike.** The figure shows gravity gradients of PEGS induced by the Tohoku-Oki earthquake at stations in the eastward direction perpendicular to the strike (direction of station (d) in Figure 7.1). The stations are located at 11 different distances from the epicentre, which are given in the titles of the subplots.

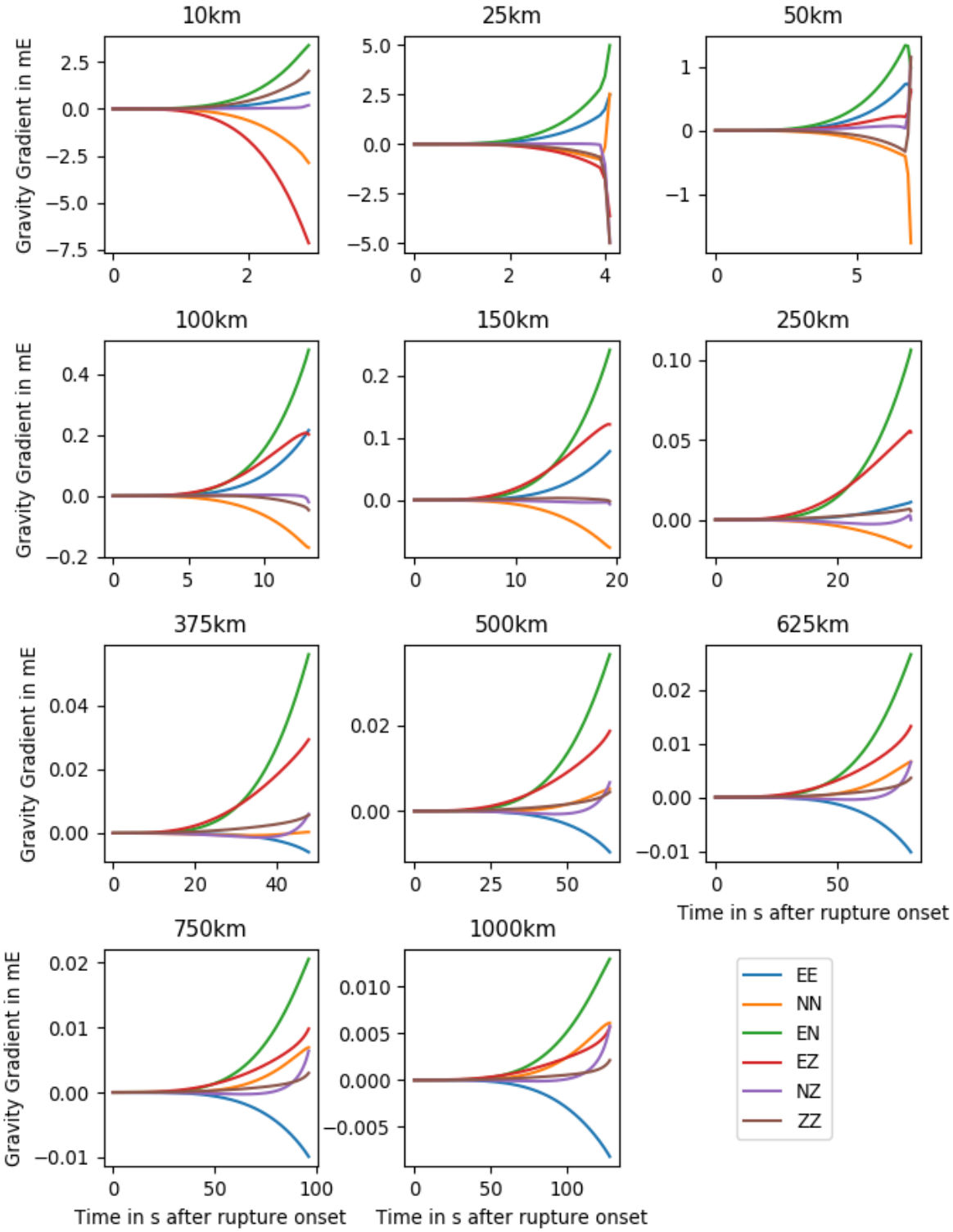

Figure D.4: **Distance dependency of gravity gradients of PEGS in the south direction of the strike.** The figure shows gravity gradients of PEGS induced by the Tohoku-Oki earthquake at stations in the southward direction of the strike (direction of station (c) in Figure 7.1). The stations are located at 11 different distances from the epicentre, which are given in the titles of the subplots.

Appendix E

Python code for normal mode summation

E.1 Main programs

E.1.1 Normal mode summation for vertical displacement

```
import CoeffMomentStrain as coeff
import EigenReceiver as eigen
import ReadInput as read
import Time as time
import Units as un
import geometry as geo
import interpol as ip

import numpy as np
import matplotlib.pyplot as plt

###Input parameters
#Folder with output files of eigcon (part of the Mineos program) giving all
#information about eigenfunctions
folderEigen='./TestMineos/RelParaDisp/Anoocean_R_S'
#Folder with moment tensor file of the earthquake
folderQuake='.</EarthquakeDatabase/Tohoku'
T=360*60-1 #length of the times series to be computed
deltat=1 #sampling interval
#Latitude and Longitude of the receiver
#latR,lonR=[48.3319,8.3311]#BFO
#latR,lonR=[ -32.3797,20.8117]#SUR
latR,lonR=[-11.9875,-76.8422]#NNA
```

```
###Setup time vector and change to Mineos unit system
t=time.time(T,deltat)
tmineos=un.s2mineos(t)
deltatmineos=un.s2mineos(deltat)

###Read the input
#Attention: The eigenfuction of the potential is called P in this code
#it was called phi in the thesis
n,l,omega,q,r,U,dUdr,V,dVdr,P,dPdr=read.ReadEigenMode(folderEigen)
M,rs,latS,longS,dmdtmineos,tdmdtSI=read.ReadEarthquake(folderQuake,deltat)

#Calculate epicentric coordinates of the receiver
Delta,Phi=geo.changeangles(latR,lonR,latS,longS)

###Normal mode summation of the Greens function for vertical displacement
green=np.zeros(t.size)
for i,li in enumerate(l):
    lint=int(li)
    U_rs,dUdr_rs=ip.eigenfuncatsource(r,U[i],dUdr[i],rs)
    V_rs,dVdr_rs=ip.eigenfuncatsource(r,V[i],dVdr[i],rs)
    U_rr=U[i][-1]
    maxm=int(min(li,2))
    summem=0
    for m in range(-maxm,maxm+1):
        Coeff=coeff.MultMomentStrain(lint,m,rs,U_rs,dUdr_rs,V_rs,dVdr_rs,M)
        Gamma=eigen.VertDispEigen(lint,m,U_rr,Delta,Phi)
        summem+=Gamma*Coeff
    timeseries=time.TimeSeries(omega[i],q[i],tmineos)
    summand=summem*timeseries
    green=green+summand

green=green.real

###Time convolution with source time function and conversion back to SI units
mess=time.convol(dmdtmineos,green,deltatmineos)
messSI=un.mineos2m(mess)
tmess=time.time(t[-1]+len(tdmdtSI)-1,deltat,t0=tdmdtSI[0])

###Save the result
np.savetxt('MessTohokuNNAMastersSH.txt', np.vstack((tmess,messSI)).T)
```

E.1.2 Normal mode summation for vertical component of gravity

```
import CoeffMomentStrain as coeff
import EigenReceiver as eigen
import ReadInput as read
import Time as time
import Units as un
import geometry as geo
import interpol as ip

import numpy as np
import matplotlib.pyplot as plt
import scipy.signal as sig

###Input parameters
#Folder with output files of eigcon (part of the Mineos programm) giving all
#information about eigenfunctions
folderEigen='./TestMineos/RelParaDisp/Anoocean_R_S'
#Folder with momenttensor file of the earthquake
folderQuake='./EarthquakeDatabase/Tohoku'
T=360*60-1  #length of the times series to be computed
deltat=1 #sampling interval
#Latitude and Longitude of the receiver
latR,lonR=[44.62,129.59] #MDJ

###Setup time vector and change to Mineos unit system
t=time.time(T,deltat)
tmineos=un.s2mineos(t)
deltatmineos=un.s2mineos(deltat)



###Read the input
n,l,omega,q,r,U,dUdr,V,dVdr,P,dPhdr=read.ReadEigenMode(folderEigen)
M,rs,latS,longS,dmdtmineos,tdmdtSI=read.ReadEarthquake(folderQuake,deltat)

#Calculate epicentric coordinates of the receiver
Delta,Phi=geo.changeangles(latR,lonR,latS,longS)
```

```
###Normal mode summation of the Greens function for vertical gravity
green=np.zeros(t.size)
for i,li in enumerate(l):
    lint=int(li)
    U_rs,dUdr_rs=ip.eigenfuncatsource(r,U[i],dUdr[i],rs)
    V_rs,dVdr_rs=ip.eigenfuncatsource(r,V[i],dVdr[i],rs)
    dPdr_rr=dPdr[i][-1]
    P_rr=P[i][-1]
    maxm=int(min(li,2))
    summem=0
    for m in range(-maxm,maxm+1):
        Coeff=coeff.MultMomentStrain(lint,m,rs,U_rs,dUdr_rs,V_rs,dVdr_rs,M)
        Gamma=eigen.VertGravEigen2(lint,m,dPdr_rr,Delta,Phi)
        summem+=Coeff*Gamma
    timeseries=time.TimeSeries(omega[i],q[i],tmineos)
    summand=summem*timeseries
    green=green+summand

green=green.real


###Time convolution with source time function and conversion back to SI units
mess=time.convol(dmdtmineos,green,deltatmineos)
messSI=un.mineos2mpersqrs(mess)
tmess=time.time(t[-1]+len(tdmdtSI)-1,deltat,t0=tdmdtSI[0])

###Save the results
np.savetxt('Tohoku_MDJ_Gravity1.txt', np.vstack((tmess,messSI)).T)
```

E.1.3 Normal mode summation for all components of the gravity gradient tensor

```
import CoeffMomentStrain as coeff
import EigenReceiver as eigen
import ReadInput as read
import Time as time
import Units as un
import geometry as geo
import interpol as ip

import numpy as np
import matplotlib.pyplot as plt
import scipy.signal as sig

###Input parameters
#Folder with output files of eigcon (part of the Mineos programm) giving all
#information about eigenfunctions
folderEigen='/home/geodaesie/Clara/Master/TestMineos/RelParaDisp/Anoocean_R_S'
#Folder with moment tensor file of the earthquake
folderQuake='/home/geodaesie/Clara/Master/EarthquakeDatabase/Tohoku'
T=360*60-1  #length of the times series to be computed
deltat=1 #sampling interval
#Latitude and Longitude of the receiver
latR,lonR=[44.62,129.59]#MDJ

###Setup time vector and change to Mineos unit system
t=time.time(T,deltat)
tmineos=un.s2mineos(t) #in s
deltatmineos=un.s2mineos(deltat)

###Read the input
n,l,omega,q,r,U,dUdr,V,dVdr,P,dPdr=read.ReadEigenMode(folderEigen)
M,rs,latS,longS,dmdtmineos,tdmdtSI=read.ReadEarthquake(folderQuake,deltat)

###Calculate epicentric coordinates of the receiver
Delta,Phi,gamma=geo.changeangles(latR,lonR,latS,longS,ReturnGamma=True)
```

```
###Compute Legendre function and its first and second derivative at the
#receiver coordinates
lmax=int(max(l))
Plm_Matrix,Plm_dtheta_Matrix,Plm_d2theta_Matrix=eigen.initializePlm(lmax,2,Delta)

###Normal mode summation of the Greens function for gradient tensor
green=np.zeros((6,t.size),dtype=complex)
for i,li in enumerate(l):
    lint=int(li)
    U_rs,dUdr_rs=ip.eigenfuncatsource(r,U[i],dUdr[i],rs)
    V_rs,dVdr_rs=ip.eigenfuncatsource(r,V[i],dVdr[i],rs)
    dPdr_rr=dPdr[i][-1]
    P_rr=P[i][-1]
    maxm=int(min(li,2))
    summem=0
    for m in range(-maxm,maxm+1):
        Coeff=coeff.MultMomentStrain(lint,m,rs,U_rs,dUdr_rs,V_rs,dVdr_rs,M)

        Plm,Plm_dtheta,Plm_d2theta=eigen.evaluatePlm(Plm_Matrix[abs(m),lint],
                                                     Plm_dtheta_Matrix[abs(m),
                                                                       lint],
                                                     Plm_d2theta_Matrix[abs(m),
                                                                        lint],
                                                     lint,m)
        Gamma=eigen.GradientTensor(lint,m,P_rr,Delta,Phi,Plm_dtheta,Plm_d2theta)
        summem+=Coeff*np.array(Gamma)
    summem=np.array(geo.RotateGravTensor(summem[0],summem[1],summem[2],
                                         summem[3],summem[4],summem[5],gamma))
    timeseries=time.TimeSeries(omega[i],q[i],tmineos)
    for k in range(6):
        summand=summem[k]*timeseries
        green[k,:]=green[k,:]+summand
green=green.real

###Time convolution with source time function and conversion back to SI units
mess=np.zeros((6,t.size+len(tdmdtSI)-1))
for k in range(6):
    mess[k,:]=time.convol(dmdtmineos,green[k,:],deltatmineos)
messSI=un.mineos2sqrHz(mess)
tmess=time.time(t[-1]+len(tdmdtSI)-1,deltat,t0=tdmdtSI[0])
###Save the results
np.savetxt('MessGradientTohokuMDJMastersSH.txt', np.vstack((tmess,messSI)).T)
```

E.2 Modules needed for the main programms

E.2.1 Read Input (ReadInput)

```
import numpy as np
import Units as un
import os
import Time as time

#Read the latitude, longitude, CMT moment tensor, the depth and the half duration
#of the earthquake given in the file file. Depth is converted to radius and
#radius and moment tensor are converted to the Mineos unit system
def readmomenttensor(file):
    lon,lat,depth,mrr,mtt,mpp,mrt,mrp,mtp,exp,Thalf=np.loadtxt(file, unpack=True)
    M=np.array([mrr,mtt,mpp,mrt,mrp,mtp])
    expNm=exp-7
    M=un.Nm2mineos(M*10**(expNm))
    rs=un.rn-depth*1000
    rs=un.m2mineos(rs)
    return(M,rs,lat,lon,Thalf)
#Compute a Triangle Source time function for a given half duration and convert
#it to Mineos unit system
def Triangle(Thalf,dt):
    tdmdt=time.time(2*Thalf,dt)-Thalf
    dmdt=np.append(1/Thalf+1/Thalf**2*tdmdt[np.nonzero(tdmdt<0)],
                   1/Thalf-1/Thalf**2*tdmdt[np.nonzero(tdmdt>=0)])
    dmdttmineos=un.mHz2mineos(1000*dmdt)
    return(dmdttmineos,tdmdt)
#Read the information about the earthquake given in the folder folderQuake
def ReadEarthquake(folderQuake,dt):
    fileMoment=folderQuake+'/Moment.txt'
    M,rs,lat,lon,Thalf=readmomenttensor(fileMoment)
    dmdt,tdmdt=Triangle(Thalf,dt)
    return( M,rs,lat,lon,dmdt,tdmdt)

#Read degree, order, eigenfrequency, damping coefficient and the values of the
#eigenfuctions nUl, nVl, nPl and its derivatives given at discreet radius r from
#output files of eigencon (Mineos). The files are all in the given folder. If
#unmineos=True, r and omega are converted to Mineos unit system. The
#eigenfunctions are already given in the Mineos unit system in the output files
#of eigcon
```

```
def ReadEigenMode(folder,unmineos=True):
    n=[]
    l=[]
    omega=[]
    Q=[]
    U=[]
    dUdr=[]
    V=[]
    dVdr=[]
    P=[]
    dPdr=[]
    for filename in os.listdir(folder):
        path=os.path.join(folder, filename)
        ni,li,Ti,Qi,=np.loadtxt(path,max_rows=1,usecols = (0,1,4,7),unpack=True)
        omegai=2*np.pi/Ti*1000 #omega in mHz
        if unmineos:
            omegai=un.mHz2mineos(omegai)
        dataEigenMode=np.loadtxt(path,skiprows=1)
        if dataEigenMode.shape[1]==3:
            ri,Ui,dUdri=dataEigenMode.T
            Vi=np.zeros(Ui.size)
            dVdri=np.zeros(Ui.size)
            Pi=np.zeros(Ui.size)
            dPdri=np.zeros(Ui.size)
        else:
            ri,Ui,dUdri,Vi,dVdri,Pi,dPdri=dataEigenMode.T
        Ui=np.flip(Ui)
        dUdri=np.flip(dUdri)
        Vi=np.flip(Vi)
        dVdri=np.flip(dVdri)
        Pi=np.flip(Pi)
        dPdri=np.flip(dPdri)
        n.append(ni)
        l.append(li)
        omega.append(omegai)
        Q.append(Qi)
        U.append(Ui)
        dUdr.append(dUdri)
        V.append(Vi)
        dVdr.append(dVdri)
        P.append(Pi)
        dPdr.append(dPdri)
```

```
    ri=np.flip(ri)
    if unmineos:
        ri=un.m2mineos(ri)
    return(n,l,omega,Q,ri,U,dUdr,V,dVdr,P,dPdr)
```

E.2.2 Functions related to time (Time)

```
import numpy as np
import scipy.signal as sig

#Compute the time dependence of a normal mode with frequency omega and damping
#coefficient q. t contains the times for which the time series should be
#calculated. If noq=True, damping is ignored
def TimeSeries(omega,q,t,noq=False):
    if noq or q==0:
        eigenschwing=(1-np.cos(omega*t))
    else:
        eigenschwing=(1-np.cos(omega*t)*np.exp(-omega*t/(2*q)))
    return(eigenschwing)


#Returns a numpy array t with times between t0 and t0+T sampled by deltat
def time(T,deltat,t0=0):
    N=int(T/deltat+1)
    t=np.linspace(t0,(N-1)*deltat+t0,N)
    return(t)

#Calculate the convolution of two time series x1 and x2 which are sampled by
#deltat
def convol(x1,x2,dt):
    mess=dt*sig.fftconvolve(x1,x2,mode='full')
    return(mess)
```

E.2.3 Constants and unit conversion (Units)

```
import numpy as np
###Constants
rhon=5515
piG=np.pi*6.6723e-11
rn=6.371e6
flat = 1/298.256
```

```
###Unit conversion
#For numerical stability Mineos has its own unit system. The following units
#exist:
#1 roh_n= 5515kg/m^3
#1 pi*G=pi*6.6723e-11 m^3/(kg s^2)
#1 rn= 6.3781e6 m
#Out of these basic units other units can be constructed. For example
#1m/s^2=1/(6.3781e6*5515*pi*6.6723e-11) rn*rohn*pi*G

def mpers2mineos(a):#from m/s to Mineos units
    return(a/(rn*np.sqrt(rhon*piG)))

def mineos2mpers(a):#from Mineos units to m/s
    return(a*rn*np.sqrt(rhon*piG))

def mHz2mineos(a):#from mHz to Mineos units
    return(a*1e-3*1/np.sqrt(rhon*piG))

def mineos2mHz(a):#from Mineos units to mHz
    return(a*1e3*np.sqrt(rhon*piG))

def m2mineos(a):#from m to Mineos units
    return(a/rn)

def mineos2m(a):#from Mineos units to m
    return(a*rn)

def mpersqrs2mineos(a):#from m/s^2 to Mineos units
    return(a/(rn*rhon*piG))

def mineos2mpersqrs(a):#from Mineos to m/s^2
    return(a*(rn*rhon*piG))

def Nm2mineos(a):#from Nm to Mineos units
    return(a/(rhon**2*rn**5*piG))

def mineos2Nm(a):#from Mineos units to Nm
    return(a*(rhon**2*rn**5*piG))

def s2mineos(a):#from s to Mineos units
    return(a*np.sqrt(rhon*piG))
```

```
def mineos2s(a):#from Mineos units to s
    return(a/np.sqrt(rhon*piG))

def sqrHz2mineos(a):# from 1/s^2 to Mineos units
    return(a/(rhon*piG))

def mineos2sqrHz(a):# from Mineos units to 1/s^2
    return(a*rhon*piG)
```

E.2.4 Geometry (geometry)

```
import math as m
import Units as un

#geodetic to geocentric coordinates
def geodetic2geocent(xi,phi):
    xirad=2*m.pi*xi/360
    phirad=2*m.pi*phi/360
    geocentlat=m.atan((1-un.flat)**2*m.tan(xirad))
    theta=m.pi/2-geocentlat
    return(theta,phirad)

# Compute colatitude Delta of the receiver in epicentric coordinates
def ComputeDelta(thetas,thetar,phis,phir):
    return(m.acos(m.cos(thetar)*m.cos(thetas)+
                  m.sin(thetar)*m.sin(thetas)*m.cos(phir-phis)))

#Compute Longitude Phi of the receiver in epicentric coordinates
def ComputePhi(thetas,thetar,phis,phir,Delta):
    PhiTest=m.acos(-(m.cos(thetar)-
                     m.cos(thetas)*m.cos(Delta))/(m.sin(thetas)*m.sin(Delta)))
    if abs(m.sin(phir-phis)*m.sin(thetar)/m.sin(Delta)-m.sin(PhiTest))<1e-7:
        return(PhiTest)
    else:
        PhiTest=2*m.pi-PhiTest
        if abs(m.sin(phir-phis)*m.sin(thetar)/m.sin(Delta)-m.sin(PhiTest))<1e-7:
            return(PhiTest)
        else:
            print('Error in ComputePhi')
```

```
#Compute azimuth gamma of the earthquakes epicentre observed at the receiver
def ComputeGamma(thetas,thetar,phis,phir,Delta):
    gammaTest=m.acos((m.cos(thetas)-
                      m.cos(Delta)*m.cos(thetar))/(m.sin(Delta)*m.sin(thetar)))
    if abs((m.sin(thetas)*m.sin(phir-phis)/m.sin(Delta))-m.sin(gammaTest))<1e-7:
        return(gammaTest)
    else:
        gammaTest=2*m.pi-gammaTest
        if (abs((m.sin(thetas)*m.sin(phir-phis)/m.sin(Delta))-m.sin(gammaTest))
            <1e-7):
            return(gammaTest)
        else:
            print('Error in ComputeGamma')


#Compute coordinates of source and receiver in all needed coordinate
#systems
def changeangles(latR,lonR,latS,lonS,ReturnGamma=False):
    thetar,phir=geodetic2geocent(latR,lonR)
    thetas,phis=geodetic2geocent(latS,lonS)
    Delta=ComputeDelta(thetas,thetar,phis,phir)
    Phi=ComputePhi(thetas,thetar,phis,phir,Delta)
    if ReturnGamma:
        gamma=ComputeGamma(thetas,thetar,phis,phir,Delta)
        return(Delta,Phi,gamma)
    else:
         return(Delta,Phi)

#Rotate the gravity gradient tensor to the local south oriented reference frame
def RotateGravTensor(Txx,Txy,Txz,Tyy,Tyz,Tzz,gamma):
    Txxneu=(m.cos(gamma)**2*Txx-2*m.sin(gamma)*m.cos(gamma)*Txy
            +m.sin(gamma)**2*Tyy)
    Txyneu=(m.cos(gamma)*m.sin(gamma)*Txx+m.cos(2*gamma)*Txy
            -m.cos(gamma)*m.sin(gamma)*Tyy)
    Txzneu=m.cos(gamma)*Txz-m.sin(gamma)*Tyz
    Tyyneu=(m.sin(gamma)**2*Txx+2*m.sin(gamma)*m.cos(gamma)*Txy
            +m.cos(gamma)**2*Tyy)
    Tyzneu=m.sin(gamma)*Txz+m.cos(gamma)*Tyz
    Tzzneu=Tzz
    return(Txxneu,Txyneu,Txzneu,Tyyneu,Tyzneu,Tzzneu)
```

E.2.5 Interpolation of eigenfunctions (`interpol`)

```
import numpy as np

#Fit a third order polynomial to values and derivatives of the function given at
#two points
def cubicfit(x1,x2,y1,y1diff,y2,y2diff):
    vecy=np.array([y1,y1diff,y2,y2diff])

    matrix=np.array([[x1*x1*x1,x1*x1,x1,1],
                     [3*x1*x1,2*x1,1,0],
                     [x2*x2*x2,x2*x2,x2,1],
                     [3*x2*x2,2*x2,1,0]])

    veccoeff=np.matmul(np.linalg.inv(matrix),vecy)
    return(veccoeff)

#Interpolate the eigenfunction X and its derivative dXdr at the source
#radius rs. X and dXdr are given at at all values of the radius given in r
def eigenfuncatsource(r,X,dXdr,rs):

    r0=r[np.nonzero(r<rs)][-1]
    r1=r[np.nonzero(r>=rs)][0]

    y0=X[np.nonzero(r<rs)][-1]
    y1=X[np.nonzero(r>=rs)][0]

    y0diff=dXdr[np.nonzero(r<rs)][-1]
    y1diff=dXdr[np.nonzero(r>=rs)][0]

    coeff=cubicfit(r0,r1,y0,y0diff,y1,y1diff)
    derivcoeff=[coeff[i]*(3-i) for i in range(0,3)]

    ys=np.polyval(coeff,rs)
    dydrs=np.polyval(derivcoeff,rs)

    return(ys,dydrs)
```

E.2.6 Double dot product of moment tensor and strain tensor (CoeffMomentStrain)

```
import numpy as np

#Strain Tensor at the pole for eigenmode lm, for given Ulm and Vlm and its
#derivatives at source radius rs
#Reference: Masters, G. SIO227B class notes at UCSD

def ComputeStrain(l,m,rs,U_rs,dUdr_rs,V_rs,dVdr_rs,):
    F=(2*U_rs-l*(l+ 1)*V_rs )/rs
    X=dVdr_rs+(U_rs-V_rs)/rs
    if m==0:
        d=np.sqrt((2*l+1)/(4*np.pi))

        err=d*dUdr_rs
        eDD=d*0.5*F
        ePP=eDD
        twoerD=0
        twoerP=0
        twoeDP=0

    if (m==1 or m==-1):
        d=1/2*np.sqrt((2*l+1)/(4*np.pi)*(l+1)*l)

        err=0
        eDD=0
        ePP=0
        twoerD=-d*m*X
        twoerP=-1j*d*X
        twoeDP=0

    if (m==2 or m==-2):
        d=1/4*np.sqrt((2*l+1)/(4*np.pi)*(l+2)*(l+1)*l*(l-1))

        err=0
        eDD=d*(V_rs/rs)
        ePP=-eDD
        twoerD=0
        twoerP=0
        twoeDP=d*m*1j*V_rs/rs
```

```
    return(np.array([err,eDD,ePP,twoerD,twoerP,twoeDP]))

#Compute e*:M
def MultMomentStrain(l,m,rs,U_rs,dUdr_rs,V_rs,dVdr_rs,M):
    e=ComputeStrain(l,m,rs,U_rs,dUdr_rs,V_rs,dVdr_rs)
    e=np.conjugate(e)
    multMe=0
    for i in range(6):
        multMe+=e[i]*M[i]
    return(multMe)
```

E.2.7 Displacement, gravity and gravity gradient change induced by normal modes at the Earth's surface at the receiver coordinates (EigenReceiver)

```
import scipy.special as sp
import math
import cmath
import numpy as np
#Compute Vertical Displacement at the receiver coordinates rr, thetar and phir
#related to the eigenfunctions nUl_rr and nVl_rr
def VertDispEigen(l,m,U_rr,thetar,phir):
    X=U_rr*sp.sph_harm(m,l,phir,thetar)
    return(X)

#Compute vertical gravity at the receiver coordinates rr, thetar and phir
#related to the eigenfunction nPl.  Derivative of nPl are computed by
#dnPl/dr=(l+1)/r0*nPl (r0, the radius of the earth is 1 in Mineos units)
#As the sign convention for the potential used in Mineos is opposite from
#the one in this thesis, the sign here is opposite to Equations 6.31
#in this thesis
def VertGravEigen(l,m,P_rr,thetar,phir):
    X=-(l+1)*P_rr*sp.sph_harm(m,l,phir,thetar)
    return(X)

#Same as VertGravEigen, but for dnPl/dr the value of the derivative given by
#Mineos is used
def VertGravEigen2(l,m,dPdr_rr,thetar,phir):
    X=-dPdr_rr*sp.sph_harm(m,l,phir,thetar)
    return(X)
```

```
#Compute Gradient Tensor at the receiver coordinates rr, thetar and phir related
#to Gravity Eigenfunction nPl_rr for degree and order l and m. Needs the first
#and second derivatives Plm_dtheta and Plm_d2theta of the Legendre Function
#Plm.
def GradientTensor(l,m,P_rr,thetar,phir,Plm_dtheta,Plm_d2theta):

    #Calculate spherical harmonics and its first and second derivatives
    Ylm=sp.sph_harm(m,l,phir,thetar)

    Ylm_dphi=1j*m*Ylm
    Ylm_d2phi=-m*m*Ylm
    Ylm_dtheta=Plm_dtheta*cmath.exp(1j*m*phir)
    Ylm_dphi_dtheta=1j*m*Ylm_dtheta
    Ylm_d2theta=Plm_d2theta*cmath.exp(1j*m*phir)



    #Calculate first and second derivatives of the potential
    Pot_dphi=P_rr*Ylm_dphi
    Pot_d2phi=P_rr*Ylm_d2phi
    Pot_dtheta=P_rr*Ylm_dtheta
    Pot_d2theta=P_rr*Ylm_d2theta
    Pot_dphi_dtheta=P_rr*Ylm_dphi_dtheta
    Pot_dr=-(l+1)*P_rr*Ylm
    Pot_d2r=(l+2)*(l+1)*P_rr*Ylm
    Pot_dphi_dr=-(l+1)*P_rr*Ylm_dphi
    Pot_dtheta_dr=-(l+1)*P_rr*Ylm_dtheta

    #Setup the gravity gradient tensor from the derivatives of the potential
    #As the sign convention for the potential used in Mineos is opposite
    #from the one in this thesis, the signs here are opposite to
    #Equations 6.32-6.37 in this thesis
    Txx=-Pot_d2theta-Pot_dr
    Txy=(1/(math.tan(thetar)*math.sin(thetar))*Pot_dphi
         -1/math.sin(thetar)*Pot_dphi_dtheta)
    Txz=Pot_dtheta-Pot_dtheta_dr
    Tyy=-1/math.tan(thetar)*Pot_dtheta-1/math.sin(thetar)**2*Pot_d2phi-Pot_dr
    Tyz=1/math.sin(thetar)*Pot_dphi-1/math.sin(thetar)*Pot_dphi_dr
    Tzz=-Pot_d2r

    return(Txx,Txy,Txz,Tyy,Tyz,Tzz)
```

```
#Compute unnormalised Legendre Functions Plm(cos(thetar))and its first and
#second derivative up to degree and order lmax and mmax. Second derivative by
#iteration formula, see Appendix A
def initializePlm(lmax,mmax,thetar):
    Plmcostheta,Plmcostheta_dtheta=sp.lpmn(mmax+2,lmax,math.cos(thetar))
    Plmcostheta_dtheta*=-math.sin(thetar)
    Plmcostheta_d2theta=np.zeros((mmax+1,lmax+1))
    for l in range(lmax+1):
        for m in range(min((l+1,mmax+1))):
            a1=1/4*(l+m)*(l-m+1)*(l+m-1)*(l-m+2)
            a2=-1/4*((l+m)*(l-m+1)+(l-m)*(l+m+1))
            a3=1/4
            Plm=Plmcostheta[m,l]
            Plmplus2=Plmcostheta[m+2,l]
            if m<2:
                Plmminus2=Plmcostheta[(2-m),l]
                if Plmminus2 !=0:
                    Plmminus2*=(-1)**(2-m)*(math.factorial(l-(2-m))
                                           /math.factorial(l+(2-m)))
            else:
                Plmminus2=Plmcostheta[m-2,l]
            Plmcostheta_d2theta[m,l]=a1*Plmminus2+a2*Plm+a3*Plmplus2
    return(Plmcostheta,Plmcostheta_dtheta,Plmcostheta_d2theta)

#Evaluate and normalise Plm and its first and second derivative for given l and m
#m can be negative (P_l^(-m)=(-1)^m P_l^m for normalised Plm)
def evaluatePlm(Plm,Plm_dtheta,Plm_d2theta,l,m):
    if m<0:
        faktor=(-1)**m*math.sqrt((2*l+1)/(4*math.pi)*(math.factorial(l+m)
                                                      /math.factorial(l-m)))
    else:
        faktor=math.sqrt((2*l+1)/(4*math.pi)(*math.factorial(l-m)
                                             /math.factorial(l+m)))

    return(faktor*Plm,faktor*Plm_dtheta,faktor*Plm_d2theta)
```

Acknowledgement

I would like to thank Karim Douch, for guiding me through the work of this thesis: You came up with the idea for this very interesting topic and we had a lot of interesting talks about it. You provided insides about gravity gradients and sensor noise and calculated the time series of noise, needed in Chapter 7 for me. Finally you made good suggestions for improving the draft of my thesis.

Furthermore, I wish to say thank you to Rudolf Widmer-Schnidrig, for many instructive discussions and explanations about normal modes and for reading and commenting the whole draft of my thesis, after I asked you just for one chapter. Especially your critical questions about the general concepts of PEGS helped me to understand the physics better.

I wish to show my appreciation to Rongjiang Wang for the insightful video conference and for sharing the QSSP code with me.

I also would like to thank Thomas Jahr for supporting me to do this external master thesis on a very uncommon topic and to Nico Sneeuw and the hole GIS team for welcoming me at the institute.

Finally I would like to express my special thanks to the motivated, persevering proof-readers Lena Feld, Christoph Bützler and Philipp Beck. By contributing all three very different comments, corrections and questions, you helped me a lot to improve my thesis.

Bibliography

Aki, K., and P. G. Richards. 1980. *Quantitative Seismology Theory and Methods.* San Francisco: W.H. Freeman / Company.

Broersen, P. M. T., and S. de Waele. 2003. "Generating data with prescribed power spectral density." *IEEE Transactions of instrumentation and measurement* 52 (4): 1061–1067.

Douch, K., B. Christophe, B. Foulon, I. Panet, G. Pajot-Métivier, and M. Diament. 2014. "Ultra-sensitive electrostatic planar acceleration gradiometer for airborne geophysical surveys." *Meas. Sci. Technol.* 25 (105902).

Dziewonski, A., and D. Anderson. 1981. "Preliminary reference earth model." *Physics of the Earth and Planetary Interiors* 25:297–356.

Eötvös, R. 1896. "Untersuchungen über Gravitation und Erdmagnetismus." *Annalen der Physik und Chemie, Neue Folge* 59:354–400.

Frisch, W., and M. Meschede. 2005. *Plattentektonik - Kontinentverschiebung und Gebirgsbildung.* Darmstadt: Wissenschaftliche Buchgesellschaft.

Gilbert, F. 1970. "Excitation of the normal modes of the earth by earthquake source." *Geophys. J. R. astr. Soc.* 22:223–226.

Griggs, C. E., M. V. Moody, R. S. Norton, H. J. Paik, and K. Venkateswara. 2017. "Sensitive Superconducting Gravity Gradiometer Constructed with Levitated Test Masses." *Phys. Rev. Appl.* 8 (064024).

Harms, J. 2016. "Transient gravity perturbations from a double-couple in a homogeneous half-space." *Geophys. J. Int* 205:1153–1164.

Harms, J., J.-P. Ampuero, M. Barsuglia, E. Chassande-Mottin, J.-P. Montagner, S. N. Somala, and B. F. Whiting. 2015. "Transient gravity perturbations induced by earthquake rupture." *Geophys. J. Int* 201:1416–1425.

Heaton, T. H. 2017. "Correspondence: Response of a gravimeter to an instantaneous step in gravity." *Nat. Commun.* 8 (1348).

Ilk, K. H. 1983. *Ein Beitrag zur Dynamik ausgedehnter Körper - Gravitationswechselwirkung.* München: Verlag der Bayerischen Akademie der Wissenschaften.

Japanese ministry of economy, trade and industry. 2011. *INES (the International Nuclear and Radiological Event Scale) Rating on the Events in Fukushima Dai-ichi Nuclear Power Station by the Tohoku District - off the Pacific Ocean Earthquake.* Archived from the website of the Japanese ministry of economy, trade and industry: `https://www.webcitation.org/5xsyUr2Wx?url=http://www.nisa.meti.go.jp/english/files/en20110412-4.pdf`. Accessed: 2020-11-18.

Juhel, K. 2018. *gravity-eew.* Python Code: `https://github.com/kjuhel/gravity-eew`. Last changes: 2018-11-02.

Juhel, K., J. P. Ampuero, M. Barsuglia, P. Bernard, E. Chassande-Mottin, D. Fiorucci, J. Harms, J.-P. Montagner, M. Vallée, and B. F. Whiting. 2018a. "Earthquake Early Warning Using Future Generation Gravity Strainmeters." *J. Geophys. Res., Solid Earth* 123:10889–10902.

Juhel, K., J.-P. Montagner, M. Vallée, J. P. Ampuero, M. Barsuglia, Bernard, E. Clévédé, J. Harms, and B. F. Whiting. 2018b. "Normal mode simulation of prompt elastogravity signals induced by an earthquake rupture." *Geophys. J. Int* 216:935–947.

Juhel, K. 2017. "Signaux gravitationnels transitoires générés par rupture sismique." Thèse de doctorat, Institut de Physique du Globe de Paris.

Kame, N., and M. Kimura. 2019. "The fundamental nature of a transient elastic response to prompt gravity perturbations." *Geophys. J. Int.* 218:1136–1142.

Mansinha, L., and T. Hayes. 2001. "A Search for Gravitational Disturbance From Earthquakes." *Journal of the Geodetic Society of Japan* 47 (1): 359–363.

Masters, G. 2014. *Mineos Version 1.0.2.* `https://geodynamics.org/cig/software/mineos/`.

Masters, G. lecture notes. *SIO227B Class notes at UCSD.* Dristributed together with the source code of mineos: `https://geodynamics.org/cig/software/mineos/`. Accessed: 2020-09-11.

Masters, G., M. Barmine, and S. Kientz. 2014. *Mineos User Manual Version 1.0.2.* `https://geodynamics.org/cig/software/mineos/mineos-manual.pdf`.

Montagner, J.-P., K. Juhel, M. Barsuglia, J. P. Ampuero, E. Chassande-Mottin, J. Harms, B. Whiting, P. Bernard, E. Clévédé, and P. Lognonné. 2016. "Prompt gravity signal induced by the 2011 Tohoku-Oki earthquake." *Nat. Commun.* 7 (13349).

Moody, M. V., H. J. Paik, and R. Canavan. 2002. "Three-axis superconducting gravity gradiometer for sensitive gravity experiments." *Rev. Sci Instrum.* 73 (11).

Mori, N., T. Takahashi, T. Yasuda, and H. Yanagisawa. 2011. "Survey of 2011 Tohoku earthquake tsunami inundation and runup." *Geophys. Res. Lett.* 38 (L00G14).

National Police Agency of Japan - Emergency Disaster Countermeasures Headquarters. 2020. *Police Countermeasures and Damage Situation associated with 2011 Tohoku district - off the Pacific Ocean Earthquake.* `https://www.npa.go.jp/news/other/earthquake2011/pdf/higaijokyo_e.pdf`. Accessed: 2020-11-03.

Nettles, M., G. Ekström, and H. C. Koss. 2011. "Centroid-moment-tensor analysis of the 2011 off the Pacific coast of Tohoku Earthquake and its larger foreshocks and aftershocks." *Earth Planets Space* 63:519–523.

Petrovskaya, M. S., and A. N. Vershkov. 2006. "Non-singular expressions for the gravity gradients in the local north-oriented and orbital reference frames." *J. Geod.* 80:117–127.

Shimoda, T., K. Juhel, J. Ampuero, J. Montagner, and M. Barsuglia. 2020. *Early earthquake detection capabilities of different types of future-generation gravity gradiometers.* `https://resolver.caltech.edu/CaltechAUTHORS:20200507-124020129`.

Takeuchi, H., and M. Saito. 1992. "Seismic surface waves." In *Methods in computational physics,* edited by B. A. Bolt, vol. 11: Seismology: Surface Waves and Earth Oscillations, 217–295. New York London: Academic Press.

U.S. Geological Servey. 2011. *Magnitude 9.0 - NEAR THE EAST COAST OF HONSHU, JAPAN.* Archived from the USGS website: `https://www.webcitation.org/query?url=http://earthquake.usgs.gov/earthquakes/recenteqsww/Quakes/usc0001xgp.php`. Accessed: 2020-11-03.

Vallée, M., and K. Juhel. 2019. "Multiple Observations of the Prompt Elastogravity Signals Heralding Direct Seismic Waves." *J. Geophys. Res., Solid Earth* 124:2970–2989.

Vallée, M., J. P. Ampuero, K. Juhel, P. Bernard, J.-P. Montagner, and M. Barsuglia. 2017. "Observations and modeling of the elastogravity signals preceding direct seismic waves." *Science* 358 (6367): 1164–1168.

Veryaskin, A. V. 2018. *Gravity, Magnetic and Electromagnetic Gradiometry.* San Rafael California: Morgan / Claypool Publishers.

Wang, R., S. Heimann, Y. Zhang, H. Wang, and T. Dahm. 2017. "Complete synthetic seismograms based on a spherical self-gravitating Earth model with an atmosphere–ocean–mantle–core structure." *Geophys. J. Int.* 210:1739–1764.

Woodhouse, J. H., and A. Deuss. 2015. “Theory and Observations - Earth’s Free Oscillations.” In *Treatise on Geophysics,* edited by G. Schubert, 1:79–115. Oxford: Elsevier.

Zhang, S., R. Wang, T. Dahm, S. Zhou, and S. Heimann. 2020. “Prompt elasto-gravity signals (PEGS) and their potential use in modern seismology.” *Earth Planet. Sci. Lett.* 536 (116150).